

OSU

8008

Ohio State University

AD-A222 908  
100-1

INLET MODELING STUDIES

by

P.H. Pathak, C.W. Chuang, M.C. Liang

PTIC  
LECTE  
JN 20 1990  
D D

The Ohio State University

ElectroScience Laboratory

Department of Electrical Engineering  
Columbus, Ohio 43212

Technical Report 717674-1  
Contract No. N60530-85-C-0249  
October 1986

DISTRIBUTION STATEMENT A

Approved for public release  
Distribution Unlimited

**BEST  
AVAILABLE COPY**

Department of the Navy  
Naval Weapons Center  
China Lake, CA 93555

90 06 19 001

## NOTICES

When Government drawings, specifications, or other data are used for any purpose other than in connection with a definitely related Government procurement operation, the United States Government thereby incurs no responsibility nor any obligation whatsoever, and the fact that the Government may have formulated, furnished, or in any way supplied the said drawings, specifications, or other data, is not to be regarded by implication or otherwise as in any manner licensing the holder or any other person or corporation, or conveying any rights or permission to manufacture, use, or sell any patented invention that may in any way be related thereto.

<b>REPORT DOCUMENTATION PAGE</b>		1. REPORT NO.	2.	3. Recipient's Accession No.										
4. Title and Subtitle		Inlet Modeling Studies		5. Report Date October 1986										
7. Author(s)		P.H. Pathak, C.W. Chuang, M.C. Liang		6.										
9. Performing Organization Name and Address		The Ohio State University ElectroScience Laboratory 1320 Kinnear Road Columbus, Ohio 43212		8. Performing Organization Rept. No. 717674-1										
12. Sponsoring Organization Name and Address		Department of the Navy Naval Weapons Center China Lake, California 93555		10. Project/Task/Work Unit No.										
15. Supplementary Notes				11. Contract(C) or Grant(G) No (C) N60530-85-C-0249 (G)										
16. Abstract (Limit: 200 words)		<p>An analysis is developed for predicting the near zone fields scattered by perfectly-conducting, open-ended, semi-infinite circular and rectangular waveguides (or ducts) which are excited by an external electromagnetic (EM) plane wave. These waveguides are terminated inside by various structures such as a planar impedance surface, or a disk/blade structure with and without a hemispherical or a conical hub. The analysis is based on a combination of asymptotic high frequency techniques such as ray methods, the equivalent current approach, and the physical theory of diffraction, with the usual modal techniques, all of which are used in conjunction with the multiple scattering method (MSM). Basically, the scattering matrices in the MSM, which account for the multiple wave interactions between the open end and the interior termination are found efficiently via the asymptotic high frequency techniques. The latter techniques provide relatively simple expressions not only for the fields scattered from the rim edge at the open-end of the ducts, but also for the amplitudes of the modes coupled into the duct by the incident plane wave as well as the reflection coefficients of the modes at the open end. Some numerical results are provided for the near and far field bistatic scattering. Whenever possible, a comparison via other approaches is provided to illustrate the accuracy of the numerical results for the elements of the scattering matrices of the MSM, since the</p>												
<p>17. Document Analysis</p> <p>a. Descriptors</p> <table> <tr> <td>Open ended waveguides</td> <td>PTD</td> </tr> <tr> <td>EM Scattering</td> <td>Waveguide Modal reflection coefficients</td> </tr> <tr> <td>GTD</td> <td>Multiple scattering method (MSM)</td> </tr> <tr> <td>UTD</td> <td>Generalized scattering matrices</td> </tr> <tr> <td>Equivalent currents</td> <td></td> </tr> </table> <p>b. Identifiers/Open-Ended Terms</p>					Open ended waveguides	PTD	EM Scattering	Waveguide Modal reflection coefficients	GTD	Multiple scattering method (MSM)	UTD	Generalized scattering matrices	Equivalent currents	
Open ended waveguides	PTD													
EM Scattering	Waveguide Modal reflection coefficients													
GTD	Multiple scattering method (MSM)													
UTD	Generalized scattering matrices													
Equivalent currents														
18. Availability Statement		19. Security Class (This Report)	21. No. of Pages											
A. Approved for public release; distribution is unlimited.		Unclassified												
		20. Security Class (This Page)	22. Price											
		Unclassified												

Unclassified

SECURITY CLASSIFICATION OF THIS PAGE(When Data Entered)

accuracy of these elements ultimately decide the accuracy of the complete solution of the scattering by the inlets as developed in this report. For the circular waveguide case, the accuracies of extensive calculated backscattering returns have been substantiated by measurements. The method is also applied to evaluating plane wave scattering by rectangular and semi-circular waveguides mounted on a ground plane.



Accession For	
NTIS	CRA&I
DTIC	TAB
Unannounced	
Justification	
By _____	
Distribution / _____	
Availability Codes	
Dist	Avail and/or Special
A-1	

ii Unclassified  
SECURITY CLASSIFICATION OF THIS PAGE(When Data Entered)

## TABLE OF CONTENTS

LIST OF TABLES	v
LIST OF FIGURES	vi
	<u>Page</u>
I. INTRODUCTION	1
II. SELF-CONSISTENT MSM FORMULATION	7
III. ANALYSIS FOR THE ELEMENTS OF THE SCATTERING MATRICES	21
A. Development of $[S_{11}]$	21
B. Development of $[S_{21}]$	30
C. Near Zone Coupling Matrix $\tilde{[S_{21}]}$	50
D. Development of $[S_{12}]$ Using Reciprocity	51
E. Development of $[S_{22}]$	72
F. Development of $[S_r]$	84
IV. NUMERICAL RESULTS AND COMPARISONS WITH MEASUREMENTS FOR THE SCATTERING BY THE COMPLETE INLET CONFIGURATIONS OF FIGURE 1	86
V. CONCLUSION	134
APPENDICES	
I WAVEGUIDE EXCITATION PROBLEM	136
II TABLES FOR THE CIRCULAR AND RECTANGULAR WAVEGUIDE MODE FUNCTIONS	142
III EXPLICIT RADIATION COEFFICIENT FOR CIRCULAR AND RECTANGULAR INLETS	145
A. For Circular Inlets:	145
B. For Rectangular Inlets:	147
IV EXPLICIT MODAL REFLECTION COEFFICIENTS AT THE OPEN END FOR THE CIRCULAR AND RECTANGULAR INLETS	152
A. For Circular Inlets:	153
B. For Rectangular Inlets:	155

	<u>Page</u>
V DEFINITIONS OF THE GENERALIZED SCATTERING MATRICES FOR THE FAR-ZONE SCATTERING SITUATION	157
VI MODAL REFLECTION COEFFICIENTS FOR BLADE/DISK AND HUB STRUCTURE TERMINATIONS IN CIRCULAR INLETS	159
REFERENCES	163

## LIST OF TABLES

<u>Table</u>		<u>Page</u>
1	PROPERTIES OF MODES IN CIRCULAR WAVEGUIDE	143
2	PROPERTIES OF MODES IN RECTANGULAR WAVEGUIDE	144

## LIST OF FIGURES

<u>Figure</u>	<u>Page</u>
1(a). EM scattering by a circular inlet with a planar impedance termination inside.	2
1(b). EM scattering by a rectangular inlet with a planar impedance termination inside.	2
1(c). EM scattering by a circular inlet with a conical hub.	3
1(d). EM scattering by a circular inlet with a hemispherical hub.	3
1(e). Different planar terminations on which the hub is attached.	4
1(f). EM scattering by a rectangular waveguide mounted on a ground plane.	4
1(g). EM scattering by a semi-circular waveguide mounted on a ground plane.	4
2(a). EM scattering by a circular inlet with a termination inside.	5
2(b). EM scattering by a rectangular inlet with a termination inside.	5
3. Multiple scattering between junctions $\textcircled{I}$ and $\textcircled{II}$ .	9
4. Scattering by only the rim at the open end of the inlet. Scattering occurs both in the exterior as well as the interior regions of the inlet.	9
5. Radiation and reflection at the open end due to a waveguide mode incident at the opening.	10
6. Reflection of waveguide modes from the impedance surface termination at $z=-L$ .	10
7. Multiple interactions between junctions $\textcircled{I}$ and $\textcircled{II}$ for calculating the total backscattered field.	19
8. Scattering from the open end and its equivalent problem.	25
9. Diffraction by a wedge. The angles $\beta_0$ , $\beta$ , $\psi'$ and $\psi$ which occur in the edge diffraction coefficient.	27
10. A comparison of the far zone and near zone edge diffraction from the open end of circular inlet for a $30^\circ$ cone scan.	31
11. A comparison of the far zone and near zone edge diffraction from the open end of circular inlet for $\phi = 0$ cut.	32
12. A comparison for $\theta = 5^\circ$ and $\theta = 30^\circ$ cone scan patterns with $\theta^1 = 5^\circ$ plane wave incidence.	33

<u>Figure</u>	<u>Page</u>
13. A comparison of the far zone and near zone edge diffraction from the open end of a rectangular inlet and also the near zone $30^\circ$ cone scan patterns for different incident angles.	34
14. A comparison of the far zone and near zone edge diffraction from the open end of rectangular inlet for $\phi = 0^\circ$ cut.	37
15. The $30^\circ$ cone scan patterns for rectangular inlet with comparable area or comparable dimension as that of circular inlet in Figure 10.	38
16. On-axis backscattered RCS (normalized to $\pi a^2$ ) from a semi-infinite, hollow, perfectly-conducting circular cylinder with various terms included in UTD calculations.	40
17. Geometry associated with $[S_{21}]$ calculation.	42
18(a). Geometry for an application of the reciprocity theorem which relates $[S_{12}]$ and $[S_{21}]$ .	53
18(b). Radiation or $[S_{12}]$ problem.	54
18(c). Coupling or $[S_{21}]$ problem.	54
19. $E_\phi$ radiation pattern due to a $TE_{01}$ mode in an open-ended circular waveguide.	59
20. $E_\theta$ and $E_\phi$ radiation patterns due to a $TE_{11}$ mode in an open-ended circular waveguide.	60
21. $E_\theta$ radiation pattern due to a $TM_{01}$ mode in an open-ended circular waveguide.	61
22. $E_\theta$ and $E_\phi$ radiation patterns due to a $TM_{11}$ mode in an open-ended circular waveguide.	62
23. $E_\theta$ and $E_\phi$ radiation patterns due to a $TM_{11}$ mode in an open-ended circular waveguide.	63
24. The near zone radiation patterns of $TE_{11}$ modes.	64
25. The near zone radiation patterns of $TM_{11}$ modes.	65
26. The near zone radiation patterns of $TE_{41}$ modes.	66
27. The near zone radiation patterns of $TE_{31}$ modes.	67
28. The near zone radiation patterns of $TE_{12}$ modes.	68
29. The near zone radiation pattern of $TM_{02}$ mode.	69

<u>Figure</u>	<u>Page</u>
30. Near zone radiation pattern of an open-ended rectangular waveguide. $ka=12.58$ , $a=2b$ , $TE_{10}$ mode, $\phi^r=0^\circ$ , $kR=62.90$ .	69
31. Near zone radiation pattern of an open-ended rectangular waveguide. $ka=12.58$ , $a=2b$ , $TE_{10}$ mode, $\phi^r=90^\circ$ , $kR=62.90$ .	70
32. Far zone radiation pattern of an open-ended rectangular waveguide. $ka=12.58$ , $a=2b$ , $TE_{10}$ mode, $\phi^r=0^\circ$ .	70
33. Far zone radiation pattern of an open-ended rectangular waveguide. $ka=12.58$ , $a=2b$ , $TE_{10}$ mode, $\phi^r=90^\circ$ .	71
34. Geometry for the reflection coefficient matrix $[S_{22}]$ calculation.	73
35. Modal reflection coefficients due to an incident $TE_{01}$ mode in an open-ended circular waveguide.	77
36. Modal reflection coefficients due to an incident $TE_{11}$ mode in an open-ended circular waveguide.	78
37. Modal reflection coefficients due to an incident $TM_{01}$ mode in an open-ended circular waveguide.	79
38. Modal reflection coefficients due to an incident $TM_{11}$ mode in an open-ended circular waveguide.	80
39. Modal reflection coefficients due to an incident $TE_{10}$ mode in an open-ended rectangular waveguide ( $a=2b$ ).	81
40. Modal reflection coefficients due to an incident $TM_{11}$ mode in an open-ended rectangular waveguide ( $a=2b$ ).	82
41. Comparisons of the calculated and measured reflection coefficients in an x-band and ku-band open-ended rectangular waveguide.	83
42. Contributions to the $\phi=180^\circ$ patterns for circular inlet.	89
43. Contributions to the $\phi=0^\circ$ patterns for circular inlet.	90
44. Contributions to the $30^\circ$ cone scan patterns for circular inlet.	91
45. Contributions to the $30^\circ$ cone scan patterns for circular inlet with almost matched termination. ( $\epsilon_r = 1-0.1j$ )	92
46. Contributions to the $30^\circ$ cone scan patterns for rectangular inlet with size $(A,B) = (2,1)$ .	93

<u>Figure</u>		<u>Page</u>
47.	Contributions to the $30^\circ$ cone scan patterns for a rectangular inlet with size $(A,B) = (1,2)$ .	94
48.	Contributions to the $\phi=0^\circ$ patterns for a rectangular inlet with size $(A,B) = (2,1)$ .	95
49.	On-axis RCS.	96
50.	Comparisons of calculated and measured vertical polarization backscattering patterns at (a) 9 GHz, (b) 10 GHz, and (c) 11 GHz.	100
51.	Comparisons of calculated and measured horizontal polarization backscattering patterns at (a) 9 GHz, (b) 10 GHz, and (c) 11 GHz.	103
52.	Comparisons of calculated and measured horizontal polarization backscattering patterns at (a) 10 GHz, (b) 10.2 GHz.	106
53.	Comparison of calculated and measured backscattering patterns at 10 GHz (a) vertical polarization, (b) horizontal polarization.	108
54.	Comparison of calculated and measured backscattering patterns at 10 GHz, (a) vertical polarization, (b) horizontal polarization.	110
55.	Comparison of calculated and measured backscattering patterns at 10 GHz. (a) vertical polarization, (b) horizontal polarization.	112
56.	Comparisons of calculated and measured backscattering patterns at 10 GHz. (a) vertical polarization, (b) horizontal polarization.	114
57.	Comparisons of calculated and measured backscattering patterns at 10 GHz. (a) vertical polarization, (b) horizontal polarization.	116
58.	Horizontal polarization backscattering frequency scans with $\theta^i=0^\circ$ . (a) calculated, (b) measured.	118
59.	Horizontal polarization backscattering frequency scans with $\theta^i=30^\circ$ . (a) calculated, (b) measured.	119
60.	Horizontal polarization backscattering frequency scans with $\theta^i=15^\circ$ . (a) calculated, (b) measured.	120

<u>Figure</u>	<u>Page</u>
61. Vertical polarization backscattering frequency scans with $\theta_i=15^\circ$ . (a) calculated, (b) measured.	121
62. Incident and reflected model rays associated with a conical hub termination.	124
63. Comparison of the backscattering patterns for a circular waveguide with conical hub terminations at different terminal positions.	125
64. Comparison of the backscattering patterns for a circular waveguide with conical hub termination at different terminal positions.	127
65. Comparison of backscattering returns from an open-ended circular waveguide (solid curve) and an open-ended semi-circular waveguide mounted on a ground plane (broken curve).	130
66. Comparison of near zone bistatic scattering from an open-ended rectangular waveguide (solid curve) and another one of half the size mounted on a ground plane (broken curve) for observation at $(r=4\lambda, \phi=90^\circ)$ .	132
A.1. Waveguide geometry.	137
A.2. Waveguide geometry with fields radiated to the left ( $z>z_+$ ) of S being of interest.	141

## I. INTRODUCTION

In the present report, an efficient analysis is developed for predicting the near zone fields scattered by perfectly-conducting, open-ended, semi-infinite circular and rectangular waveguides and also semi-infinite semi-circular and rectangular waveguides mounted on an infinite ground plane, which are excited by an external electromagnetic (EM) plane wave. These waveguides which model simple inlet configurations are terminated inside by various structures such as a planar impedance surface, a disk, a disk-blade geometry, and also by hemispherical and conical hubs on disks and disk-blade geometries as shown in Figures 1(a) through 1(g).

The present analysis employs a combination of high frequency techniques such as the geometrical theory of diffraction (GTD) [1,2,3] and its modifications based on the equivalent current method (ECM) [4,5,6], as well as the physical theory of diffraction (PTD) [6,7], all of which are used in conjunction with the self-consistent multiple scattering method (MSM) [8], as indicated in a previous analysis [9,10].

As is well known, the GTD employs rays to describe the phenomenon of wave radiation, propagation, scattering and diffraction at high frequencies. Furthermore, the GTD is, in general, found to remain accurate even for moderately high frequencies. In the present analysis, the GTD together with its modification at caustics and a confluence of caustics and shadow boundaries, which are based on the ECM as well as the PTD, is employed to calculate the elements of the

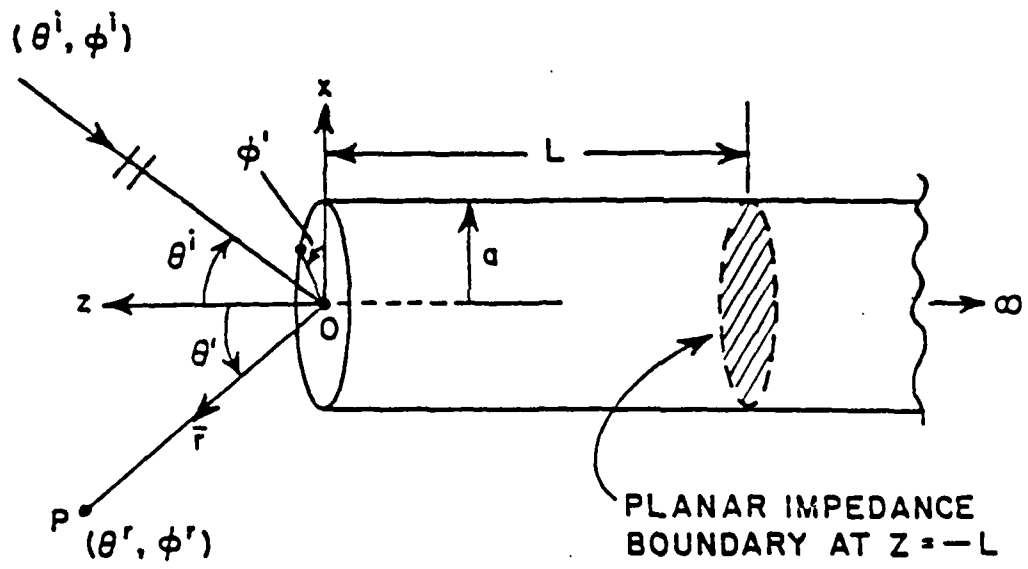


Figure 1(a). EM scattering by a circular inlet with a planar impedance termination inside.

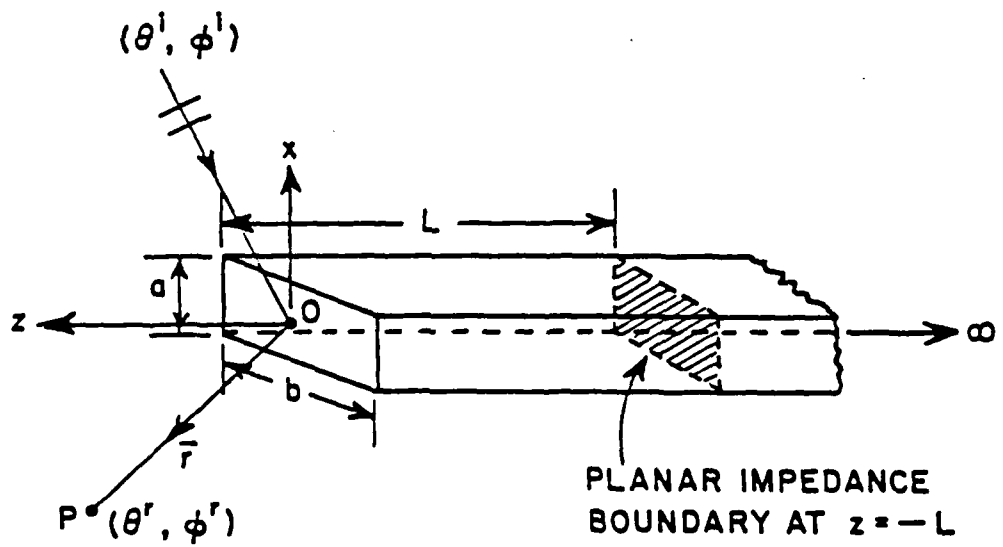


Figure 1(b). EM scattering by a rectangular inlet with a planar impedance termination inside.

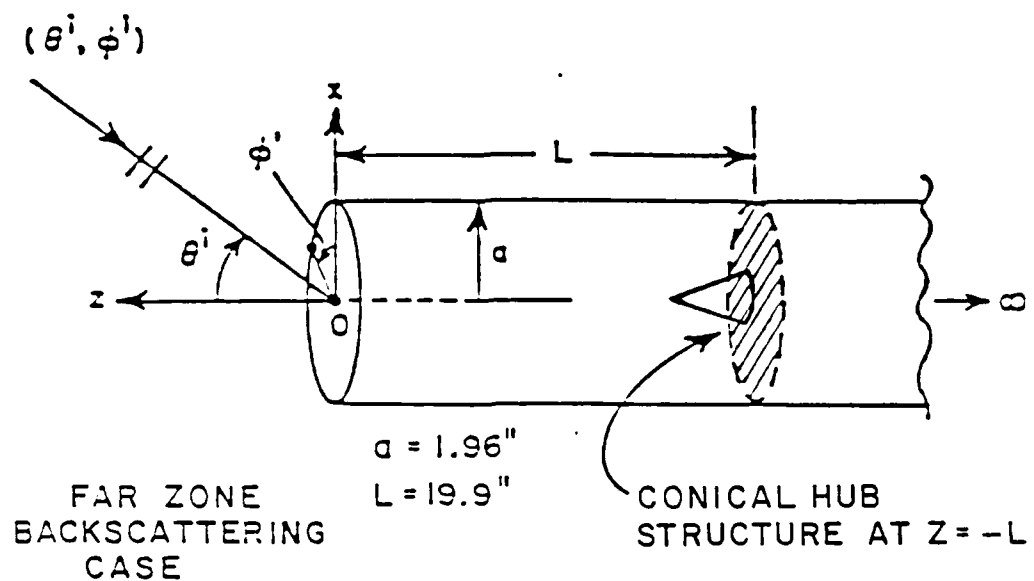


Figure 1(c). EM scattering by a circular inlet with a conical hub.

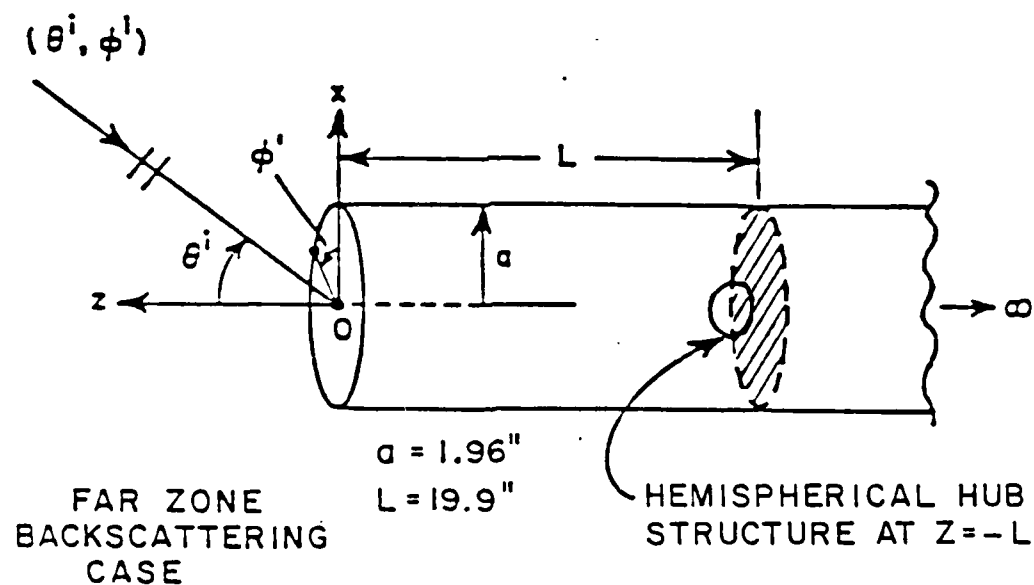
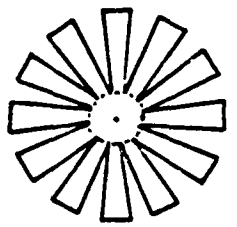
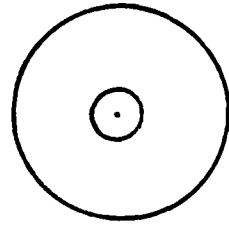


Figure 1(d). EM scattering by a circular inlet with a hemispherical hub.

FRONT VIEW:



HUB WITH  
BLADE STRUCTURE



HUB WITH  
SHORT END

Figure 1(e). Different planar terminations on which the hub is attached.

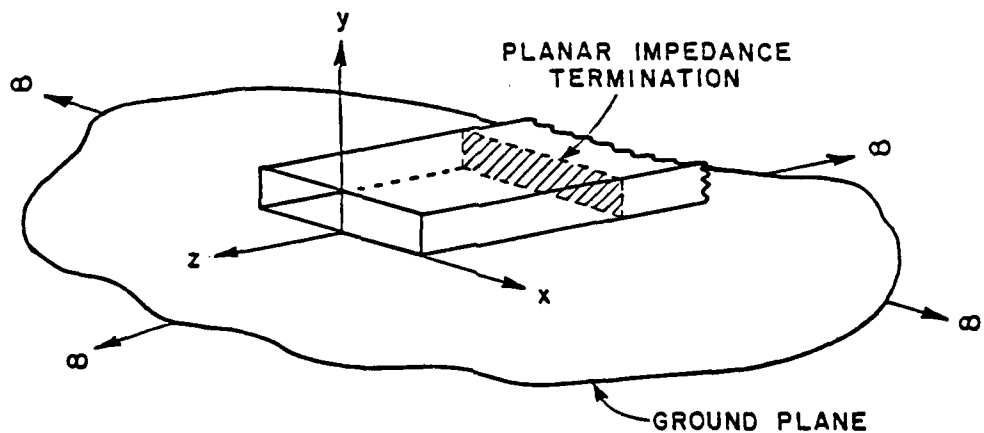


Figure 1(f). EM scattering by a rectangular waveguide mounted on a ground plane.

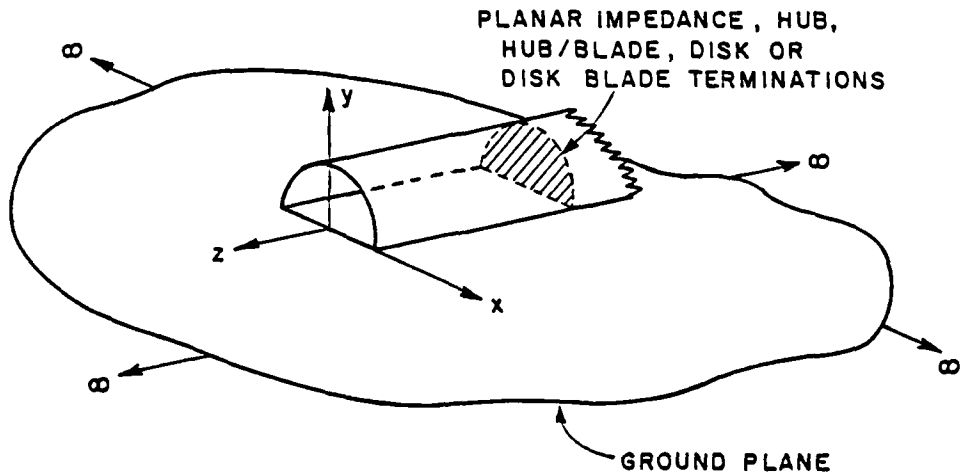


Figure 1(g). EM scattering by a semi-circular waveguide mounted on a ground plane.

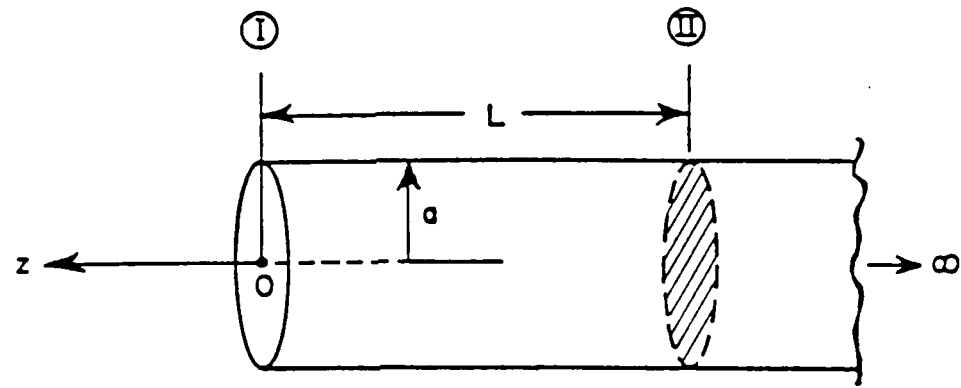


Figure 2(a). EM scattering by a circular inlet with a termination inside.

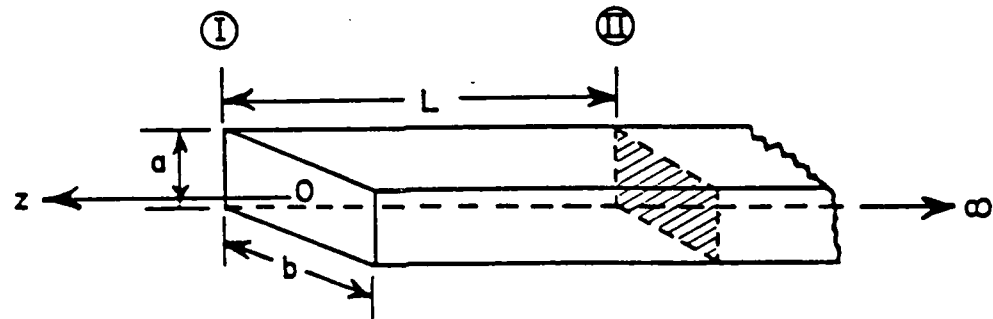


Figure 2(b). EM scattering by a rectangular inlet with a termination inside.

junction scattering matrices which are required in the MSM. These scattering matrices characterize the scattering properties of the junctions  $\textcircled{I}$  and  $\textcircled{II}$  at  $z=0$  and  $z=-L$ , respectively, which are indicated in Figures 2(a) and 2(b). The multiple wave interactions between junctions  $\textcircled{I}$  and  $\textcircled{II}$  is accounted for in a self consistent fashion in the MSM through the use of the junction scattering matrices. It is noted that the self-consistent MSM procedure used here is essentially the same as the generalized scattering matrix technique (GSMT) [11].

The format of this report is as follows. First, the self-consistent MSM formulation is discussed in Section II where the junction scattering matrices are defined. Next, the GTD/ECM/PTD based analysis to determine the elements of these junction scattering matrices in a relatively efficient manner is developed in Section III. Some numerical results illustrating the behavior of the junction scattering matrices are also presented in Section III. Finally, these relatively simple expressions for the elements of the junction scattering matrices are combined via the MSM procedure to obtain numerical results for the near field scattered by the circular, semi-circular and rectangular inlet configurations of Figure 1; several such numerical results and comparisons with measured ones are presented in Section IV together with a discussion of these results. An  $e^{+jwt}$  time convention for the electromagnetic fields is assumed and suppressed throughout this report.

## II. SELF-CONSISTENT MSM FORMULATION

As mentioned in Section I, the method of analysis which will be employed here to predict the near field bistatic EM scattering by the configurations in Figure 1 is based primarily on the GTD and the ECM, as well as the PTD, together with the self-consistent MSM. In the MSM based analysis, the basic scattering mechanisms are isolated and identified as being associated with the scattering by junctions  $\textcircled{I}$  and  $\textcircled{II}$  as in Figures 2(a) and 2(b). These junctions can likewise be identified in open-ended semi-circular and rectangular waveguides on a ground plane. The multiple scattering between the junctions is calculated via a self-consistent procedure. Such a procedure requires a knowledge of the generalized scattering matrices  $[S_{11}]$ ,  $[S_{12}]$ ,  $[S_{21}]$ ,  $[S_{22}]$ , and  $[S_T]$  for the junctions  $\textcircled{I}$  and  $\textcircled{II}$ . These generalized scattering matrices [9] are directly associated with the canonical scattering events shown in Figures 3, 4, 5 and 6 for an open-ended semi-infinite waveguide with an impedance termination at  $z=-L$ . The waveguide cross-section is shown to be arbitrary in Figures 3, 4, 5 and 6; however, as stated previously, only circular and rectangular cross-sectional waveguides are of interest in the present study. Besides an impedance termination, other terminations studied include a disk, a disk-blade, and hemispherical and conical hubs on disk and disk-blade structures. The concept of the scattering matrix in microwave circuit analysis is based on the propagating modes within the circuit and it characterizes waveguide discontinuities or circuit properties of a microwave network. Thus, the circuit scattering matrix for microwave networks is restricted to interior (guided wave) regions.

On the other hand, the polarization scattering matrix is defined for exterior regions [12]. The generalized scattering matrix extends the concept of the microwave circuit scattering matrix to include evanescent modes as well as to include the polarization scattering matrix for exterior scattering. Thus, the generalized scattering matrix approach is useful for solving scattering problems which involve a coupling between interior and exterior regions as in the problems of Figure 1. The elements of the generalized scattering matrices associated with the junctions (I) and (II) as in Figures 3, 4, 5, and 6 are defined next.

Let  $\bar{E}^i$  denote the electric field intensity of the incident electromagnetic plane wave. One may express  $\bar{E}^i$  as:

$$\bar{E}^i = \hat{\theta}^i E_\theta^i + \hat{\phi}^i E_\phi^i \quad (1)$$

with

$$E_\theta^i = A_\theta e^{-jk^i \cdot \bar{r}} ; \quad (2a)$$

$$E_\phi^i = A_\phi e^{-jk^i \cdot \bar{r}} \quad (2b)$$

where

$$k^i = -k(\sin\theta^i \cos\phi^i \hat{x} + \sin\theta^i \sin\phi^i \hat{y} + \cos\theta^i \hat{z}) \quad (3)$$

and

$$\bar{r} = \hat{x}x + \hat{y}y + \hat{z}z . \quad (4)$$

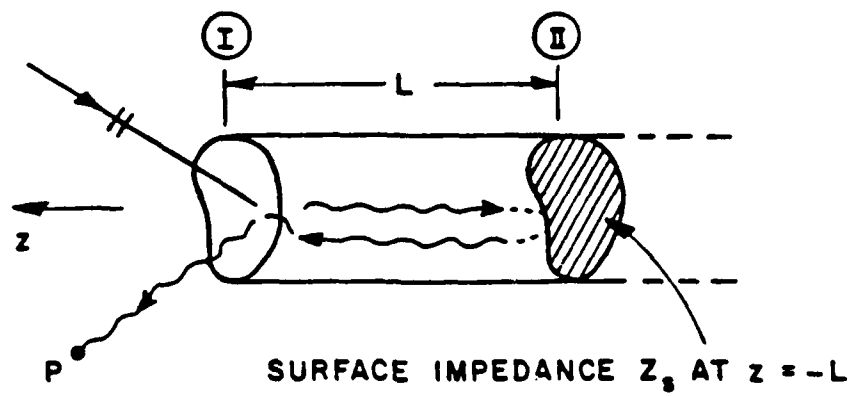


Figure 3. Multiple scattering between junctions (I) and (II).

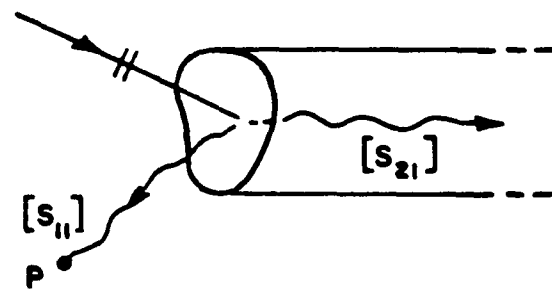


Figure 4. Scattering by only the rim at the open end of the inlet. Scattering occurs both in the exterior as well as the interior regions of the inlet.

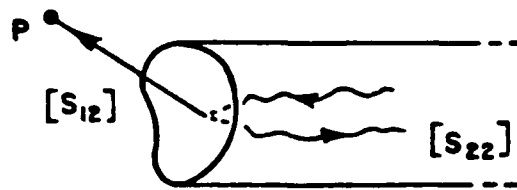


Figure 5. Radiation and reflection at the open end due to a waveguide mode incident at the opening.

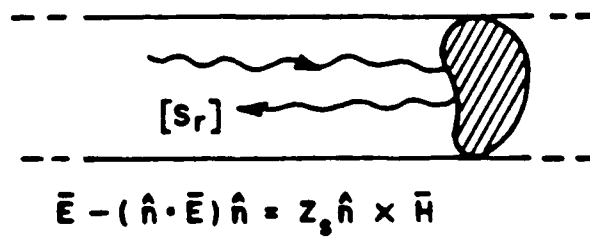


Figure 6. Reflection of waveguide modes from the impedance surface termination at  $z=-L$ .

It is noted that  $k$  refers to the free space wave number and  $\vec{r}$  refers to the position vector of an observation point at  $P$ .

One may now describe the scattering matrix  $[S_{11}]$  (see Figures 3 and 4). The scattering matrix  $[S_{11}]$  relates the electric field  $\vec{E}^{so}$  scattered from only the open end at  $z=0$  to the field  $\vec{E}^i$  which is incident on the open end as follows:

$$\begin{bmatrix} E_x^{so} \\ E_y^{so} \\ E_z^{so} \end{bmatrix} = \begin{bmatrix} S_{x\theta}^{so} & S_{x\phi}^{so} \\ S_{y\theta}^{so} & S_{y\phi}^{so} \\ S_{z\theta}^{so} & S_{z\phi}^{so} \end{bmatrix} \begin{bmatrix} A_\theta \\ A_\phi \end{bmatrix}, \quad (5)$$

where

$$\vec{E}^{so}(P) = E_x^{so}\hat{x} + E_y^{so}\hat{y} + E_z^{so}\hat{z} \quad (6)$$

and

$$[S_{11}] = \begin{bmatrix} S_{x\theta}^{so} & S_{x\phi}^{so} \\ S_{y\theta}^{so} & S_{y\phi}^{so} \\ S_{z\theta}^{so} & S_{z\phi}^{so} \end{bmatrix}. \quad (7)$$

The scattering matrix  $[S_{12}]$  converts the waveguide modal fields incident at the open end ( $z=0$ ) from the interior region ( $z<0$ ) to the fields radiated by these modes from the open end as in Figures 3 and 5. The modal electric field  $\vec{E}_g^\pm$  within the waveguide region ( $z<0$ ) may be represented in the usual manner [13]:

$$\bar{E}_g^{\pm} = \sum_{mn} [A_{nm}^{\pm} \bar{e}'_{nm} e^{\mp j\beta_{nm} z} + B_{nm}^{\pm} (\bar{e}_{nm} \pm \hat{z} e_{znm}) e^{\mp j\beta_{nm} z}] . \quad (8)$$

Here,  $\bar{e}'_{nm}$  and  $\bar{e}_{nm}$  denote the transverse (to  $z$ ) electric vector mode functions for the  $TE_{nm}$  and  $TM_{nm}$  modes, respectively (with  $TE$  and  $TM$  being defined with respect to  $z$ ). Likewise, the  $\beta_{nm}$  and  $\beta_{nm}'$  denote the propagation constants of the  $TE_{nm}$  and  $TM_{nm}$  modes, respectively. Also,  $n$  and  $m$  refer to the modal indices associated with the transverse eigenvalues (in  $x$  and  $y$  for the rectangular waveguide case, or in  $\phi$  and  $\rho$  for the circular waveguide case) associated with the waveguide eigenfunctions or modes. It is noted that  $e_{znm}$  is the  $\hat{z}$ -component of the  $TM_{nm}$  modal electric field; clearly,  $e'_{znm}$  for the corresponding  $TE_{nm}$  case vanishes by definition. The superscripts + and - in (8) refer to modes propagating in the  $\hat{z}$  and  $-\hat{z}$  directions, respectively. It is convenient to define the magnetic field  $\bar{H}_g^{\pm}$  in the waveguide region following the representation for the electric field  $\bar{E}_g^{\pm}$  in (8); thus [13],

$$\bar{H}_g^{\pm} = \sum_{mn} [A_{nm}^{\pm} (\pm \bar{h}'_{nm} + \bar{h}_{znm} \hat{z}) e^{\mp j\beta_{nm} z} + B_{nm}^{\pm} (\pm \bar{h}_{nm}) e^{\mp j\beta_{nm} z}] . \quad (9)$$

The  $A_{nm}^{\pm}$  and  $B_{nm}^{\pm}$  in (8) and (9) are the modal coefficients. If  $\bar{E}^{ro}(P)$  denotes the electric field at  $P$  exterior to the waveguide region, which is radiated by the modes that impinge on the open end, then the scattering matrix  $[S_{12}]$  relates  $\bar{E}^{ro}$  to  $\bar{E}_g^+$  as follows:

$$\begin{bmatrix} E_x^{ro} \\ E_y^{ro} \\ E_z^{ro} \end{bmatrix} = \begin{bmatrix} [S_x^{ro'}] & [S_x^{ro}] \\ [S_y^{ro'}] & [S_y^{ro}] \\ [S_z^{ro'}] & [S_z^{ro}] \end{bmatrix} \begin{bmatrix} [A_{nm}^+] \\ [B_{nm}^+] \end{bmatrix} , \quad (10)$$

where

$$\bar{E}^{ro}(p) = E_x^{ro} \hat{x} + E_y^{ro} \hat{y} + E_z^{ro} \hat{z} , \quad (11)$$

and

$$[S_{12}] = \begin{bmatrix} [S_x^{ro'}] & [S_x^{ro}] \\ [S_y^{ro'}] & [S_y^{ro}] \\ [S_z^{ro'}] & [S_z^{ro}] \end{bmatrix} \quad (12)$$

with

$$\begin{bmatrix} S_x^{ro'} \\ S_y^{ro'} \\ S_z^{ro'} \end{bmatrix} = [S_{x01}^' \ S_{x02}^' \ \dots \ S_{x11}^' \ S_{x12}^' \ \dots \ S_{xnm}^' \ \dots] , \quad (13a)$$

and

$$\begin{bmatrix} S_x^{ro} \\ S_y^{ro} \\ S_z^{ro} \end{bmatrix} = [S_{x01} \ S_{x02} \ \dots \ S_{x11} \ S_{x12} \ \dots \ S_{xnm} \ \dots] . \quad (13b)$$

The scattering matrix  $[S_{21}]$  describes the transformation or the coupling of the incident plane wave field into the waveguide modes as illustrated in Figure 4. It is clear that  $[S_{21}]$  can therefore relate  $\bar{E}_g^i$  to  $\bar{E}^i$  as

$$\begin{bmatrix} [A_{nm}^-] \\ [B_{nm}^-] \end{bmatrix} = \begin{bmatrix} [S'_{\theta nm}] & [S'_{\phi nm}] \\ [S_{\theta nm}] & [S_{\phi nm}] \end{bmatrix} \begin{bmatrix} A_\theta \\ A_\phi \end{bmatrix} \quad (14)$$

where

$$[S_{21}] = \begin{bmatrix} [S'_{\theta nm}] & [S'_{\phi nm}] \\ [S_{\theta nm}] & [S_{\phi nm}] \end{bmatrix} \quad . \quad (15)$$

It is noted that the problem of determining  $[S_{21}]$  is related to the problem of determining  $[S_{12}]$  via reciprocity if  $P$  is moved to the far zone in the reciprocal (or  $[S_{12}]$ ) problem to correspond to a local plane wave incidence in the original (or  $[S_{21}]$ ) problem. The precise relationship between  $[S_{21}]$  and  $[S_{12}]$  will be discussed in Section III-B.

The scattering matrix  $[S_{22}]$  is a modal reflection coefficient matrix which is associated with the interaction illustrated in Figure 5. In particular, the elements of  $[S_{22}]$  describe the reflection coefficients associated with the  $TE_{nm}$  and  $TM_{nm}$  modes reflected back from the open end (at  $z=0$ ) into the waveguide region ( $z<0$ ) when either a  $TE_{pq}$  or a  $TM_{pq}$  mode is incident on that open end from within the waveguide. Thus, the matrix  $[S_{22}]$  relates  $\bar{E}_g^-$  to  $\bar{E}_g^+$  as follows:

$$\begin{bmatrix} [A_{nm}^-] \\ [B_{nm}^-] \end{bmatrix} = \begin{bmatrix} [R_{nm;pq}^{hh}] & [R_{nm;pq}^{he}] \\ [R_{nm;pq}^{eh}] & [R_{nm;pq}^{ee}] \end{bmatrix} \begin{bmatrix} [A_{pq}^+] \\ [B_{pq}^+] \end{bmatrix} \quad (16)$$

where

$$[S_{22}] = \begin{bmatrix} [R_{nm;pq}^{hh}] & [R_{nm;pq}^{he}] \\ [R_{nm;pq}^{eh}] & [R_{nm;pq}^{ee}] \end{bmatrix} . \quad (17)$$

The meaning of  $R_{nm;pq}^{he}$ , for example, in (17) is the following. A  $TM_{pq}$  (or e type) mode with modal amplitude  $B_{pq}^+$  which is incident at the open end is partly transformed (or coupled) into a reflected  $TE_{nm}$  (or h type) mode with modal amplitude  $A_{nm}^- = R_{nm;pq}^{he} B_{pq}^+$ .

The scattering matrix  $[S_\Gamma]$ , like  $[S_{22}]$ , is also a reflection coefficient type matrix which is associated with the termination at  $z=-L$  (see Figure 5). Thus, one may write:

$$\begin{bmatrix} [A_{nm}^+] \\ [B_{nm}^+] \end{bmatrix} = \begin{bmatrix} [\Gamma_{nm;pq}^{hh}] & [\Gamma_{nm;pq}^{he}] \\ [\Gamma_{nm;pq}^{eh}] & [\Gamma_{nm;pq}^{ee}] \end{bmatrix} \begin{bmatrix} [A_{pq}^-] \\ [B_{pq}^-] \end{bmatrix} \quad (18)$$

where

$$[S_\Gamma] = \begin{bmatrix} [\Gamma_{nm;pq}^{hh}] & [\Gamma_{nm;pq}^{he}] \\ [\Gamma_{nm;pq}^{eh}] & [\Gamma_{nm;pq}^{ee}] \end{bmatrix} . \quad (19)$$

As before,  $\Gamma_{nm;pq}^{he}$  relates  $A_{nm}^+$  to  $B_{pq}^-$  via  $A_{nm}^+ = \Gamma_{nm;pq}^{he} B_{pq}^-$ .

At any given operating frequency, the waveguide region can support a finite number of propagating modes and an infinite number of evanescent (non-propagating) modes. Therefore, the matrices  $[S_{12}]$ ,  $[S_{21}]$ ,  $[S_{22}]$  and  $[S_\Gamma]$  are of infinite order to include the infinite number of evanescent modes. However, even though the matrices  $[S_{12}]$ ,  $[S_{21}]$ ,  $[S_{22}]$  and  $[S_\Gamma]$  are of infinite order in a formal sense, one needs to retain only a finite number of the elements of these

scattering matrices in practice, because the distance "L" shown in Figure 1 is generally large enough to where the infinite number of evanescent modes generated at junction (I) contribute negligibly at junction (II), and vice versa. The finite number of elements of the scattering matrices which are retained in practice thus correspond to only the finite number of all the propagating (or non evanescent) modes which can exist within the waveguide region. If the distance L in Figure 1 is small enough so that the "lower order" evanescent modes become important, then one must include these modes but one can still ignore the contribution from all the "higher order" evanescent modes when the latter is negligible. In either case, one always retains a finite number of elements in the scattering matrices which may otherwise formally be of infinite order. The number of evanescent modes which need to be included in the special case when L is very small is dictated by how many of these are needed for convergence; it has been known from experience that even when L → 0, the inclusion of only three to five evanescent modes are sufficient for convergence.

It is observed from Figure 1 that one may describe the field scattered by the inlet as consisting of two parts. The entire scattered field thus consists of the contribution from just the open end by itself, together with the field radiated from the open end as a result of all the interactions between the open end and the termination that arises from the incident field which is coupled into the waveguide region. Referring to Figure 7, it is observed that the incident electric field  $[E^i] = [A_\phi^\theta]$  at the open end is scattered by junction (I) to produce a scattered field  $[E^{s0}]$  given by (5) as

$$[E^{SO}] = [S_{11}][E^i] \quad (20)$$

where

$$[E^{SO}] = \begin{bmatrix} E_x^{SO} \\ E_y^{SO} \\ E_z^{SO} \end{bmatrix} . \quad (21)$$

A part of the incident field is coupled at (I) into the waveguide region; this field then becomes incident at junction (II) from which it is subsequently reflected. The field reflected from junction (II) is incident back at (I) where it undergoes further scattering into the exterior and interior regions, and so on, thus giving rise to multiple wave interactions between junctions (I) and (II). The fields resulting from these multiple interactions may be expressed in a convergent Neumann series as done by Pace and Mittra [14]; however, an alternate procedure based on a self-consistent method leads directly to the same result. The latter self-consistent MSM based analysis will be employed here. Let  $[E_{12}]$  represent the total field incident at (I) from (II) after taking all the multiple interactions into account. Likewise, let  $[E_{21}]$  represent the total field incident at (II) from (I) after taking all the multiple interactions into consideration. Then, the total scattered field in the exterior region denoted by  $[E^S]$  consists of a superposition of  $[E^{SO}]$  and  $[E^{MO}]$ , where  $[E^{MO}]$  is the field scattered into the exterior region when  $[E_{12}]$  is incident on (I). Therefore,

$$[E^S] = [E^{SO}] + [E^{MO}] \quad (22)$$

where  $[E^{MO}]$  may be expressed as

$$[E^{MO}] = [S_{12}] [E_{12}] \Big|_{z=0} . \quad (23)$$

The expressions for  $[E_{12}]$  and  $[E_{21}]$  may be written in terms of  $[S_{21}]$  and  $[S_{22}]$ ; namely,

$$[E_{21}] \Big|_{z=0} = [S_{21}] [E^i] + [S_{22}] [E_{12}] \Big|_{z=0} \quad (24)$$

and

$$[E_{12}] \Big|_{z=0} = [P] [S_R] [P] [E_{21}] \Big|_{z=0} \quad (25)$$

in which  $[S_R]$  denotes the reflection coefficient scattering matrix pertaining to junction (II) as defined in (19), and  $[P]$  is a diagonal matrix accounting for the phase delay along the length  $L$  between junctions (I) and (II). Eliminating  $[E_{12}]$  between (24) and (25) yields

$$([I] - [S_{22}] [P] [S_R] [P]) [E_{21}] \Big|_{z=0} = [S_{21}] [E^i] , \quad (26)$$

where  $[I]$  is an infinite order identity matrix. Hence, it follows that

$$[E_{21}] \Big|_{z=0} = ([I] - [S_{22}] [P] [S_R] [P])^{-1} [S_{21}] [E^i] . \quad (27)$$

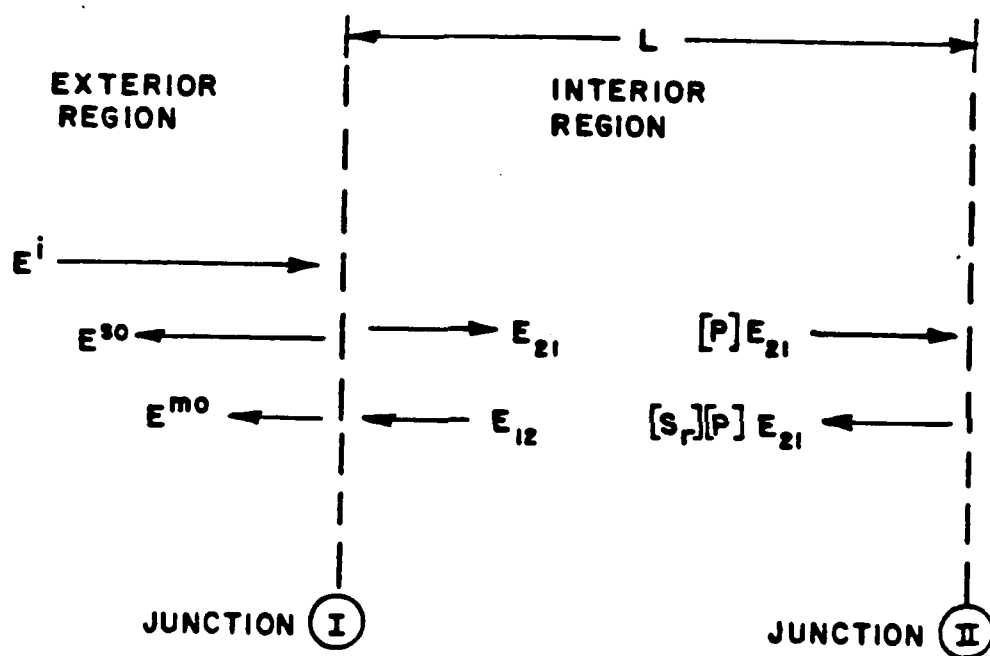


Figure 7. Multiple interactions between junctions I and II for calculating the total backscattered field.

From (25) and (27),  $[E_{12}] \Big|_{z=0}$  becomes

$$[E_{12}] \Big|_{z=0} = [P][S_T][P]([I] - [S_{22}][P][S_T][P])^{-1}[S_{21}][E^i] . \quad (28)$$

Incorporating the above result into (23) yields

$$[E^{mo}] = [S_{12}][P][S_T][P]([I] - [S_{22}][P][S_T][P])^{-1}[S_{21}][E^i] . \quad (29)$$

Finally, combining (20) and (29) according to (22) leads to the self-consistent expression for the total scattered field  $[E^s]$  as

$$[E^s] = \{[S_{11}] + [S_{12}][P][S_T][P]([I] - [S_{22}][P][S_T][P])^{-1}[S_{21}]\}[E^i] . \quad (30)$$

The scattering matrices  $[S_{11}]$ ,  $[S_{12}]$ ,  $[S_{21}]$ , and  $[S_{22}]$  can be found in a relatively simple manner via asymptotic high frequency techniques (such as GTD, UTD, ECM or PTD), as shown in the next section.

Before proceeding further with the development of the expressions for the elements of the scattering matrices, it is important to mention that these scattering matrices are somewhat different from the conventional scattering matrices due to the fact that they contain range information (because they are valid for field calculations in the near zone of the inlet opening). Secondly, one notes that the present analysis is restricted to angles of incidence and scattering which are about  $60^\circ$  or less from the forward axis of the inlets.

In the far zone calculations, it is more common to define the scattering matrices so that they are independent of the range (i.e., the far zone distance from the origin of the coordinate system shown in Figure 1). The alternative, more common definitions for the generalized scattering matrices used in far zone calculations are included in Appendix V for the sake of completeness and convenience. It is noted that the results calculated from (30) in the limit as the near zone point is allowed to recede to the far zone should reduce to those obtained from the far zone scattering described in Appendix V.

### III. ANALYSIS FOR THE ELEMENTS OF THE SCATTERING MATRICES

#### A. Development of $[S_{11}]$

The scattering matrix  $[S_{11}]$  describes the field scattered from only the open end (at  $z=0$ ) of the geometries in Figure 1 when these geometries are illuminated by an external source. In the present study, the illumination is an external EM plane wave and the observation point  $P$  is also located in the exterior region; furthermore,  $P$  could lie either in the near zone or the far zone of the aperture (at  $z=0$ ) corresponding to the open end of the inlet configurations in Figure 1. According to the ray picture afforded by the GTD, the fields scattered by just the open end arise only from the diffraction of the incident wave by the rim corners and edges (at the inlet opening). Thus, let  $\bar{E}^{so}$  and  $\bar{H}^{so}$  denote the electric and magnetic fields, respectively, which are singly diffracted by the inlets in

Figure 1; in addition, multiply edge diffracted fields ( $\bar{E}^{sm}$ ,  $\bar{H}^{sm}$ ), which are produced by rays that undergo multiple diffractions across the aperture, also contribute to the scattered field at P. However, in the present study, only  $\bar{E}^{so}$  and  $\bar{H}^{so}$  are included; whereas,  $\bar{E}^{sm}$  and  $\bar{H}^{sm}$  are not considered. These multiple interactions may become important if the aperture dimensions are not sufficiently large in terms of the wavelength.

Actually,  $\bar{E}^{so}$  (and  $\bar{H}^{so}$ ) is the sum of the fields of all the singly diffracted rays which are initiated at various points on the rim edge by the incident field in accordance with the law of edge diffraction, which is a consequence of one of the basic postulates of the GTD. That postulate deals with Keller's generalization of Fermat's principle to include diffracted rays. In the case of the rectangular inlet opening, the rays diffracted from the corners of the inlet rim also contribute to the diffracted fields  $\bar{E}^{so}$  and  $\bar{H}^{so}$  in addition to the edge diffracted rays. The points of edge diffraction can, in general, migrate around the rim as a function of the observation point and incident field direction. In the case of the circular inlet the entire rim edge or portions of the rim can contribute to the edge diffracted field for certain observation points; in such instances there exists a caustic of the edge diffracted rays at or near P and the GTD fails because of the continuum of rays that must now reach P in this case. Also, away from the caustics of diffracted rays there can, in general, be four points of diffraction on the circular rim which contribute to the field  $\bar{E}^{so}$  when it is evaluated for a certain set of oberservation points P;

whereas, at other observation points  $P$  only two points of edge diffraction on the circular rim contribute to  $\bar{E}^{SO}$ . Again, a direct application of the GTD fails in the range of observation points within which such a disappearance of four points into two points of diffraction occurs on the rim edge. Typically, such a disappearance of rays results when three of the four points merge together. Conversely, one can also experience a transition from two to four rays diffracted to  $P$ . In order to overcome some of the above problems in the GTD which occur for a certain range of aspects, it is necessary to use the equivalent current method (ECM). In the case of the rectangular inlet, the use of ECM also automatically takes into account the presence of the corners at the inlet opening. It is noted, of course, that the effect of the corners is taken into consideration in an approximate fashion in the ECM; such an approximation is also present if one employs the GTD approach alone since the GTD corner diffraction coefficient that is available at this time is based partly on heuristic arguments [3] and is thus approximate. In regions where GTD is valid, the ECM generally blends into the GTD solution provided the inlet opening is sufficiently large in terms of the wavelength. Thus, one could switch over from the ECM based solution to a GTD solution away from regions where GTD fails. Such a switch would yield a numerically more efficient approach for evaluating the elements of  $[S_{11}]$  because the ECM involves an integration around the rim edge (of the inlet), whereas the GTD involves no integration. In the present work, this kind of switching has not been used for the calculation of the  $[S_{11}]$

matrix. The ECM method is employed at all aspects of interest in this study.

In the ECM [3-6], equivalent currents  $I_{eq}$  and  $M_{eq}$  of the electric and magnetic type, respectively, are located at the rim edge as shown in Figure 8 for an arbitrarily shaped inlet opening. These equivalent rim currents radiate in "free space" to produce the scattered field. As indicated in [3,6],  $I_{eq}$  and  $M_{eq}$  are actually deduced from GTD. Thus, even though GTD itself is not valid within diffracted ray caustic regions, it can still indirectly provide the strengths of the equivalent currents which radiate fields that remain valid within those caustic regions in the ECM based approach. From [6],

$$I_{eq}(\hat{\ell}') = -Y_0 \sqrt{\frac{8\pi}{jk}} \frac{D_S(\psi, \psi'; \beta_0, \beta)}{|\sqrt{\sin\beta_0 \sin\beta}|} (\bar{E}^i \cdot \hat{\ell}') \quad (31)$$

and

$$M_{eq}(\hat{\ell}') = -Z_0 \sqrt{\frac{8\pi}{jk}} \frac{D_h(\psi, \psi'; \beta_0, \beta)}{|\sqrt{\sin\beta_0 \sin\beta}|} (\bar{H}^i \cdot \hat{\ell}') , \quad (32)$$

where

$Z_0$  = free space impedance, and

$Y_0 = 1/Z_0$  .

One can incorporate  $I_{eq}$  and  $M_{eq}$  of (31) and (32) into the radiation integral for calculating the scattered field  $\bar{E}^{so}$ ; namely [1,6]:

$$E^{so}(P) \approx \frac{jkZ_0}{4\pi} \int_{\text{rim}} d\ell' [\hat{R} \times \hat{R} \times I_{eq}(\ell') \hat{\ell}' + Y_0 \hat{R} \times M_{eq}(\ell') \hat{\ell}'] \frac{e^{-jkR}}{R} ; \quad (33)$$

in which

$$d\ell' = \hat{\ell}' d\ell' = \begin{cases} +\hat{x}dx', \text{ or } +\hat{y}dy', \text{ for } y=(0;b), \text{ or } x=(0;a), \\ \text{respectively, in the case of the rectangular slit.} \\ +\hat{\phi}' a d\phi' \text{ in the case of the circular inlet.} \end{cases}$$

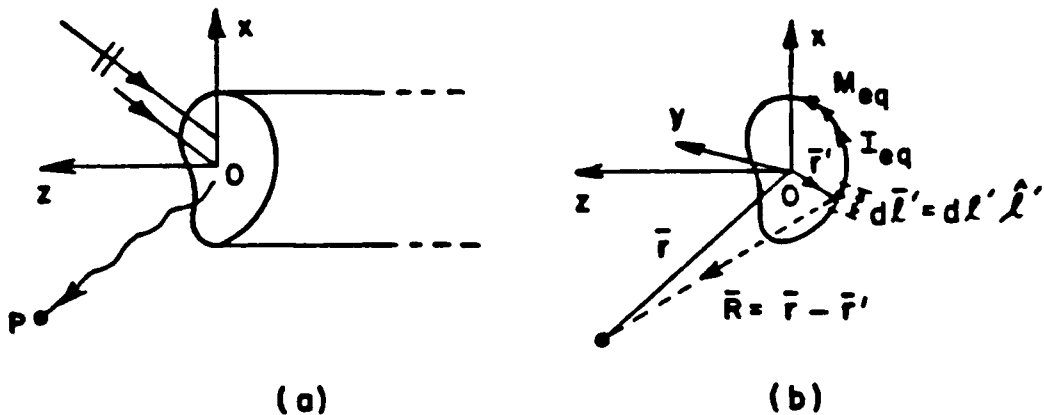


Figure 8. Scattering from the open end and its equivalent problem.

$\bar{r}$  = position vector from 0 to P ;

$\bar{r}'$  = position vector from 0 to mid-point of the rim element  $d\bar{r}'$  (see Figure 8(b));

$\bar{R} = [\bar{r} - \bar{r}']$  ;

The angles  $\psi$ ,  $\psi'$ ,  $\beta_0$  and  $\beta$  are associated with the soft and hard edge diffraction coefficients  $D_s$  and  $D_h$  which are present in (31) and (32).

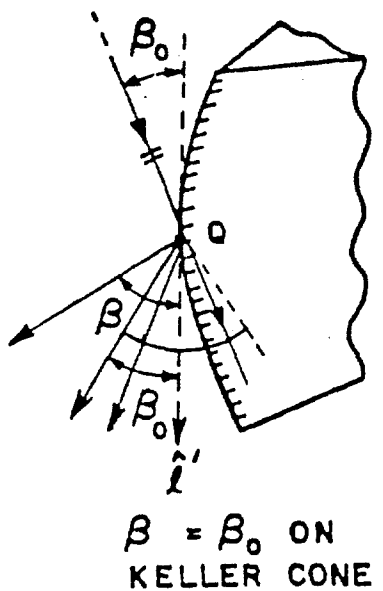
In particular, these edge diffraction coefficients  $D_{s,h}(\psi, \psi'; \beta_0, \beta)$  in (31) and (32) are defined for each point of diffraction on the rim edge, and they are associated with an equivalent edge of a half plane which is tangent to both the rim edge as well as the inlet surface at each point of diffraction on the rim. Assuming that Q is any such point of diffraction on an edge in an arbitrary curved wedge, the meaning of  $\beta_0$ ,  $\beta$ ,  $\psi$  and  $\psi'$  with respect to the point of diffraction Q becomes clear from Figures 9(a) and 9(b) for this wedge configuration. Of course, the walls of the inlets or waveguides are assumed to be infinitesimally thin in the present work, so the wedge geometry in Figures 9(a) and 9(b) should be reduced to an edge in a curved or plane screen (n=2 case in Figure 9(b)) for the circular and rectangular inlets in the present instance; however, the meaning of  $\psi$ ,  $\psi'$ ,  $\beta_0$  and  $\beta$  is unchanged even when the wedge in Figures 9(a) and 9(b) collapses to an edge in a screen.

Finally, the equivalent currents  $I_{eq}$  and  $M_{eq}$  are valid provided one is observing the fields of these sources in directions away from the geometrical optics incident and reflection shadow boundaries [3,6]; under these conditions which are met in practice (since directions of incidence and scattering are restricted to  $60^\circ$  or so from the axis of

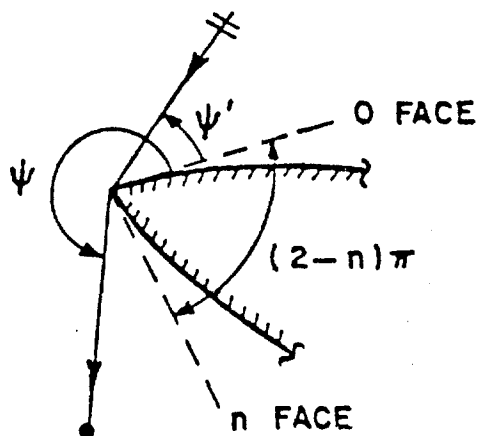
the inlets),  $D_s$  and  $D_h$  for the local half planes at each point of diffraction on the rim become [6]:

$$D_s(\psi, \psi'; \beta_0, \beta) = \frac{-e^{-j\pi/4}}{2\sqrt{2\pi k} \sqrt{\sin \beta_0 \sin \beta}} \cdot \left[ \sec\left(\frac{\psi - \psi'}{2}\right) \mp \sec\left(\frac{\psi + \psi'}{2}\right) \right]. \quad (34)$$

The use of (31), (32) and (34) into (33) together with  $\bar{E}^i$  of (1; 2(a); 2(b)) and  $\bar{H}^i = \hat{k}^i \times \gamma_0 \bar{E}^i$  allows one to easily identify  $[S_{11}]$  via (5) and (7). Thus



(a)



(b)

Figure 9. Diffraction by a wedge. The angles  $\beta_0$ ,  $\beta$ ,  $\psi'$  and  $\psi$  which occur in the edge diffraction coefficient.

$$\begin{aligned}
 S_{u\theta}^0 = & \frac{jkZ_0}{4\pi} \int_{\text{rim}(z=0)} d\hat{\ell}' \hat{u} \cdot [\hat{R} \times \hat{R} \times \hat{\ell}' (-Y_0 \sqrt{\frac{8\pi}{jk}} \frac{D_S(\psi, \psi'; \beta_0, \beta)}{|\sqrt{\sin\beta_0 \sin\beta}|} \hat{\ell}' \cdot \hat{\theta}^i) \\
 & - Y_0 \hat{R} \times \hat{\ell}' (-\sqrt{\frac{8\pi}{jk}} \frac{D_h(\psi, \psi'; \beta_0, \beta)}{|\sqrt{\sin\beta_0 \sin\beta}|} \hat{\ell}' \cdot \hat{\phi}^i)] \frac{e^{-jk\hat{\ell}' \cdot \hat{r}' - jkR}}{R}
 \end{aligned} \tag{35}$$

and

$$\begin{aligned}
 S_{u\phi}^0 = & \frac{jkZ_0}{4\pi} \int_{\text{rim}(z=0)} d\hat{\ell}' \hat{u} \cdot [\hat{R} \times \hat{R} \times \hat{\ell}' (-Y_0 \sqrt{\frac{8\pi}{jk}} \frac{D_S(\psi, \psi'; \beta_0, \beta)}{|\sqrt{\sin\beta_0 \sin\beta}|} \hat{\ell}' \cdot \hat{\phi}^i) \\
 & + Y_0 \hat{R} \times \hat{\ell}' (-\sqrt{\frac{8\pi}{jk}} \frac{D_h(\psi, \psi'; \beta_0, \beta)}{|\sqrt{\sin\beta_0 \sin\beta}|} \hat{\ell}' \cdot \hat{\theta}^i)] \frac{e^{-jk\hat{\ell}' \cdot \hat{r}' - jkR}}{R}
 \end{aligned} \tag{36}$$

with

$$\hat{u} = \begin{bmatrix} \hat{x} \\ \hat{y} \\ \hat{z} \end{bmatrix} \quad \text{and} \quad u = \begin{bmatrix} x \\ y \\ z \end{bmatrix} \quad .$$

Some typical results for the fields scattered by only the open end of circular and rectangular inlets are shown in Figures 10 - 15. The plane wave is incident on the open end from the direction  $(\theta^i; \phi^i)$ , and the near field is evaluated either for a fixed  $R$  and  $\theta^r$  with  $0 < \phi^r < 2\pi$ , or for a fixed  $R$  and  $\phi^r$  with  $|\phi^r| < 60^\circ$ . Here, the direction of scattering is specified by the set of angles  $(\theta^r; \phi^r)$  and  $R$  denotes the distance from the origin of the coordinate system (see Figure 1) to the near zone where the scattered field is observed. Again, near zone or near field implies that the observation (or field) point is located

within the "radiating" near zone of the inlet opening. It is clear from these figures that the "total" scattered field ( $\hat{E}^{SO} = \hat{x}E_x^{SO} + \hat{y}E_y^{SO} + \hat{z}E_z^{SO}$ ) generally contains a peak around ( $\theta^r = \theta^i$  and  $\phi^r = \pi + \phi^i$ ); this is to be expected since it is like a specular direction where the fields diffracted from the entire rim (at the open end) contribute almost in phase. In these figures, all the lengths are expressed in terms of the wavelength.

In order to show the effects of multiple interactions of the rays across the aperture, it is useful to illustrate the on-axis backscattered field for a circular inlet as calculated previously in [9] which includes up to first-order, second-order, and third-order diffractions as well as the effects of all the multiple interactions. These results as shown in Figure 16 are calculated from an asymptotic high frequency ECM based approach and are compared with an exact solution based on the Wiener-Hopf technique. It is seen that for  $a/\lambda > 0.5$ , the backscattered field starts to settle down and approaches (within 2 dB) the values based on including only first-order diffraction. As the electrical dimensions of the inlet opening increases, the results based on using only first-order diffraction will become more and more accurate. In the computer code associated with this report, the first-order and the second order edge diffractions are included to show the effect of the edges.

## B. Development of $[S_{21}]$

The scattering matrix  $[S_{21}]$  describes the transmission or coupling of the incident plane wave field into the waveguide modes as illustrated in Figure 4 and described in (14) and (15).

For later convenience, let the waveguide in Figure 4 be excited by an electric current moment  $\bar{d}_e$  which lies in the exterior but near zone region of the inlet (waveguide) opening as shown in Figure 17. The  $[S_{21}]$  will be developed here for the coupling of the fields of the exterior source  $\bar{d}_e$  into the interior waveguide region via the inlet opening as in Figure 17; this more general situation reduces to the special case of plane wave incidence on the inlet opening as in Figure 1 if the source  $\bar{d}_e$  is allowed to recede to infinity.

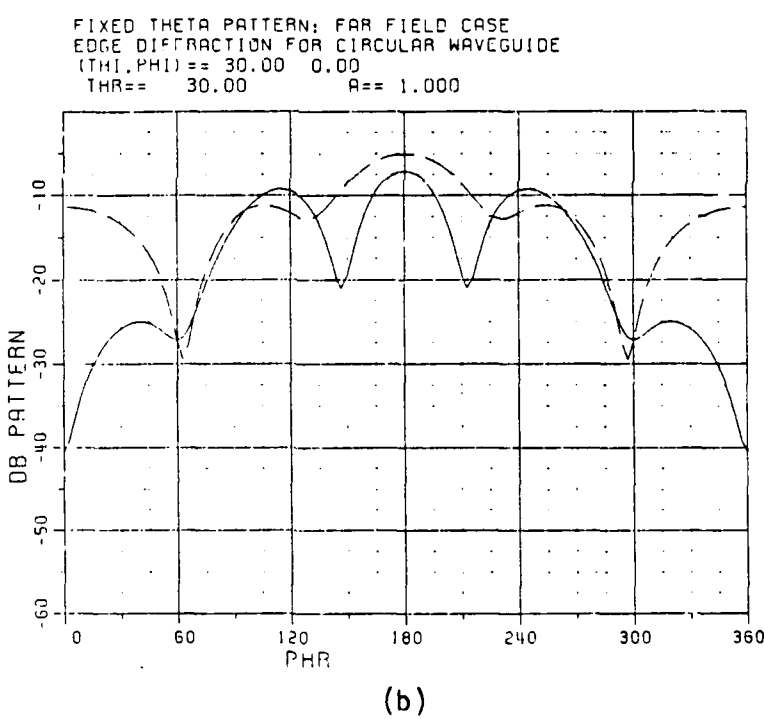
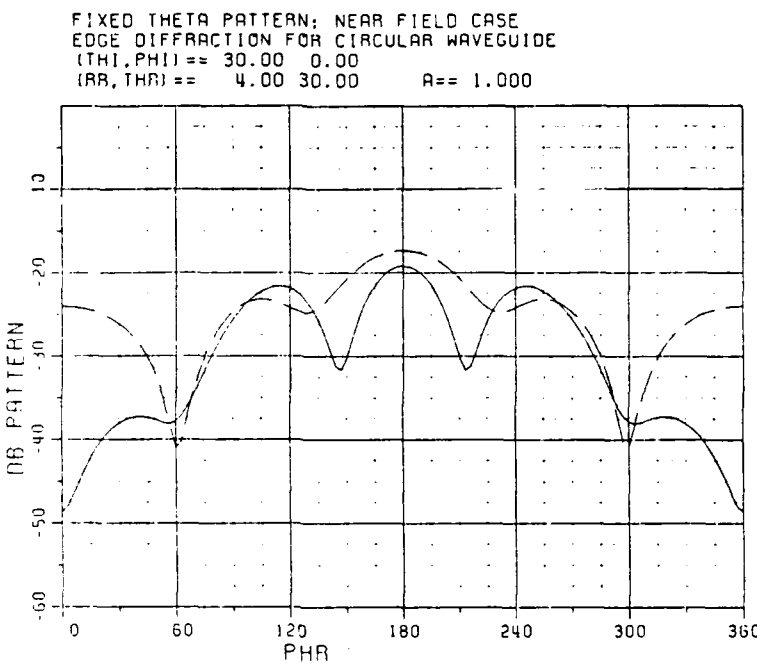
The field  $\bar{E}_{in}$  which is coupled into the waveguide region by  $\bar{d}_e$  in Figure 17 may be expressed as in (8) by

$$\bar{E}_{in} = \sum_{mn} [A_{nm}^- \bar{e}_{nm}^- e^{+j\beta_{nm}^* z} + B_{nm}^- (\bar{e}_{nm}^- - \hat{z} \bar{e}_{znm}^-) e^{+j\beta_{nm}^* z}] . \quad (37)$$

The associated magnetic field  $\bar{H}_{in}$  is likewise given via (9) as

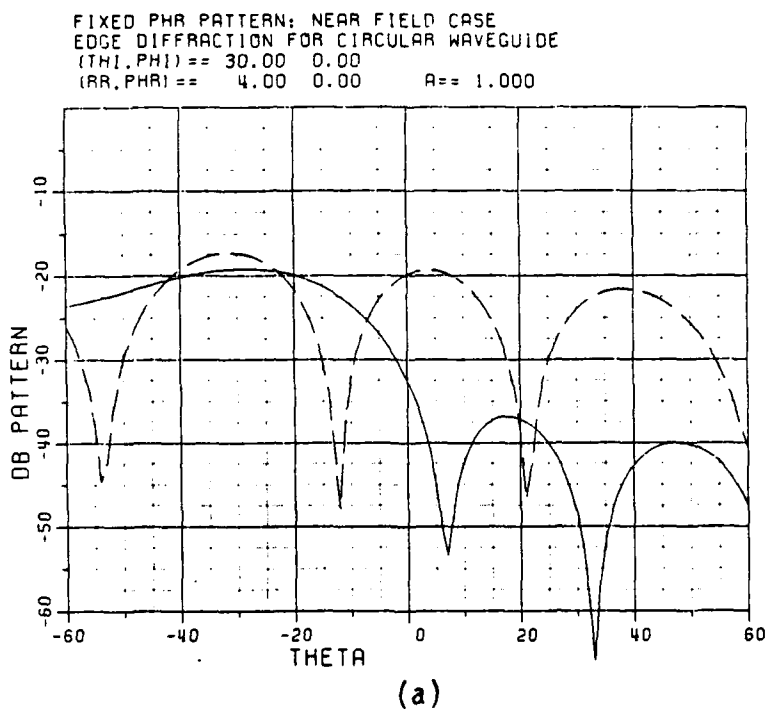
$$\bar{H}_{in} = \sum_{mn} [A_{nm}^- (-\bar{h}_{nm}^- + \bar{h}_{znm}^-) e^{+j\beta_{nm}^* z} + B_{nm}^- (-\bar{h}_{nm}^-) e^{+j\beta_{nm}^* z}] . \quad (38)$$

The modal coupling or transmission coefficients  $A_{nm}^-$  and  $B_{nm}^-$  in (37) and (38) may be found from the equivalent problem in Figure 17(c) which illustrates an equivalent surface and line source distribution at  $z=0$  within an infinite waveguide (which is an extension of the

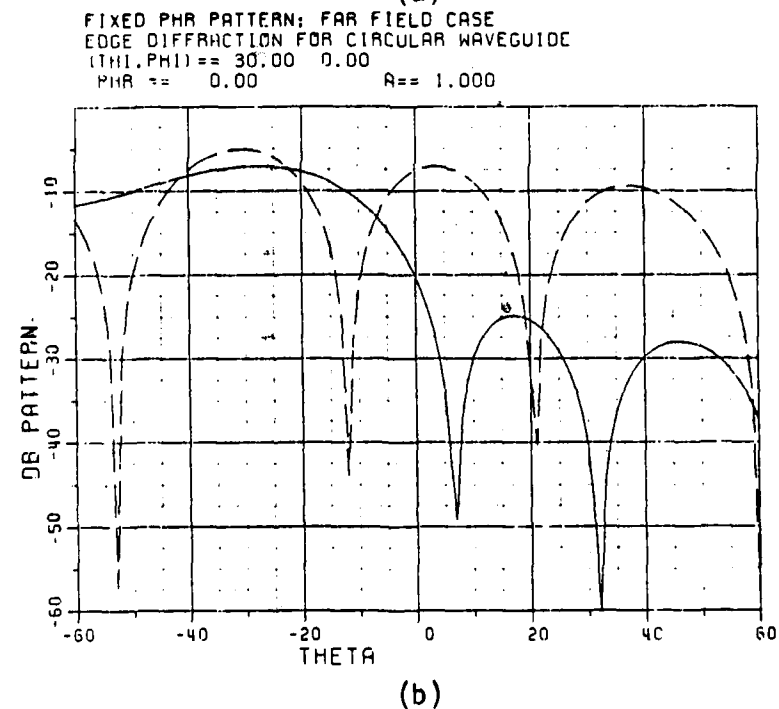


— total field due to  $E_\theta^i$     - - - total field due to  $E_\phi^i$

Figure 10. A comparison of the far zone and near zone edge diffraction from the open end of circular inlet for a  $30^\circ$  cone scan.



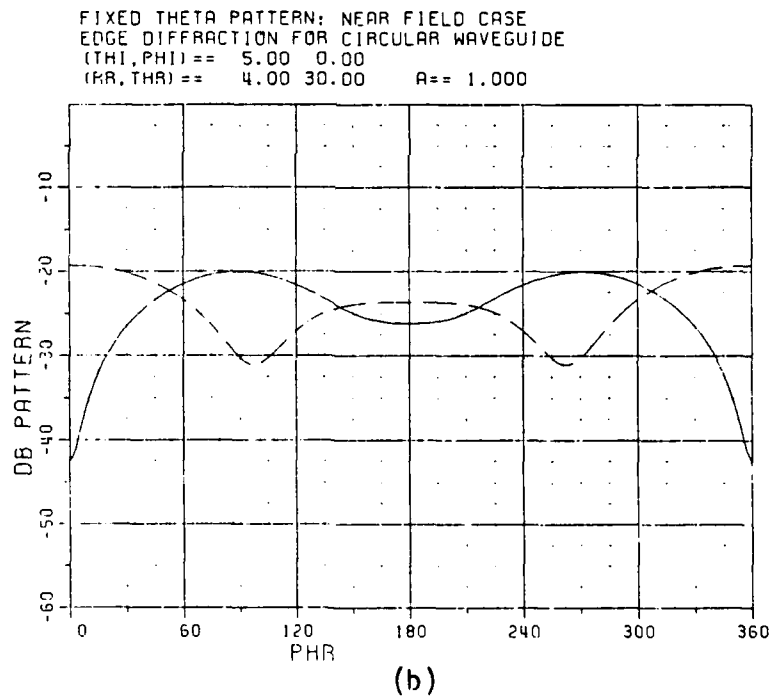
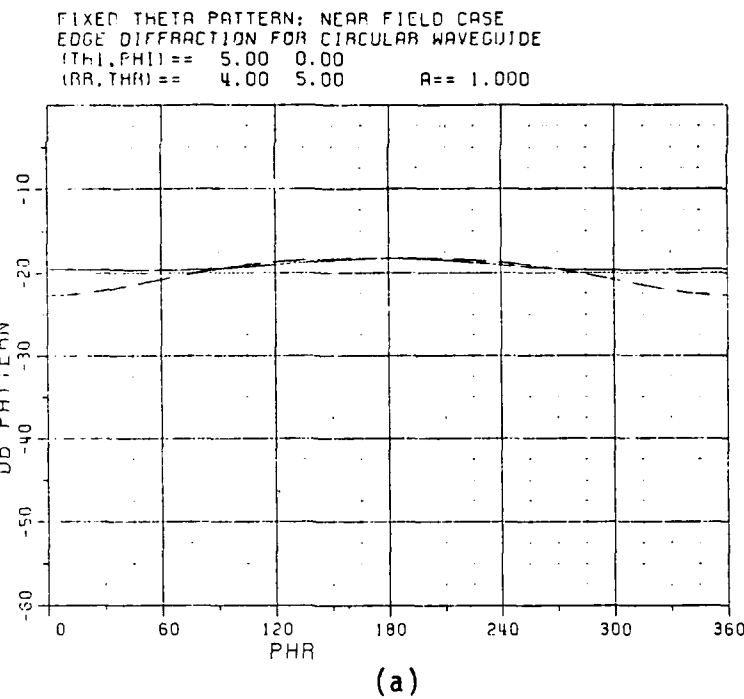
(a)



(b)

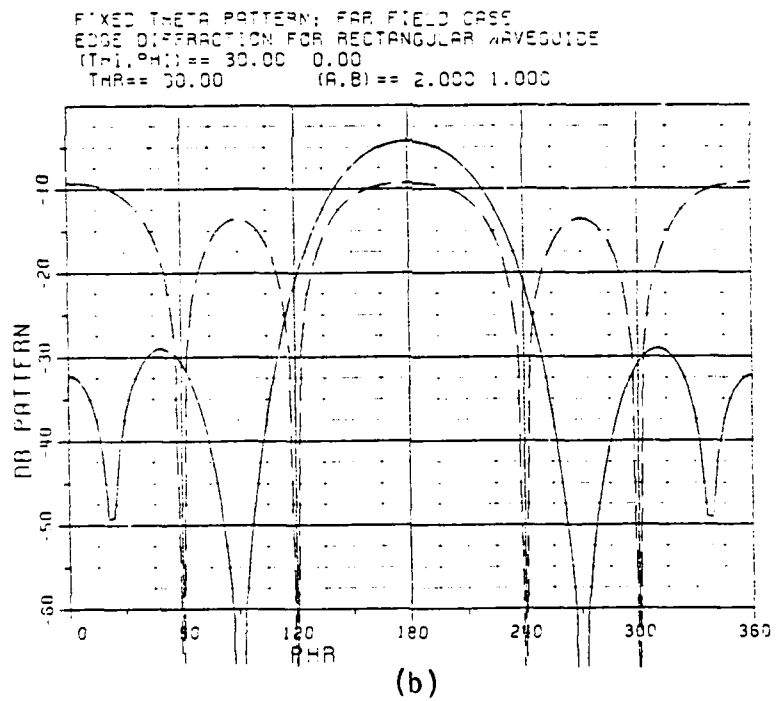
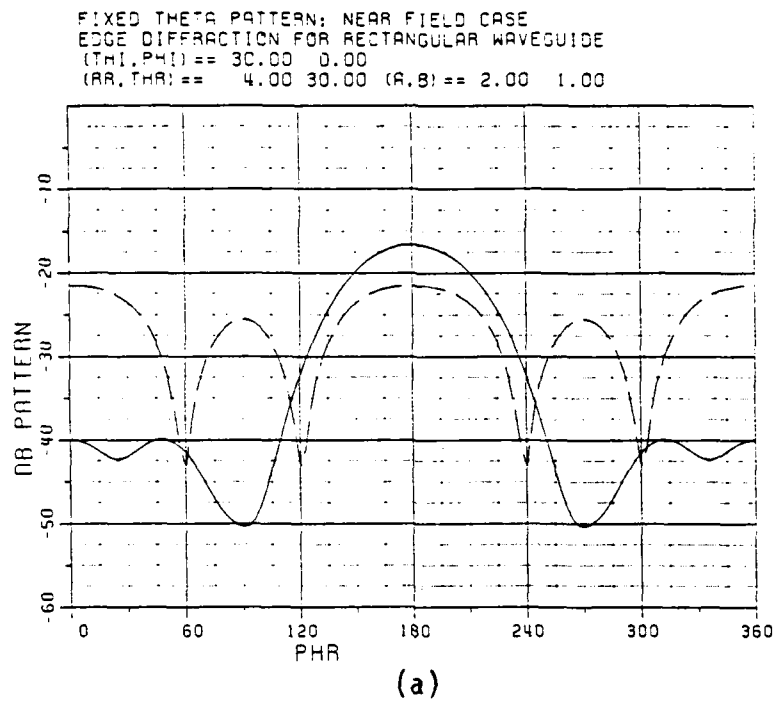
— total field due to  $E_\theta^1$     - - - total field due to  $E_\phi^1$

Figure 11. A comparison of the far zone and near zone edge diffraction from the open end of circular inlet for  $\phi = 0$  cut.



— total field due to  $E_\theta^i$     - - - total field due to  $E_\phi^i$

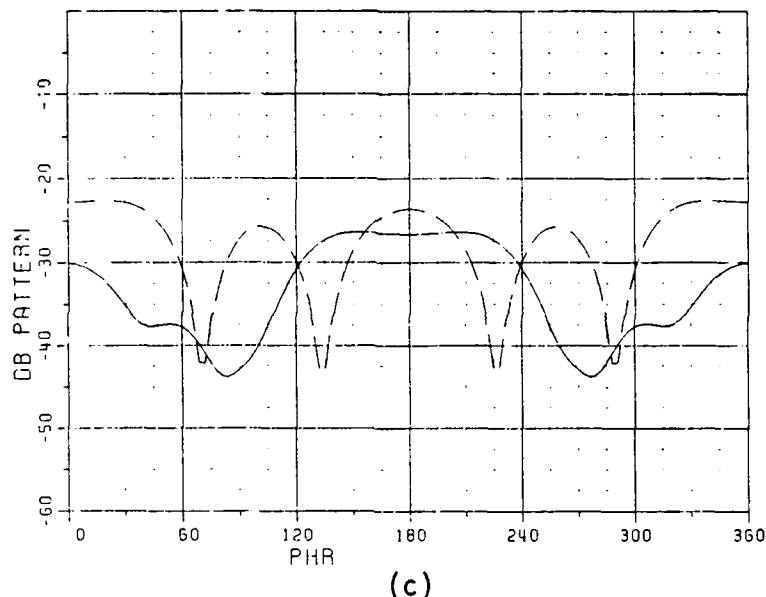
Figure 12. A comparison for  $\theta = 5^\circ$  and  $\theta = 30^\circ$  cone scan patterns with  $\theta_f^i = 5^\circ$  plane wave incidence.



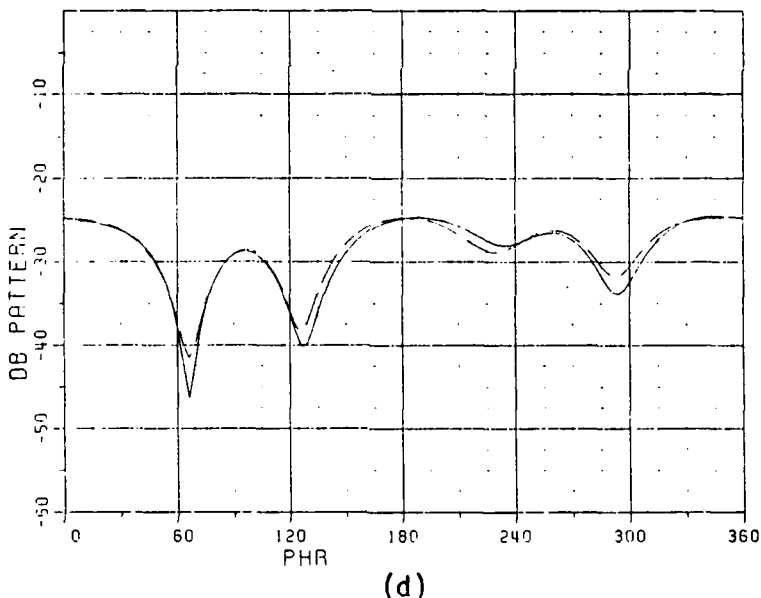
— total field due to  $E_\theta^i$     - - - total field due to  $E_\phi^i$

Figure 13. A comparison of the far zone and near zone edge diffraction from the open end of a rectangular inlet and also the near zone  $30^\circ$  cone scan patterns for different incident angles.

FIXED THETA PATTERN: NEAR FIELD CASE  
 EDGE DIFFRACTION FOR RECTANGULAR WAVEGUIDE  
 $(THI, PHI) == 5.00 0.00$   
 $(RR, THRI) == 4.00 30.00$   $(A, B) == 2.000 1.000$



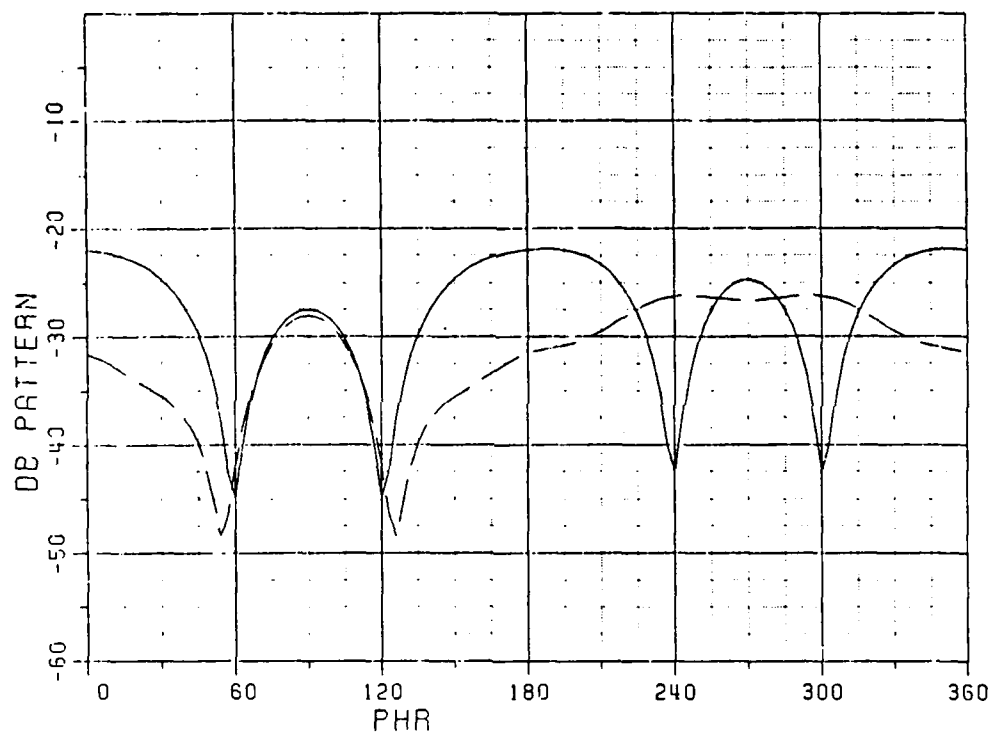
FIXED THETA PATTERN: NEAR FIELD CASE  
 EDGE DIFFRACTION FOR RECTANGULAR WAVEGUIDE  
 $(THI, PHI) == 5.00 45.00$   
 $(RR, THRI) == 4.00 30.00$   $(A, B) == 2.000 1.000$



— total field due to  $E_\theta^i$     - - - total field due to  $E_\phi^i$

Figure 13. (Continued).

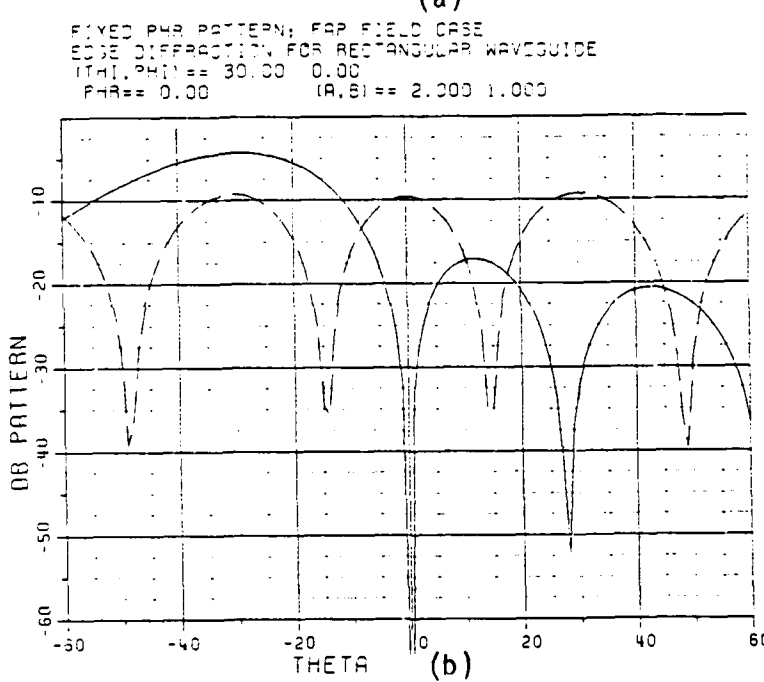
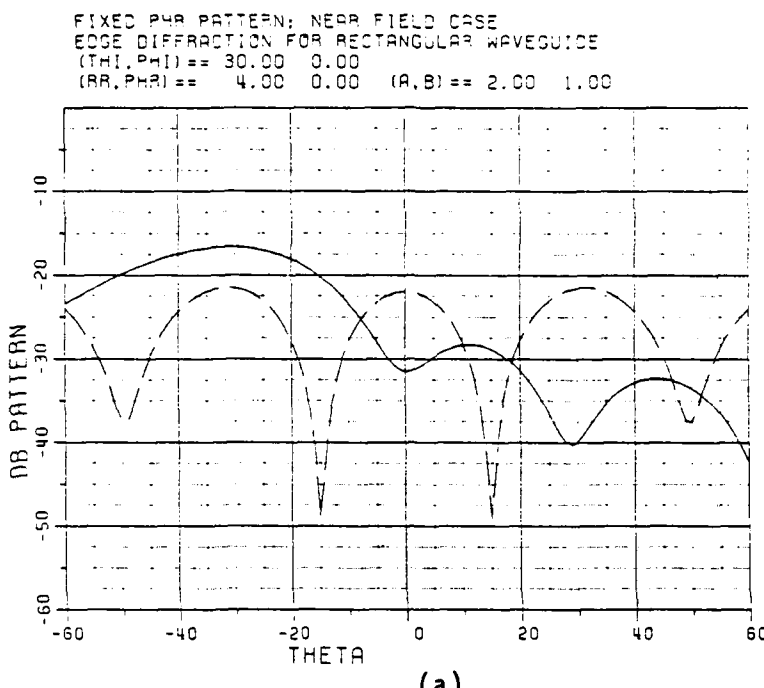
FIXED THETA PATTERN; NEAR FIELD CASE  
 EDGE DIFFRACTION FOR RECTANGULAR WAVEGUIDE  
 $(\Theta_{HI}, \Phi_{HI}) = 5.00 \ 90.00$   
 $(RR, THR) = 4.00 \ 30.00 \quad (A, B) = 2.000 \ 1.000$



(e)

— total field due to  $E_\theta^i$     - - - total field due to  $E_\phi^i$

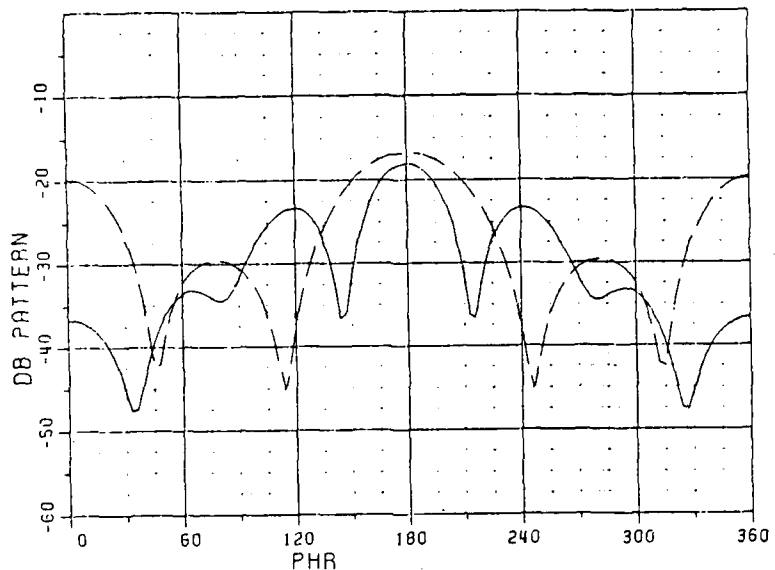
Figure 13. (Continued).



— total field due to  $E_\theta^i$     - - - total field due to  $E_\phi^i$

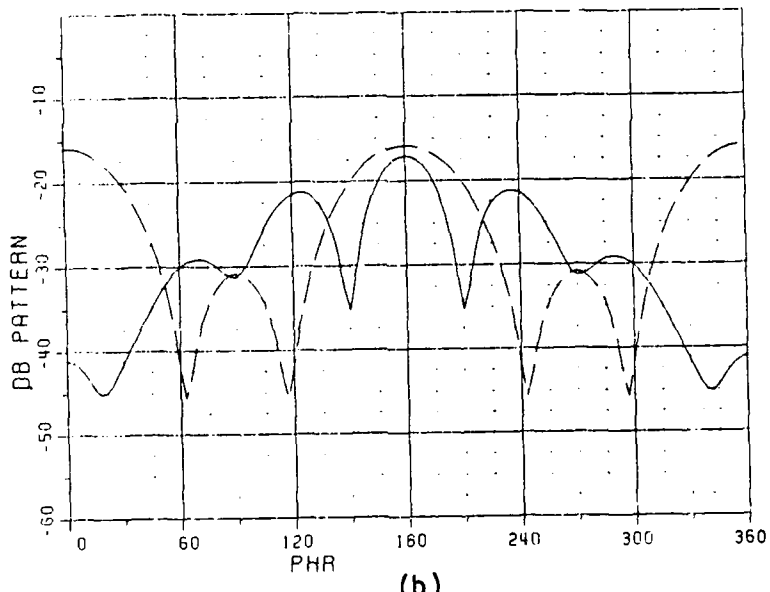
Figure 14. A comparison of the far zone and near zone edge diffraction from the open end of rectangular inlet for  $\phi = 0^\circ$  cut.

FIXED THETA PATTERN: NEAR FIELD CASE  
 EDGE DIFFRACTION FOR RECTANGULAR WAVEGUIDE  
 $(\text{THI}, \text{PHI}) = 30.00 \ 0.00$   
 $(\text{IRR}, \text{THRI}) = 4.00 \ 30.00 \quad (\text{A}, \text{B}) = 1.770 \ 1.770$



(a)

FIXED THETA PATTERN: NEAR FIELD CASE  
 EDGE DIFFRACTION FOR RECTANGULAR WAVEGUIDE  
 $(\text{THI}, \text{PHI}) = 30.00 \ 0.00$   
 $(\text{IRR}, \text{THRI}) = 4.00 \ 30.00 \quad (\text{A}, \text{B}) = 2.000 \ 2.000$

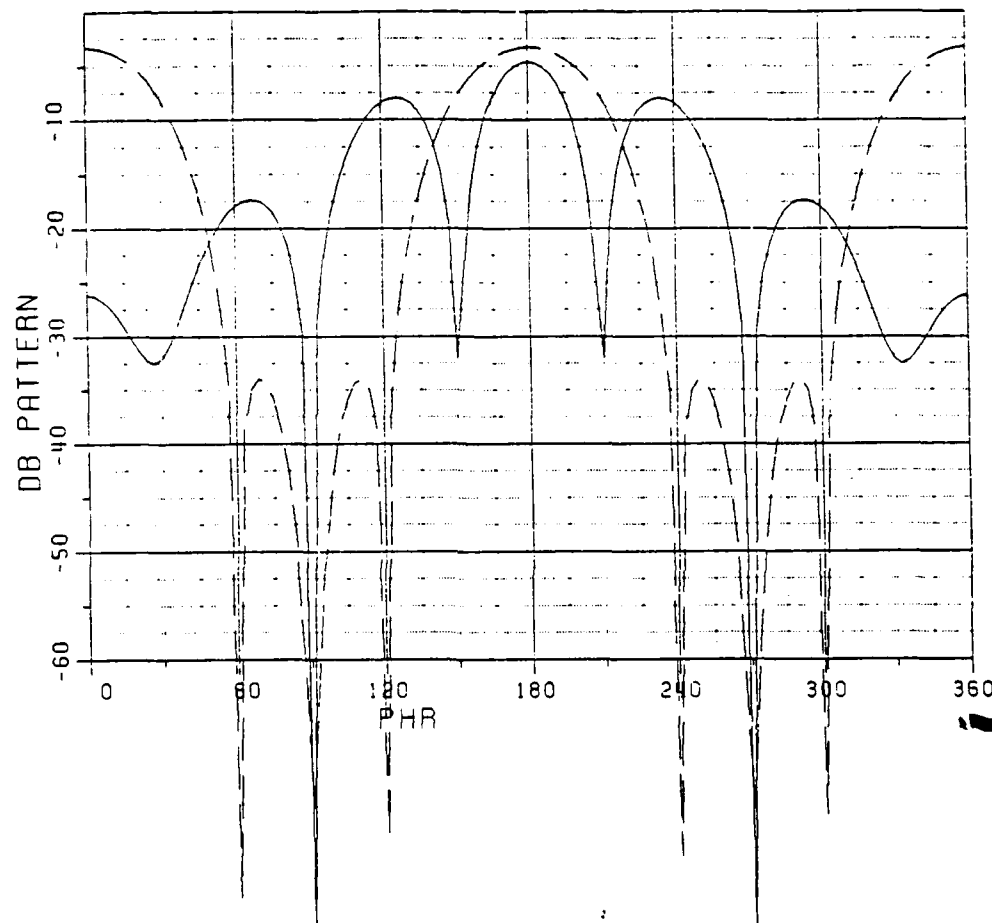


(b)

— total field due to  $E_\theta^i$     - - - total field due to  $E_\phi^i$

Figure 15. The  $30^\circ$  cone scan patterns for rectangular inlet with comparable area or comparable dimension as that of circular inlet in Figure 10.

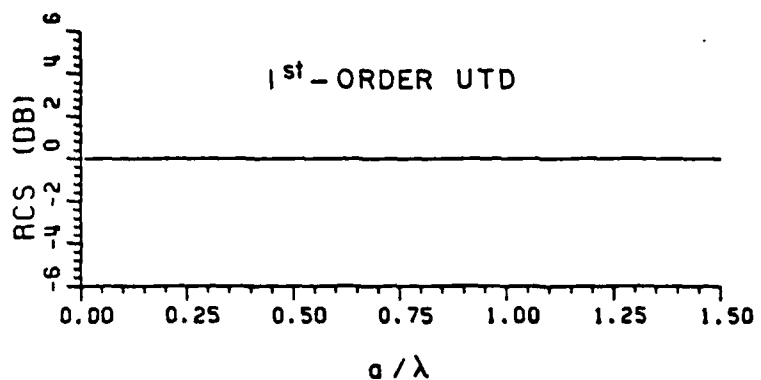
FIXED THETA PATTERN: FAR FIELD CASE  
 EDGE DIFFRACTION FOR RECTANGULAR WAVEGUIDE  
 $(\Theta_1, \Phi_1) = 30.00 \ 0.00$   
 $\Theta_R = 30.00 \quad (a, b) = 2.000 \ 2.000$



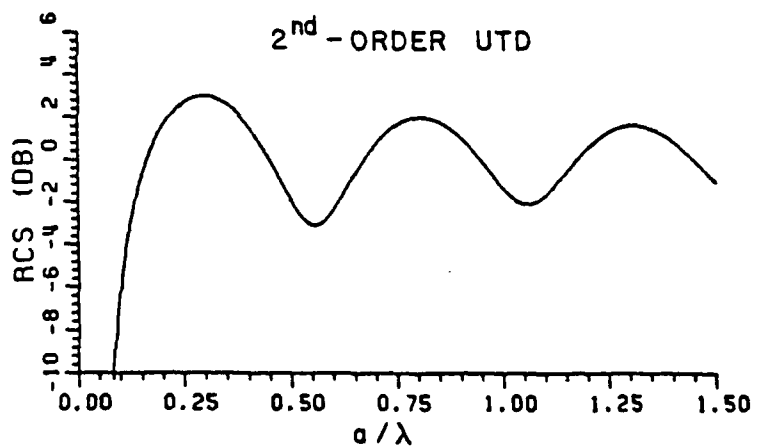
(c)

— total field due to  $E_\theta^i$     - - - total field due to  $E_\phi^i$

Figure 15. (Continued)

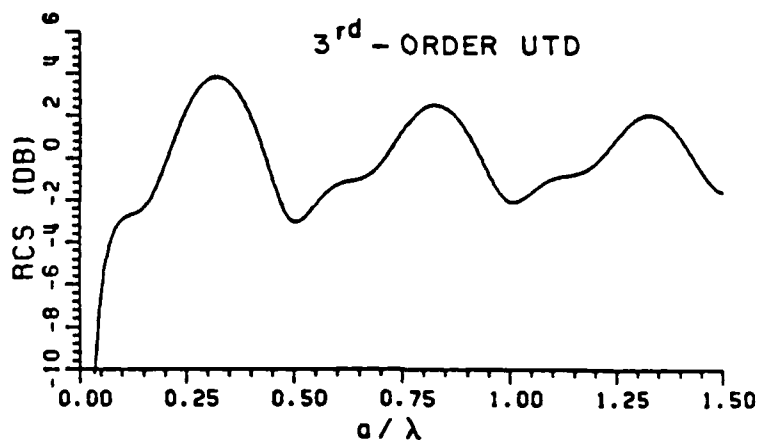


(a) first-order

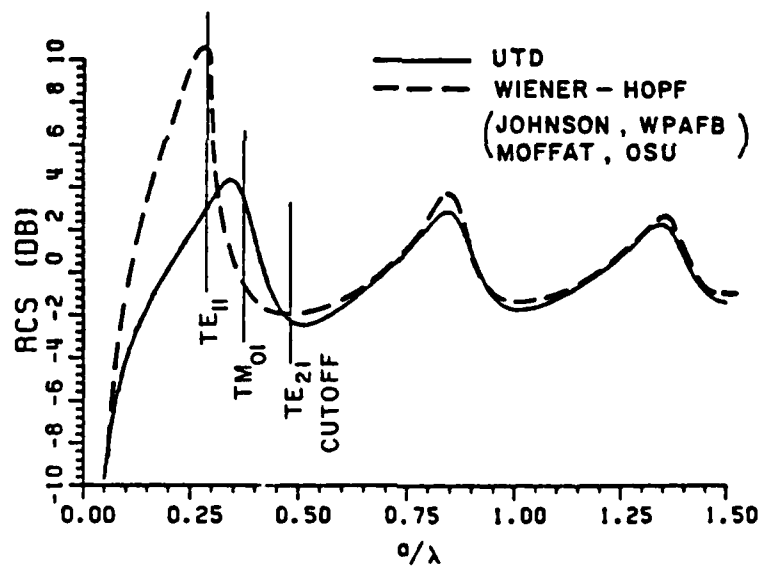


(b) second-order

Figure 16. On-axis backscattered RCS (normalized to  $\pi a^2$ ) from a semi-infinite, hollow, perfectly-conducting circular cylinder with various terms included in UTD calculations.

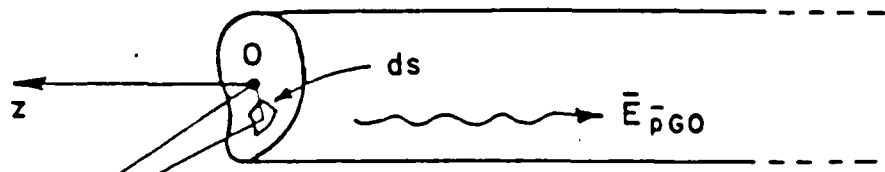


(c) third-order

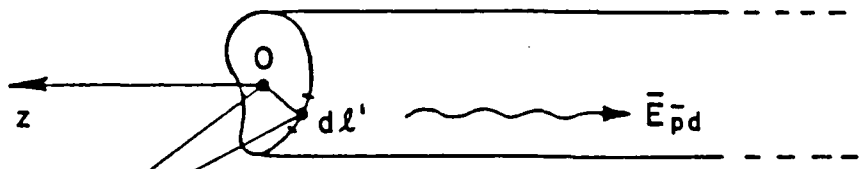


(d) all interaction terms included

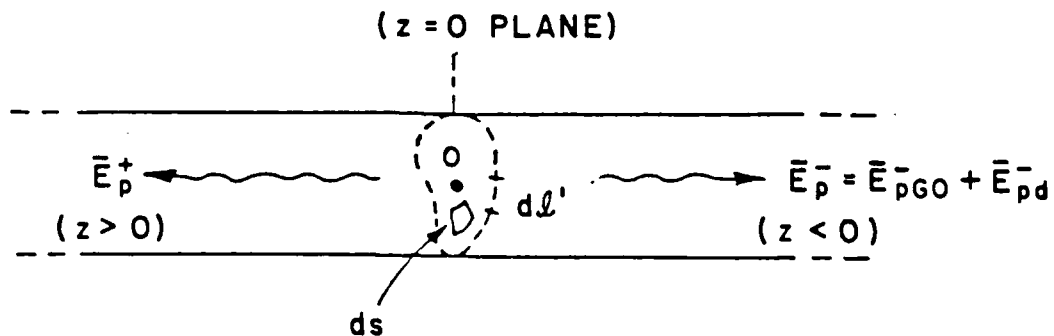
Figure 16. (Continued).



(a) PART OF  $[S_{21}]$  DUE TO COUPLING OF THE  
DIRECT FIELD OF  $d\hat{p}_e$  THROUGH THE APERTURE



(b) PART OF  $[S_{21}]$  DUE TO DIFFRACTION  
CORRECTION FROM THE RIM



(c) EQUIVALENT PROBLEM

Figure 17. Geometry associated with  $[S_{21}]$  calculation.

semi-infinite inlet or waveguide for  $z>0$ ). The equivalent sources at  $z=0$  in Figure 17(c) generate the same fields in the waveguide region  $z<0$  as those which exist in Figures 17(a) and (b) if the equivalent sources are found exactly. Here, the equivalent sources are determined from asymptotic high frequency techniques so that the fields coupled into the waveguide are approximations to the true fields therein. These approximations are high frequency approximations which are expected to work well even down to the lowest propagating mode in the waveguide. According to the high frequency estimates based on the GTD,

$$\bar{J}_s \sim \bar{J}_s^{GO} + \bar{J}_s^d ; \quad (39)$$

and

$$\bar{M}_s \sim \bar{M}_s^{GO} + \bar{M}_s^d \quad (40)$$

where  $\bar{J}_s^{GO}$  and  $\bar{M}_s^{GO}$  represent the unperturbed or geometrical optics (GO) field produced by  $d_{pe}$  within the aperture region (in the  $z=0$  plane) but in the absence of the inlet structure. The additional contributions to  $\bar{J}_s$  and  $\bar{M}_s$  must arise from the diffraction by the edges of the aperture; these edge diffracted field contributions are denoted by  $\bar{J}_s^d$  and  $\bar{M}_s^d$  in (39) and (40). It is easily seen that  $\bar{J}_s^{GO}$  and  $\bar{M}_s^{GO}$  may be expressed as:

$$\bar{J}_s^{GO} = - [\hat{z} \times \bar{H}_{dp_e}^i]_{z=0} ; \quad (41)$$

$$\bar{M}_s^{GO} = - [\bar{E}_{dp_e}^i \times \hat{z}]_{z=0} \quad (42)$$

where  $(\bar{E}_{dp_e}^i; \bar{H}_{dp_e}^i)$  are the (electric; magnetic) fields incident at the open end ( $z=0$ ) from the external source  $dp_e$  at P. These incident fields  $(\bar{E}_{dp_e}^i; \bar{H}_{dp_e}^i)$  represent the unperturbed fields of  $dp_e$  which exist in the absence of the inlet. Clearly [6,15]:

$$\bar{E}_{dp_e}^i \approx \frac{jkZ_0}{4\pi} \hat{s}^i \times \hat{s}^i \times dp_e \frac{e^{-jks^i}}{s^i} \quad (43)$$

and

$$\bar{H}_{dp_e}^i \approx \frac{-jk}{4\pi} \hat{s}^i \times dp_e \frac{e^{-jks^i}}{s^i} \quad (44)$$

The expressions in (43) and (44) are valid for distances  $s^i$  which correspond to  $dp_e$  being in the near zone of the inlet aperture ( $z=0$ ). However,  $s^i$  cannot be made extremely small to where the reactive field terms of the type  $1/(s^i)^2$  and  $1/(s^i)^3$  become significant; these higher order range dependent terms are ignored in (43) and (44) which pertain only to the radiation fields. Before proceeding to calculate the modal transmission coefficients  $\bar{A}_{nm}$ , it is convenient to decompose  $\bar{A}_{nm}$  as follows:

$$\bar{A}_{nm} = A_{nm}^{GO} + A_{nm}^d \quad , \quad (45)$$

where  $A_{nm}^{GO}$  is the part of  $\bar{A}_{nm}$  due to  $\bar{J}_s^{GO}$  and  $\bar{M}_s^{GO}$ ; whereas,  $A_{nm}^d$  is the part of  $\bar{A}_{nm}$  which is produced by  $\bar{J}_s^d$  and  $\bar{M}_s^d$ . It is now an easy matter to find  $A_{nm}^{GO}$  from  $\bar{J}_s^{GO}$  and  $\bar{M}_s^{GO}$  by employing the results of Appendix I which indicate the manner in which electric and magnetic current sources excite modes inside a waveguide [13]. Thus, from (A-8) of

Appendix I, the GO part of the  $TE_{nm}$  transmission (or coupling) coefficients  $A_{nm}$  are given by:

$$A_{nm}^{GO} = \frac{- \int \int ds [(\bar{e}_{nm}^{-1} e^{-j\beta_{nm} z}) \cdot (\bar{J}_s^{GO}) - (\bar{h}_{nm}^{-1} + \hat{z} \bar{h}_{znm}^{-1}) e^{-j\beta_{nm} z} \cdot (\bar{M}_s^{GO})]}{(aperture(z=0))} \cdot \frac{2 \int \int ds \hat{z} \cdot (\bar{e}_{nm}^{-1} \times \bar{h}_{nm}^{-1})}{(aperture(z=0))} . \quad (46)$$

In a similar fashion, one may express the  $TM_{nm}$  transmission (or coupling) coefficients  $B_{nm}^{-}$  by

$$B_{nm}^{-} = B_{nm}^{GO} + B_{nm}^d \quad (47)$$

where  $B_{nm}^{GO}$  is obtained via (A-8) as

$$B_{nm}^{GO} = \frac{- \int \int ds [(\bar{e}_{nm}^{-1} + \hat{z} \bar{e}_{znm}^{-1}) e^{-j\beta_{nm} z} \cdot (\bar{J}_s^{GO}) - (\bar{h}_{nm}^{-1} e^{-j\beta_{nm} z}) \cdot (\bar{M}_s^{GO})]}{(aperture(z=0))} \cdot \frac{2 \int \int ds \hat{z} \cdot (\bar{e}_{nm}^{-1} \times \bar{h}_{nm}^{-1})}{(aperture(z=0))} . \quad (48)$$

It is not easy, in general to calculate  $A_{nm}^d$  and  $B_{nm}^d$  from  $\bar{J}_s^d$  and  $\bar{M}_s^d$  in the aperture ( $z=0$ ); however,  $A_{nm}^d$  and  $B_{nm}^d$  may be calculated indirectly via an approach based on the ECM which employs equivalent magnetic line and line dipole sources on the rim of the aperture ( $z=0$ ). These equivalent sources of strengths  $M_{\ell}^d$  and  $M_{d\ell}^d$  corresponding to the magnetic line and line dipole rim currents radiate "inside the infinite waveguide" (corresponding to the inlet and it's extension for  $z>0$ ) as in Figure 17(c). Since the equivalent rim currents must lie on the "waveguide walls" (see Figure 17) in this case, only the equivalent

magnetic type rim currents are thus required as any equivalent electric type rim currents which are tangential to the waveguide walls would be shorted out because the walls are perfectly-conducting. This situation is in contrast to the exterior radiation or  $[S_{11}]$  calculation via the equivalent electric and magnetic rim currents  $I_{eq}$  and  $M_{eq}$  which radiate in "free space" as shown in Figure 8(b). Also,  $I_{eq}$  and  $M_{eq}$  of (31) and (32) contain Keller's GTD edge diffraction coefficients  $D_s$  and  $D_h$ ; whereas, for reasons which are indicated below, the equivalent rim currents  $M^L$  and  $M^{Ld}$  are defined in terms of the Ufimstev type edge diffraction coefficients  $D_h^U$  and  $D_s^U$ , respectively, as follows\* [6]:

$$M^L = \sum_{j=1}^N M_j^L = \sum_{j=1}^N \left( -Z_0 \sqrt{\frac{8\pi}{jk}} \right) \frac{D_h^U(\psi_j^{nm}, \psi'; \beta_0, \beta_{nmj})}{|\sqrt{\sin\beta_0 \sin\beta_{nmj}}|} \left( \frac{\bar{H}^i \cdot \hat{\ell}'}{2} \right) \quad (49)$$

and

$$M^{Ld} = \sum_{j=1}^N M_j^{Ld} = \sum_{j=1}^N \left( \sqrt{\frac{8\pi}{jk}} \frac{1}{|s_{nm}^{dj} \times \hat{z}|} \right) \cdot \frac{D_s^U(\psi_j^{nm}, \psi'; \beta_0, \beta_{nmj})}{|\sqrt{\sin\beta_0 \sin\beta_{nmj}}|} \left( \frac{\bar{E}^i \cdot \hat{\ell}'}{2} \right) \quad (50)$$

where  $D_s^U$  and  $D_h^U$  are given by [6]:

---

\* The fields  $\bar{H}^i \cdot \hat{\ell}'$  and  $\bar{E}^i \cdot \hat{\ell}'$  are multiplied by a factor of 1/2 in (49) and (50) to account for the presence of the waveguide walls on which  $M^L$  and  $M^{Ld}$  are located: this aspect is discussed in [6].

$$D_{s,h}^U(\psi_j^{nm}, \psi'; \beta_0, \beta_{nmj}) = \frac{-e^{-j\pi/4}}{2\sqrt{2\pi k}} \frac{1}{|\sqrt{\sin\beta_0 \sin\beta_{nmj}}|} \left[ \left( \sec \frac{\psi_j^{nm} - \psi'}{2} - \tan \frac{\psi_j^{nm} - \psi'}{2} \right) \mp \left( \sec \frac{\psi_j^{nm} + \psi'}{2} - \tan \frac{\psi_j^{nm} + \psi'}{2} \right) \right]. \quad (51)$$

It is necessary to use the Ufimstev diffraction coefficients  $D_s^U$  and  $D_h^U$ , respectively, in (49) and (50) instead of the Keller edge diffraction coefficients  $D_s$  and  $D_h$  due to the fact that the truncation of the  $\bar{J}_s^{GO}$  and  $\bar{M}_s^{GO}$  sources by the rim or boundary (end points) of the surface integrals in (46) and (48) over the inlet aperture ( $z=0$ ) gives rise to some contributions to the edge diffracted fields which propagate into the waveguide. Hence, the remaining contributions to the edge diffracted field must come from  $D_{s,h}^U$  according to the PTD ansatz instead of from  $D_{s,h}$  which yields the total first order diffracted field [6]. Clearly, the use of  $D_{s,h}$  instead of  $D_{s,h}^U$  in (51) would erroneously include some diffraction effects twice when the effects of (49) and (50) are combined with (46) and (48). In (49), (50) and (51), the incident ray from  $d\bar{p}_e$  makes an azimuthal angle  $\psi'$  about the unit edge tangent  $\hat{\ell}'$  at any point of diffraction on the rim (see Figures 9(a) and 9(b)). Likewise,  $\psi_j^{nm}$  in (49;50;51) corresponds to an azimuthal angle which the ray diffracted from the edge along the  $\hat{s}_{nm}^{dj}$  direction into the waveguide region makes about  $\hat{\ell}'$  at the same point of diffraction (note:  $\beta_{nmj}$  and  $\psi_j^{nm}$  are like  $\beta$  and  $\psi$  in Figures 9(a) and 9(b); likewise  $\beta_0$  and  $\psi'$

also have the same meaning as in those figures.) It is important to also note that the direction of the ray diffracted into the waveguide must be chosen to correspond to the "modal ray" direction [6]. The circular waveguide modes can be asymptotically approximated in the circular inlet case by a set of axially divergent and convergent conical modal ray systems sufficiently far from the waveguide axis. If one considers the reciprocal problem of the radiation into the exterior region by the modes incident at the open end from within the waveguide region ( $z < 0$ ), then it is only the upgoing or axially divergent (and not axially convergent) conical modal ray system which constitutes the field "incident" on the edge; this incident field diffracts from the rim edge (at  $z=0$ ) to contribute to the exterior field. The  $\psi_j^{nm}$  of (49;50) in the original problem is associated with the  $TE_{nm}$  and  $TM_{nm}$  conical modal rays which are launched via edge diffraction and which exactly correspond to the axially divergent conical modal rays in the reciprocal problem except that these rays are now reversed with respect to those in the reciprocal problem. Alternately phrased,  $\psi_j^{nm}$  of (49;50) in the original problem is associated with the axially convergent conical modal rays which are launched into the waveguide region due to edge diffraction effects contained in  $\bar{J}_s^d$  and  $\bar{M}_s^d$ . Since one deals with only one set of conical modal rays (i.e., of the axially convergent type in this situation) the sums in (49) and (50) reduce to a single term for each  $TE_{nm}$  and  $TM_{nm}$  case, respectively; i.e.,  $N=1$  in (49) and (50) for the circular inlet configuration. On the other hand, the rectangular waveguide modes can be expressed as a set of four modal plane wave or ray

fields everywhere inside the waveguide including the edges at the open end. These rays also contain a pair of rays that propagate toward each of the four edges as well as a pair of rays that propagate away from those edges. In the present  $[S_{21}]$  calculation, it is of interest to associate  $\psi_j^{nm}$ , in the case of the rectangular inlet, to rays launched into the waveguide region ( $z < 0$ ) via edge diffraction of the field incident from  $d\bar{e}_e$  (which lies in the exterior region as in Figure 9). Thus,  $\psi_j^{nm}$  is the azimuthal angle (about  $\hat{z}'$ ) associated with the edge diffracted rays which are identified with a pair of rectangular waveguide modal rays that propagate away from the edges. Clearly, since there exists a pair of such modal rays in this  $[S_{21}]$  calculation for the rectangular inlet, the summing index in (49) and (50) goes from  $j=1$  to  $j=2$ ; i.e.,  $N=2$  in (49) and (50) for the rectangular inlet case. The radiation of  $M^\ell$  and  $M^{\ell d}$  of (49) and (50) into the waveguide region is given as before via (A-8) of Appendix I. Thus, the coefficients  $A_{nm}^d$  and  $B_{nm}^d$  of the  $TE_{nm}$  and  $TM_{nm}$  modes excited by  $M^\ell$  and  $M^{\ell d}$  are explicitly given by

$$A_{nm}^d = \frac{\sum_{j=1}^N \int_{\text{rim}(z=0)} (d\ell' [\bar{h}_{nm} \cdot M_j^\ell \hat{e}' + \hat{z} h_{znm} \cdot M_j^{\ell d} \hat{z}] e^{-j\beta_{nm}^j z})}{2 \iint_{\text{aperture } (z=0)} ds \hat{z} \cdot (\bar{e}_{nm} \times \bar{h}_{nm})} \quad (52)$$

and,

$$B_{nm}^d = \frac{\sum_{j=1}^N \int_{\text{rim}(z=0)} (d\ell' [\bar{h}_{nm} \cdot M_j^\ell \hat{e}'] e^{-j\beta_{nm}^j z})}{2 \iint_{\text{aperture } (z=0)} ds \hat{z} \cdot (\bar{e}_{nm} \times \bar{h}_{nm})} \quad (53)$$

### C. Near Zone Coupling Matrix $[\tilde{S}_{21}]$

The scattering matrix  $[S_{21}]$  can easily be identified via (14), (15), (45), (46), (47), (48), (52) and (53). It is noted that  $\bar{M}_s^{GO}$ ,  $\bar{J}_s^{GO}$ ,  $M_j^l$  and  $M_j^{ld}$  contain information on  $A_\theta$  and  $A_\phi$  via  $\bar{E}^i$  and  $\bar{H}^i$  that are present in these quantities (also see (1) and (2)). Recall, of course, that the present development can also deal with a near source  $d\bar{p}_e$  type illumination as indicated in (43) and (44) in which case the coupling matrix  $[S_{21}]$  must be replaced by  $[\tilde{S}_{21}]$  which is defined via the relationship

$$\begin{bmatrix} [A_{nm}^-] \\ [B_{nm}^-] \end{bmatrix} = \begin{bmatrix} [S'_{xnm}] & [S'_{ynm}] & [S'_{znm}] \\ [S'_{xnm}] & [S'_{ynm}] & [S'_{znm}] \end{bmatrix} \begin{bmatrix} d\bar{p}_{ex} \\ d\bar{p}_{ey} \\ d\bar{p}_{ez} \end{bmatrix} \quad (54)$$

where

$$[\tilde{S}_{21}] = \begin{bmatrix} [S'_{xnm}] & [S'_{ynm}] & [S'_{znm}] \\ [S'_{xnm}] & [S'_{ynm}] & [S'_{znm}] \end{bmatrix} \quad (55)$$

and

$$\begin{bmatrix} d\bar{p}_{ex} \\ d\bar{p}_{ey} \\ d\bar{p}_{ez} \end{bmatrix} = \begin{bmatrix} \hat{x} \cdot d\bar{p}_e \\ \hat{y} \cdot d\bar{p}_e \\ \hat{z} \cdot d\bar{p}_e \end{bmatrix} \quad .$$

If the source  $d\bar{p}_e$  recedes to infinity, then  $\bar{E}_{d\bar{p}_e}^i \rightarrow \bar{E}^i$  corresponding to a

locally plane wave type of illumination. Also,  $[\tilde{S}_{21}] [dp_e]$  on the right side of (54) should approach  $[S_{21}] [E^i]$  which occurred on the right side of (14) when  $dp_e$  recedes to infinity. Clearly then,

$$\begin{bmatrix} [A_{nm}] \\ [B_{nm}] \end{bmatrix} = [\tilde{S}_{21}] \begin{bmatrix} dp_{ex} \\ dp_{ey} \\ dp_{ez} \end{bmatrix} \rightarrow [S_{21}] \begin{bmatrix} A_\theta \\ A_\phi \end{bmatrix}, \text{ if } dp_e \text{ recedes to infinity} \quad (56)$$

Some numerical results for  $[\tilde{S}_{21}]$  will be indicated in terms of  $[S_{12}]$  since  $[S_{12}]$  is obtained from  $[\tilde{S}_{21}]$  via reciprocity.

#### D. Development of $[S_{12}]$ Using Reciprocity

The scattering matrix  $[S_{12}]$  describes the manner in which the modal fields propagating within the waveguide region ( $z < 0$ ) radiate into the exterior region from the open front end (at  $z = 0$ ) as in Figure 5. The observation point can be in the near zone of the inlet aperture as mentioned previously. This matrix  $[S_{12}]$  was defined earlier in (10) and (12). Actually the problem of determining  $E_{x,y,z}^{r0}$  of (10) in the near zone of the inlet aperture can be seen to be related to the problem of determining  $A_{nm}$  and  $B_{nm}$  due to the source  $dp_e$  at the point P in the near zone as in Figure 17 via the reciprocity theorem for electromagnetic fields. Thus,  $[S_{12}]$  of (12) may be found from  $[\tilde{S}_{21}]$  of (55) via the reciprocity principle as illustrated below.

Let an electric current moment  $dp_e$  at P in the near zone of the inlet aperture generate the fields  $(\bar{E}^e; \bar{H}^e)$  everywhere<sup>†</sup> in the presence

of the inlet structure which is assumed to be a semi-infinite hollow waveguide as shown in Figure 18. Also let a source-free waveguide modal field  $\bar{E}_p^+$  propagate from the region  $z < 0$  to the inlet opening at  $z = 0$ , and let this mode generate the total fields  $(\bar{E}^{ro}; \bar{H}^{ro})$  after it scatters from the open end. Furthermore, let  $(\bar{E}^e; \bar{H}^e)$  exist everywhere<sup>†</sup> with  $d\bar{p}_e$  absent. Now, an application of the reciprocity theorem to the pair of fields  $(\bar{E}^e; \bar{H}^e)$  and  $(\bar{E}^{ro}; \bar{H}^{ro})$  within the region  $V$  bounded by the surfaces  $S$ ,  $S_0$  and the surface  $\Sigma$  at infinity (see Figure 18) yields:

$$\iint_{S+S_0+\Sigma} [\bar{E}^{ro} \times \bar{H}^e - \bar{E}^e \times \bar{H}^{ro}] \cdot \hat{n} \, ds = d\bar{p}_e \cdot \bar{E}^{ro}(p) . \quad (57)$$

Next, employing the boundary conditions  $[\hat{n} \times \bar{E}^{ro}]_S = 0$ ,  $[\hat{n} \times \bar{E}^e]_S = 0$  on the surface which encapsulates the waveguide walls, and also enforcing the radiation conditions on  $(\bar{E}^{ro}; \bar{H}^{ro})$  and  $(\bar{E}^e; \bar{H}^e)$  over the surface  $\Sigma$  at infinity in (57) leads to

$$- \iint_{S_0} \bar{H}^e \cdot \bar{M}_S^{eq} \, ds + \iint_{S_0} \bar{E}^e \cdot \bar{J}_S^{eq} \, ds = d\bar{p}_e \cdot \bar{E}^{ro}(p) , \quad (58)$$

where  $\bar{M}_S^{eq}$  and  $\bar{J}_S^{eq}$  constitute the field quantities associated with  $\bar{E}^{ro}$  and  $\bar{H}^{ro}$  inside the waveguide. In particular

---

<sup>†</sup>Here, "everywhere" includes the regions which are both interior and exterior to the inlet.

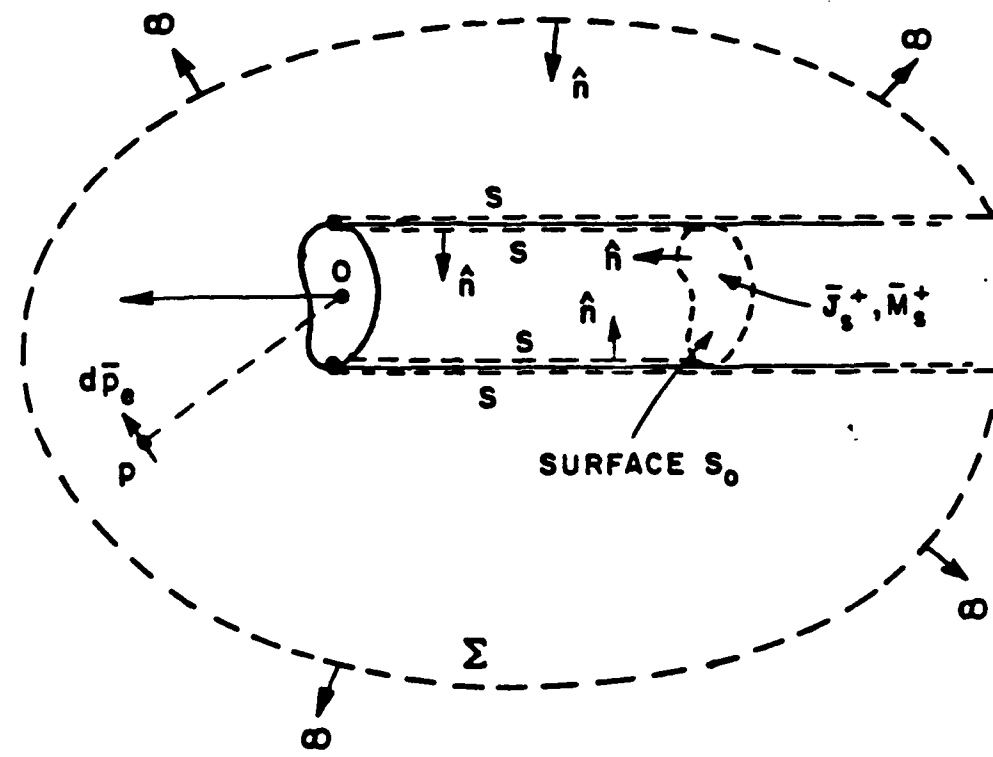


Figure 18(a). Geometry for an application of the reciprocity theorem which relates  $[S_{12}]$  and  $[S_{21}]$ .

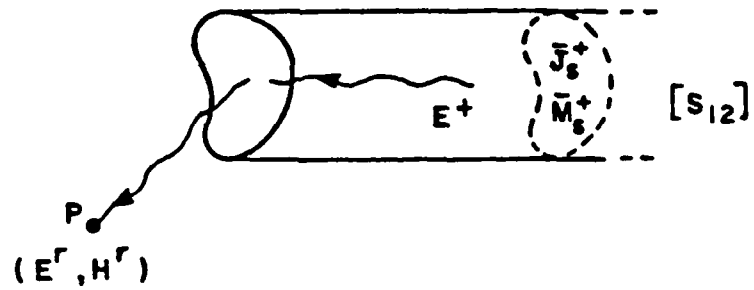


Figure 18(b). Radiation or  $[S_{12}]$  problem.

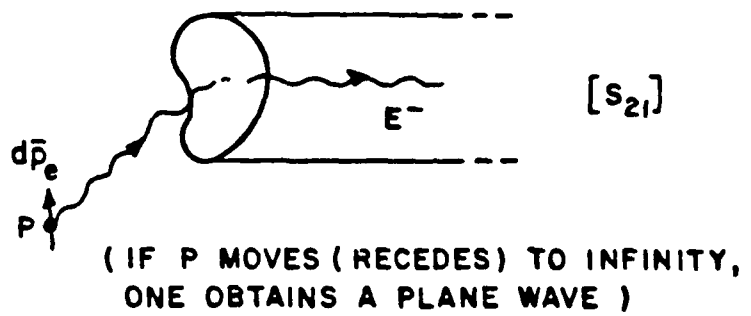


Figure 18(c). Coupling or  $[S_{21}]$  problem.

$$\left. \bar{M}_s^{\text{eq}} \right|_{S_0} \equiv [\bar{E}^{\text{ro}} \times \hat{n}]_{S_0} ; \quad (59)$$

$$\left. \bar{J}_s^{\text{eq}} \right|_{S_0} \equiv [\hat{n} \times \bar{H}^{\text{ro}}]_{S_0} . \quad (60)$$

Furthermore,

$$\left. \bar{E}^{\text{ro}} \right|_{S_0} = (\bar{E}_p^+ + \sum_q R_{pq} \bar{E}_q^-) A_p^+ , \quad (61)$$

and,

$$\left. \bar{H}^{\text{ro}} \right|_{S_0} = (\bar{H}_p^+ + \sum_q R_{pq} \bar{H}_q^-) A_p^+ . \quad (62)$$

The fields  $(\bar{E}_p^+; \bar{H}_p^+)$  are as defined in (A-2) of Appendix I. Here  $(\bar{E}_p^+; \bar{H}_p^+)$  is the  $p^{\text{th}}$  mode incident at the open end of the waveguide as in Figure 5. The single subscript  $p$  refers to a double mode index  $n, m$  as mentioned in Appendix I; likewise, the subscript  $q$  refers to another pair of modal indices  $i, j$ , for example, where  $i$  and  $j$  can be different from  $n$  and  $m$ . The incident modal fields  $(\bar{E}_p^+; \bar{H}_p^+)$  generate the reflected fields  $(\sum_q R_{qp} \bar{E}_q^-; \sum_q R_{qp} \bar{H}_q^-)$  after scattering at the open end, and  $R_{qp}$  denotes the reflection coefficient or the amplitude of the  $q^{\text{th}}$  modal field which is reflected back into the waveguide after a  $p^{\text{th}}$

mode is incident at the open end. One can also write  $\bar{E}^e|_{S_0}$  and  $\bar{H}^e|_{S_0}$  as follows:

$$\bar{E}^e|_{S_0} = \sum_{\ell} A_{\ell}^- \bar{E}_{\ell}^- ; \quad (63)$$

$$\bar{H}^e|_{S_0} = \sum_{\ell} A_{\ell}^- \bar{H}_{\ell}^- , \quad (64)$$

where the subscript  $\ell$  once again refers to a double mode index  $rs$ , for example, as in Appendix I. Incorporating (59)-(64) into (58), and making use of the orthogonality property of the waveguide modes gives:

$$d\bar{p}_e \cdot \bar{E}^{ro}(p) = -2A_p^+ A_p^- \iint_{S_0} \bar{E}_{pt} \times \bar{H}_{pt} \cdot \hat{z} ds . \quad (65)$$

In matrix notation, it is clear that (65) can be expressed as:

$$\begin{bmatrix} \bar{E}_x^{ro}(p) & \bar{E}_y^{ro}(p) & \bar{E}_z^{ro}(p) \end{bmatrix} \begin{bmatrix} d\bar{p}_{ex} \\ d\bar{p}_{ey} \\ d\bar{p}_{ez} \end{bmatrix} = ([A_p^+])^T (-2 \iint_{S_0} \bar{E}_{pt} \times \bar{H}_{pt} \cdot \hat{z} ds) ([A_p^-]). \quad (66)$$

It is noted that  $\bar{E}^{ro}$  contains  $A_p^+$  since  $\bar{E}^{ro}(p)$  is produced by the radiation of  $A_p^+ \bar{E}_p^+$ . Furthermore, it is obvious that (10) and (54) can be expressed more compactly as:

$$\begin{bmatrix} E_x^{ro}(p) \\ E_y^{ro}(p) \\ E_z^{ro}(p) \end{bmatrix} = [S_{12}] \begin{bmatrix} A_p^+ \\ \vdots \end{bmatrix}, \quad (67)$$

and

$$\begin{bmatrix} A_p^- \\ \vdots \end{bmatrix} = [\tilde{S}_{21}] \begin{bmatrix} dp_{ex} \\ dp_{ey} \\ dp_{ez} \end{bmatrix}, \quad (68)$$

where

$$\begin{bmatrix} A_p^\pm \\ \vdots \end{bmatrix} \equiv \begin{bmatrix} A_{nm}^\pm \\ \vdots \\ B_{nm}^\pm \end{bmatrix}. \quad (69)$$

Incorporating (67) and (68) into (66) yields:

$$\begin{bmatrix} A_p^+ \\ \vdots \end{bmatrix}^T [S_{12}]^T \begin{bmatrix} dp_{ex} \\ dp_{ey} \\ dp_{ez} \end{bmatrix} = \begin{bmatrix} A_p^+ \\ \vdots \end{bmatrix}^T (-2 \iint_{S_0} \bar{E}_{pt} \times \bar{H}_{pt} \cdot \hat{z} dS) [\tilde{S}_{21}] \begin{bmatrix} dp_{ex} \\ dp_{ey} \\ dp_{ez} \end{bmatrix}. \quad (70)$$

The relationship between  $[S_{12}]$  and  $[\tilde{S}_{21}]$  now becomes evident from (70); namely:

$$[S_{12}]^T = \left( -2 \iint_{S_0} \bar{E}_{pt} \times \bar{H}_{pt} \cdot \hat{z} ds \right) [\tilde{S}_{21}] \quad . \quad (71)$$

Therefore, one can find  $[S_{12}]$  from a knowledge of  $[\tilde{S}_{21}]$ ;  $[\tilde{S}_{21}]$  was obtained previously in part B of this section.

Typical near zone radiation patterns of open-ended rectangular and circular waveguides which are calculated by the above procedure are indicated in Figures 19 to 33. If the near zone field point is allowed to recede to the far zone then the above procedure also furnishes the far zone radiation patterns. Indeed, the latter are shown in Figures 19 to 23 for the open ended circular waveguide problem; these principal plane far zone radiation pattern calculations are compared with those obtained via the rigorous Wiener-Hopf method [16] in Figures 19 to 23; the comparison is seen to be quite good in these figures. It is noted that while the Wiener-Hopf method provides a useful check on our solutions, the present procedure is far simpler than that based on the Wiener-Hopf method. There is presently no corresponding rigorous analytical solution available in the literature for the far zone radiation pattern of an open-ended rectangular waveguide as there is for the circular waveguide case; hence, the rectangular waveguide far zone radiation patterns are shown without any comparisons. Explicit expressions for the far zone radiation patterns for the circular and rectangular inlets are presented for convenience in Appendix III.

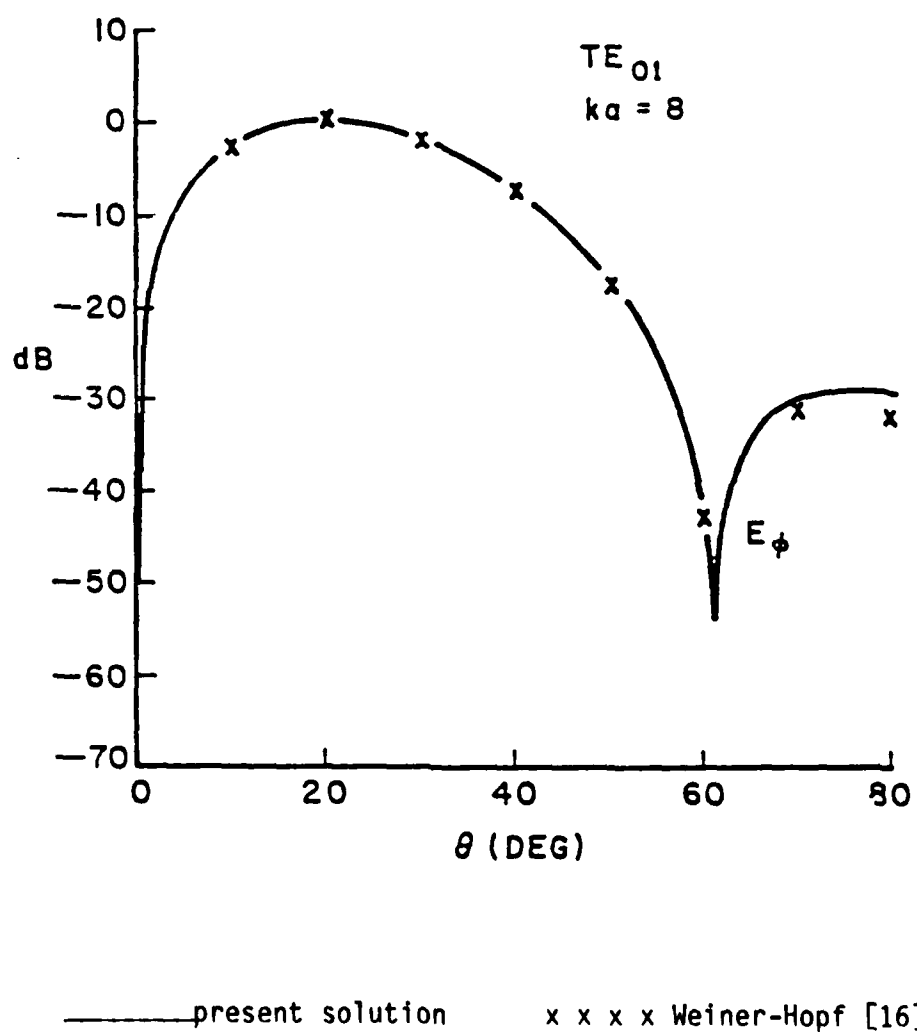


Figure 19.  $E_\phi$  radiation pattern due to a TE<sub>01</sub> mode in an open-ended circular waveguide.

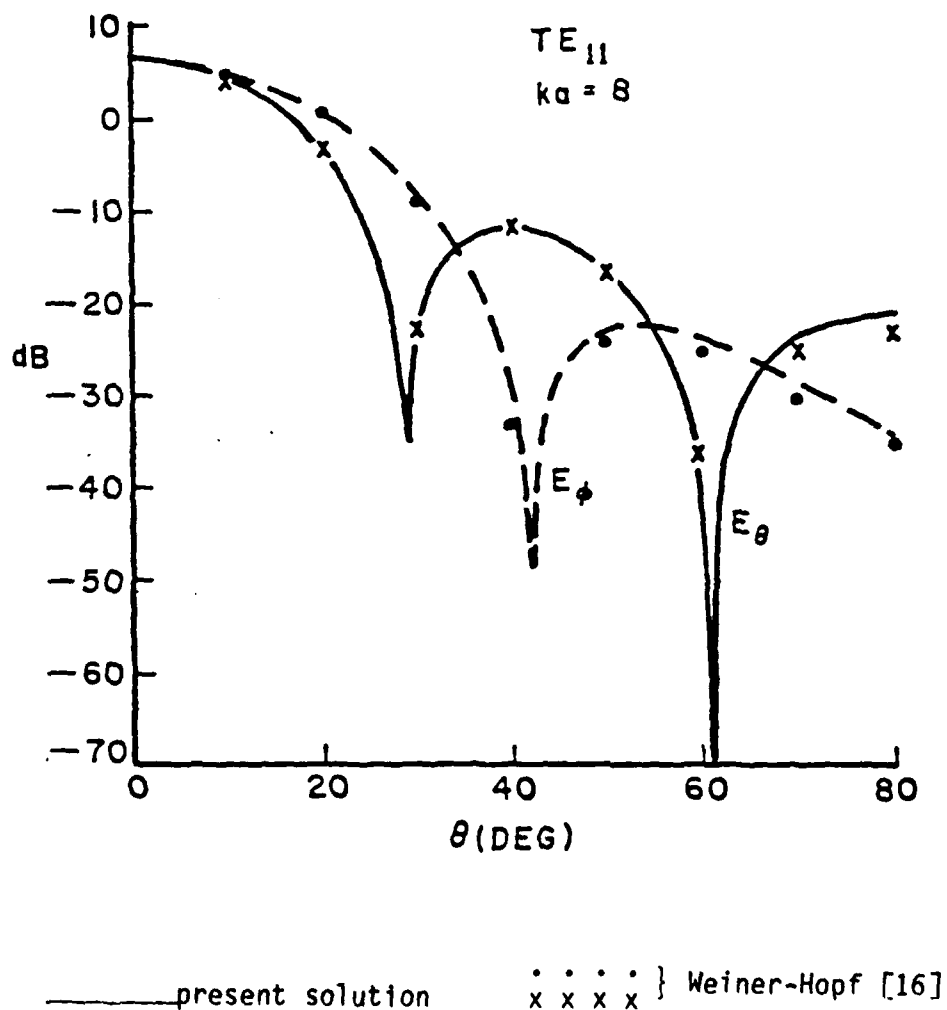


Figure 20.  $E_\theta$  and  $E_\phi$  radiation patterns due to a TE<sub>11</sub> mode in an open-ended circular waveguide.

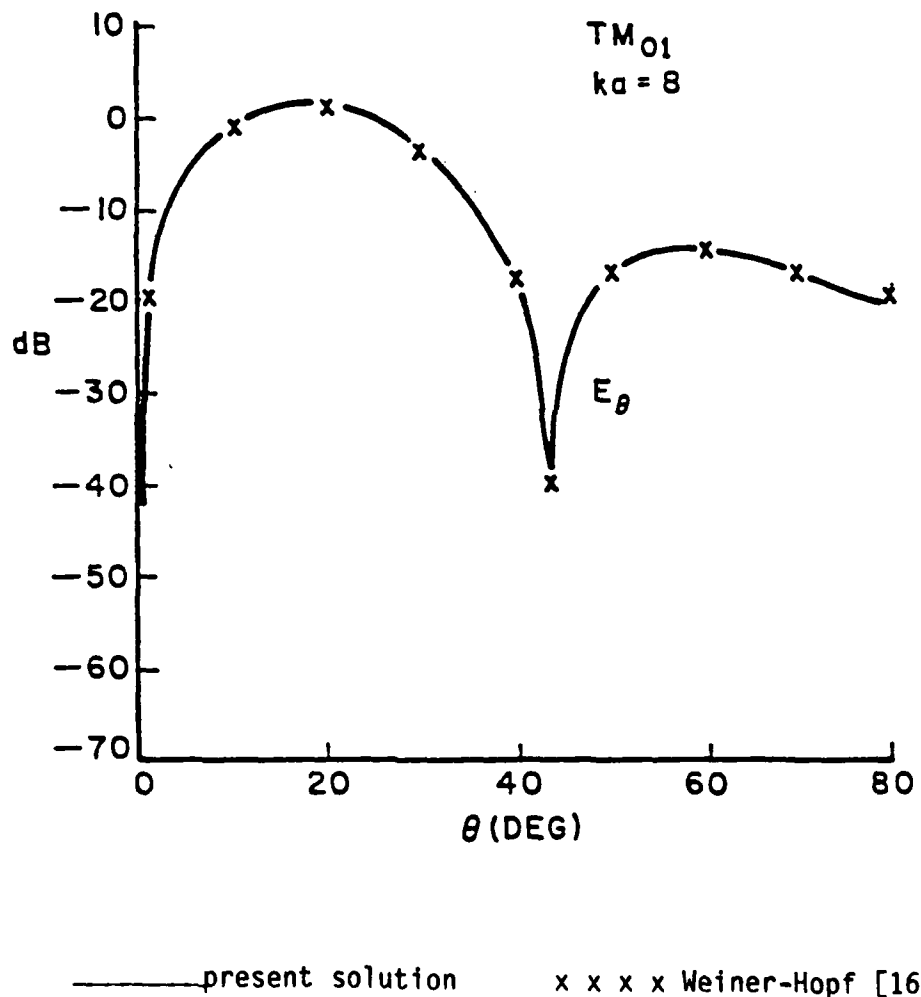
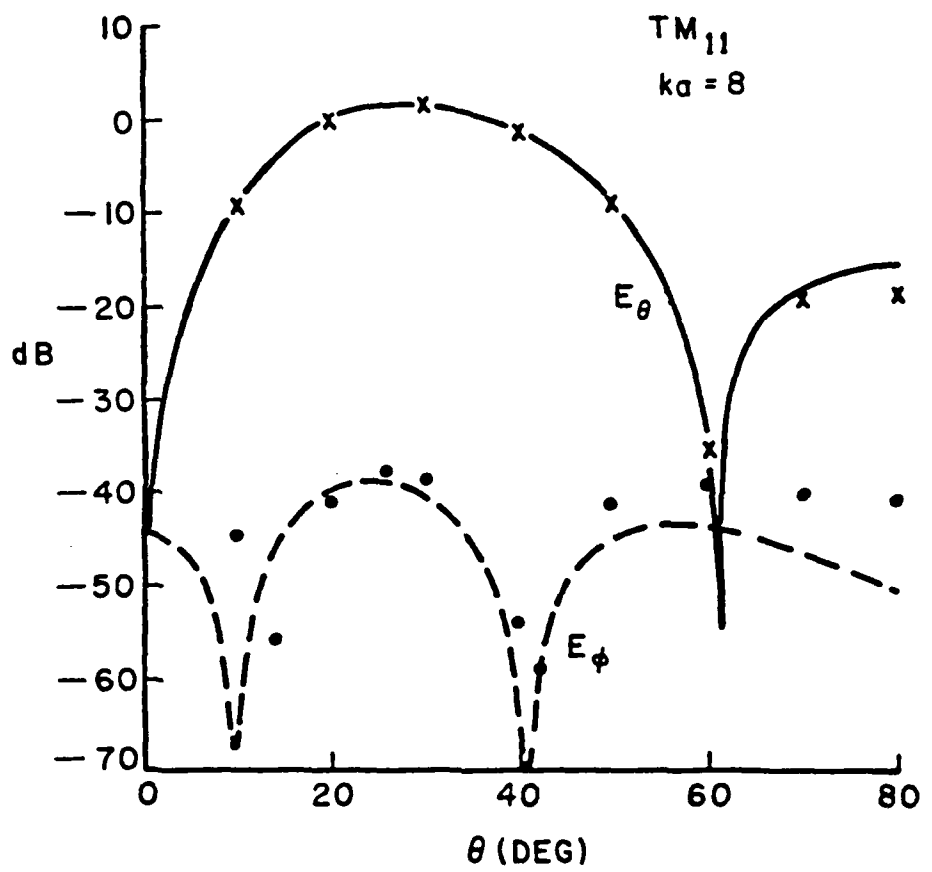


Figure 21.  $E_\theta$  radiation pattern due to a  $TM_{01}$  mode in an open-ended circular waveguide.



— present solution      x x x x } Weiner-Hopf [16]

Figure 22.  $E_\theta$  and  $E_\phi$  radiation patterns due to a  $TM_{11}$  mode in an open-ended circular waveguide.

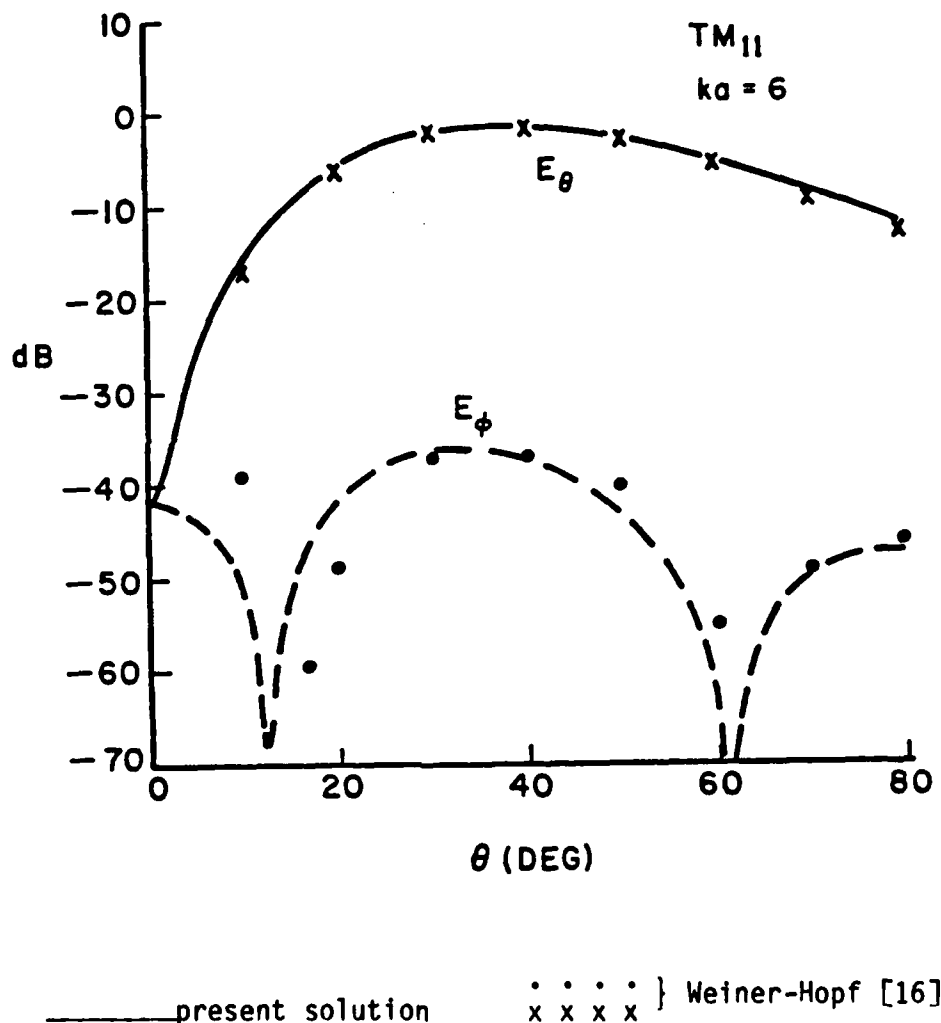
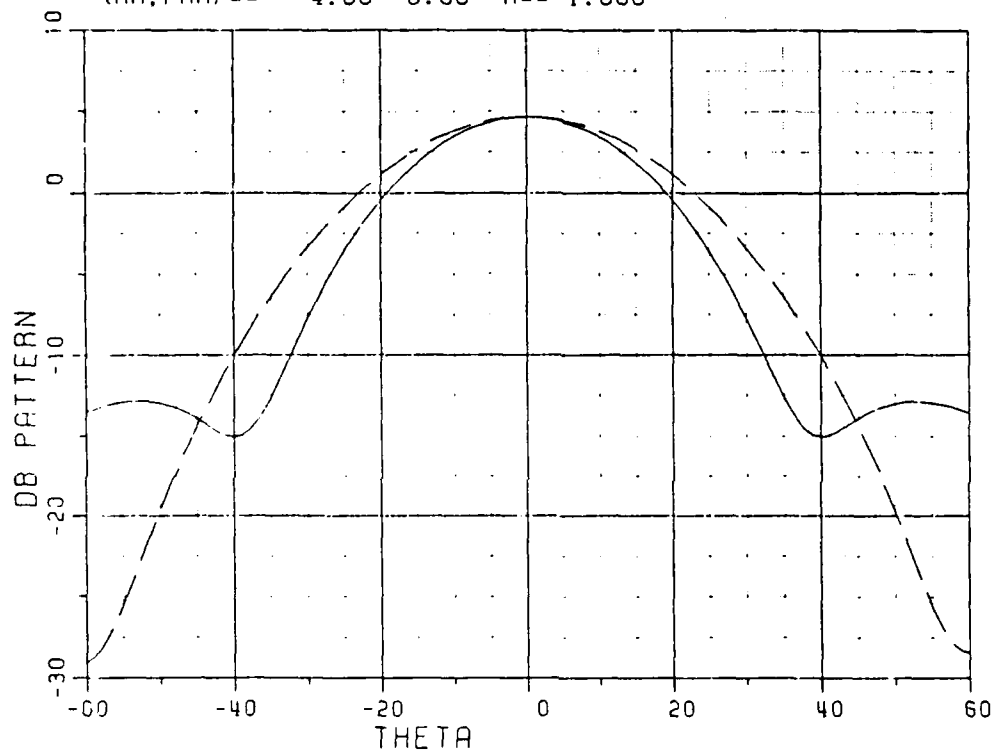


Figure 23.  $E_\theta$  and  $E_\phi$  radiation patterns due to a TM<sub>11</sub> mode in an open-ended circular waveguide.

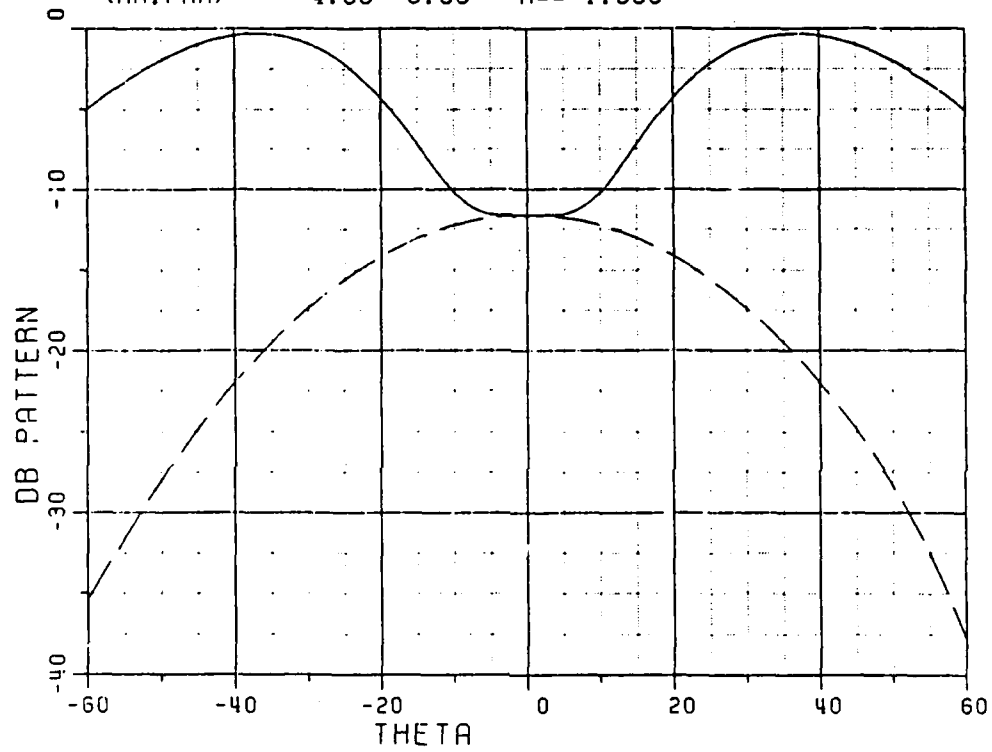
FIXED PHR PATTERN: NEAR FIELD CASE  
RADIATION PATTERN FOR CIRCULAR WAVEGUIDE  
(TE<sub>11</sub> MODE)  
(RR, PHR) == 4.00 0.00 A == 1.000



— corresponding to  $E_\theta$  far zone patterns  
- - - - - corresponding to  $E_\phi$  far zone patterns

Figure 24. The near zone radiation patterns of TE<sub>11</sub> modes.

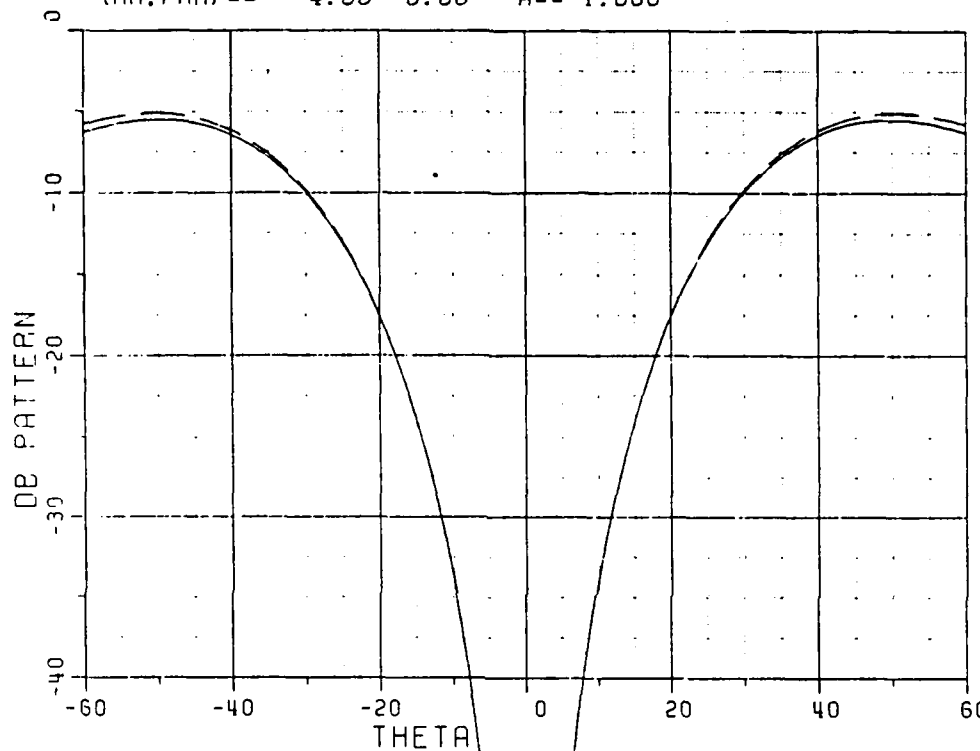
FIXED PHR PATTERN: NEAR FIELD CASE  
 RADIATION PATTERN FOR CIRCULAR WAVEGUIDE  
 (TM<sub>11</sub> MODE)  
 (RR, PHR) == 4.00 0.00 A == 1.000



— corresponding to  $E_\theta$  far zone patterns  
 - - - - - corresponding to  $E_\phi$  far zone patterns

Figure 25. The near zone radiation patterns of TM<sub>11</sub> modes.

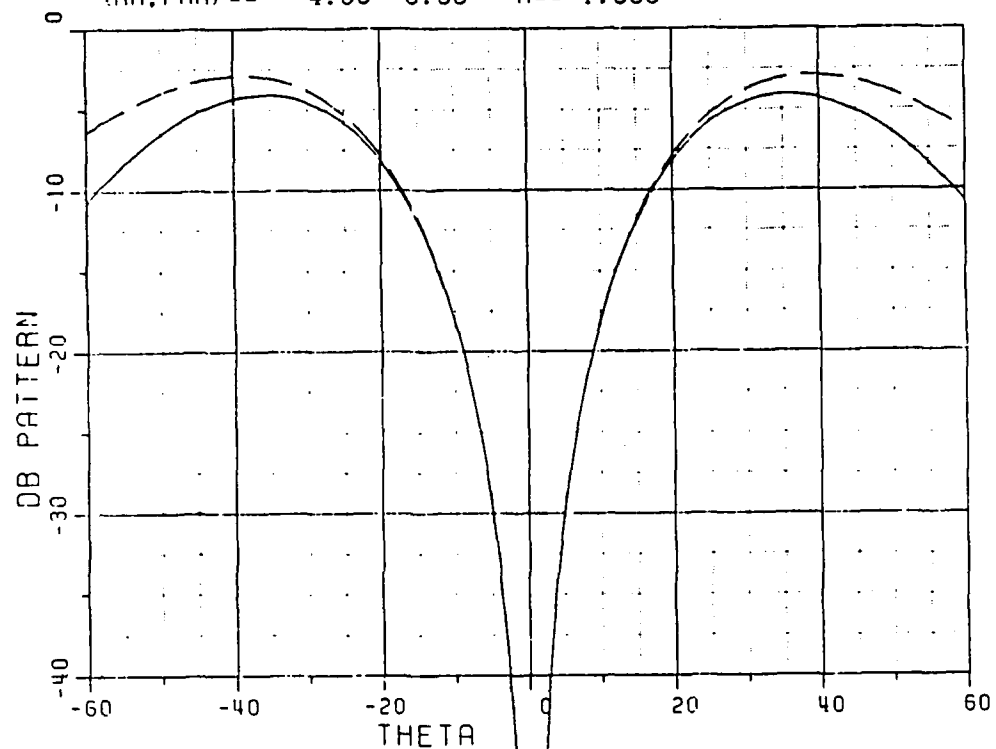
FIXED PHR PATTERN: NEAR FIELD CASE  
RADIATION PATTERN FOR CIRCULAR WAVEGUIDE  
TE41 MODE  
(RR.PHR) == 4.00 0.00 A== 1.000



— corresponding to  $E_\theta$  far zone patterns  
- - - - -  $E_\phi$

Figure 26. The near zone radiation patterns of TE41 modes.

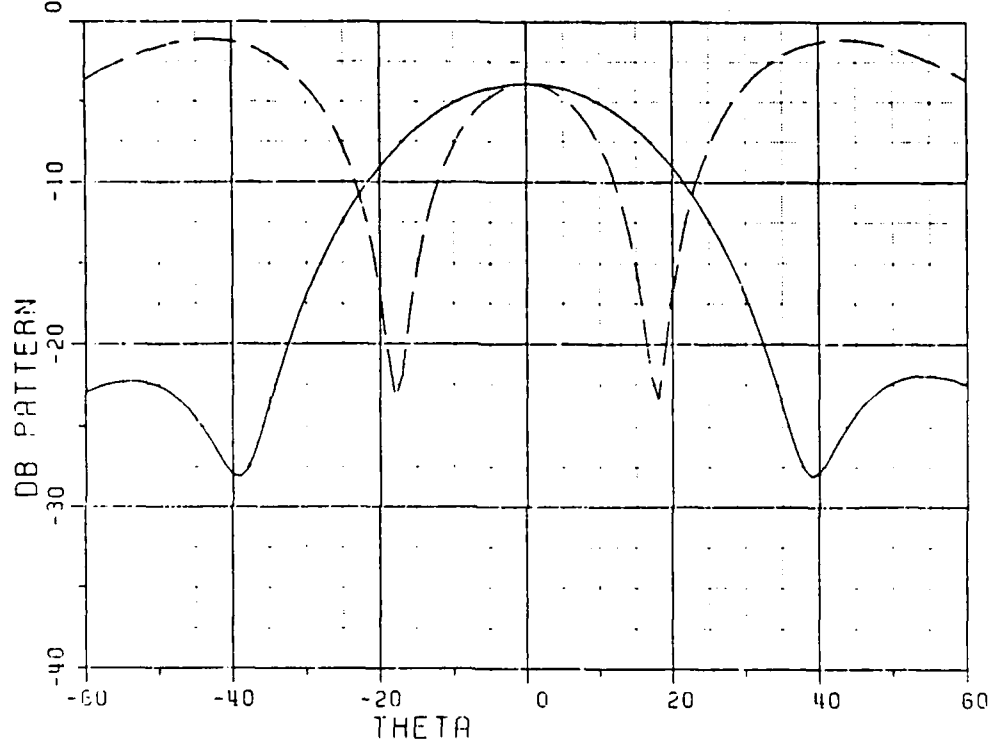
FIXED PHR PATTERN: NEAR FIELD CASE  
RADIATION PATTERN FOR CIRCULAR WAVEGUIDE  
TE31 MODE  
(RR,PHR) == 4.00 0.00 A== 1.000



— corresponding to  $E_\theta$  far zone patterns  
- - - - - corresponding to  $E_\phi$  far zone patterns

Figure 27. The near zone radiation patterns of TE<sub>31</sub> modes.

FIXED PHR PATTERN; NEAR FIELD CASE  
RADIATION PATTERN FOR CIRCULAR WAVEGUIDE  
TE12 MODE  
(RR,PHR) == 4.00 0.00 A== 1.000



— corresponding to  $E_\theta$  far zone patterns  
- - - - - corresponding to  $E_\phi$

Figure 28. The near zone radiation patterns of TE<sub>12</sub> modes.

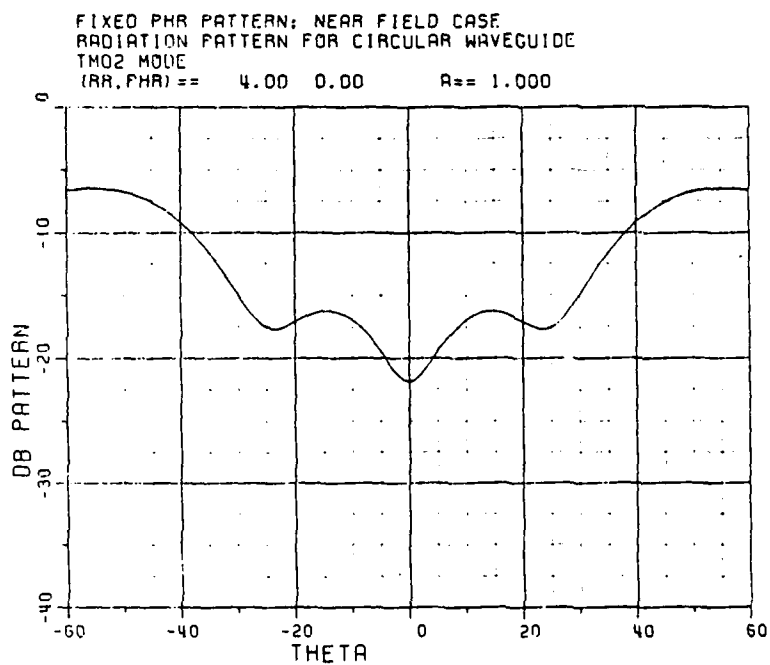


Figure 29. The near zone radiation pattern of TM<sub>02</sub> mode.

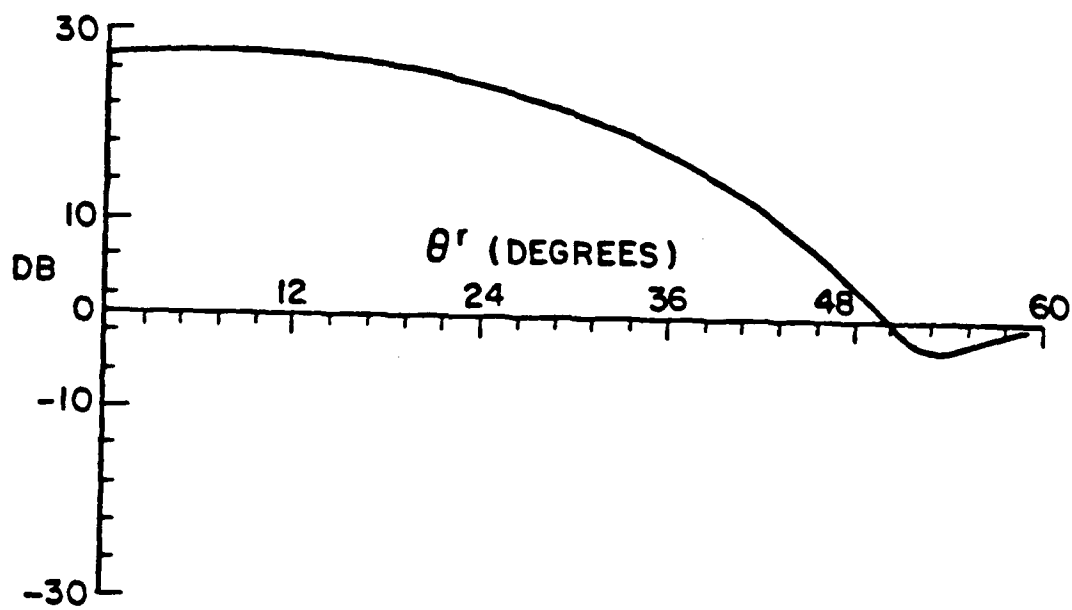


Figure 30. Near zone radiation pattern of an open-ended rectangular waveguide.  $ka=12.58$ ,  $a=2b$ , TE<sub>10</sub> mode,  $\phi^r=0^\circ$ ,  $kR=62.90$ .

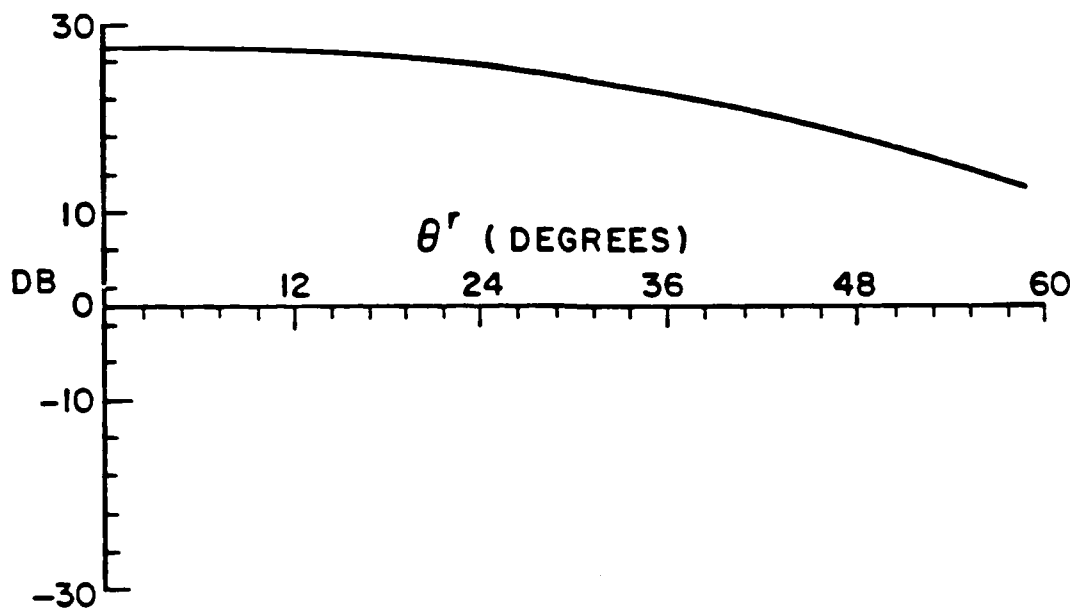


Figure 31. Near zone radiation pattern of an open-ended rectangular waveguide.  $ka=12.58$ ,  $a=2b$ ,  $TE_{10}$  mode,  $\phi^r=90^\circ$ ,  $kR=62.90$ .

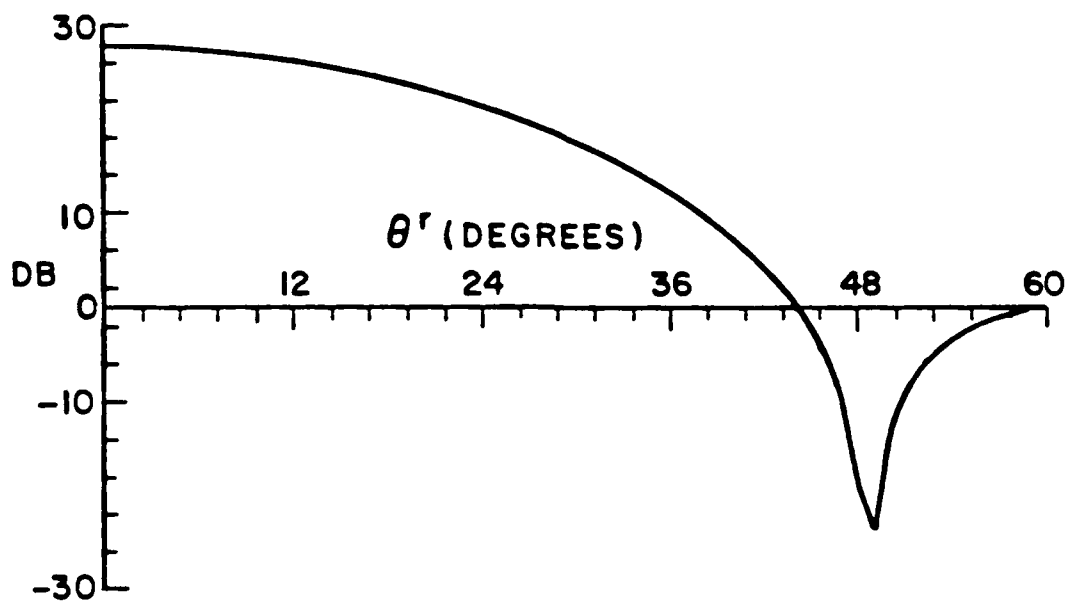


Figure 32. Far zone radiation pattern of an open-ended rectangular waveguide.  $ka=12.58$ ,  $a=2b$ ,  $TE_{10}$  mode,  $\phi^r=0^\circ$ .

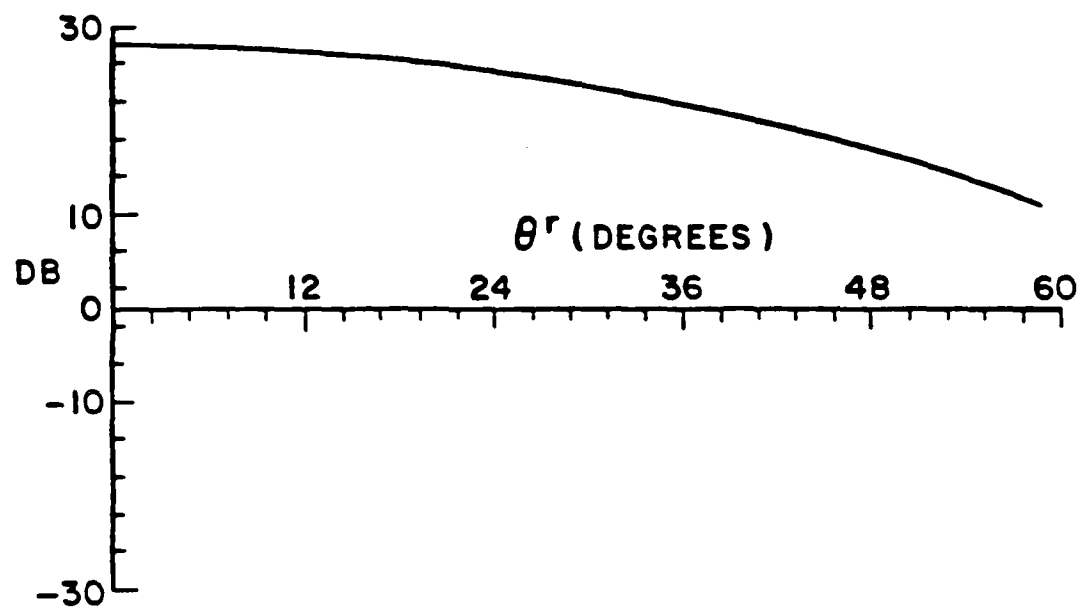
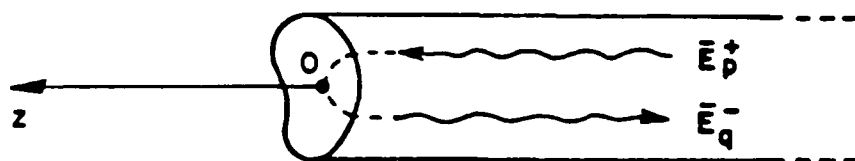


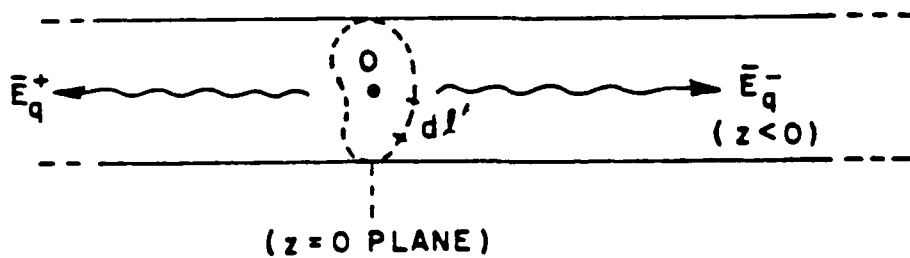
Figure 33. Far zone radiation pattern of an open-ended rectangular waveguide.  $ka=12.58$ ,  $a=2b$ ,  $TE_{10}$  mode,  $\phi^r=90^\circ$ .

### E. Development of $[S_{22}]$

As indicated earlier in Section I,  $[S_{22}]$  represents a modal reflection coefficient matrix which is associated with the interaction illustrated in Figures 5 and 34. In particular,  $[S_{22}]$  is made up of elements which correspond to the modal amplitudes (which are proportional to the reflection coefficients) of the  $TE_{nm}$  and  $TM_{nm}$  modes that are reflected back into the waveguide region ( $z < 0$ ) when either a  $TE_{pq}$  or a  $TM_{pq}$  mode is incident on that open end from the region  $z < 0$ . Once again, GTD and ECM will be employed to calculate these modal reflection coefficients. It was mentioned in part B (of this section) dealing with the development of  $[S_{21}]$  that the modal fields inside a circular or rectangular waveguide could be decomposed into fields which are associated with a set of "modal rays". There exists only one set of rays, namely the axially divergent modal rays, which are "incident" on the circular inlet edge; these incident rays can partly diffract from the edge to propagate back into the waveguide region as a set of axially convergent modal rays to form the reflected modes. On the other hand, there is a pair of such modal rays which are incident on the edge of a rectangular inlet; again, these rays can diffract at the edge to enter back into the waveguide as a pair of rays which exit or leave the edge to form the reflected modes. It is noted that the pair of rays in the rectangular inlet case contain oppositely traveling plane wave components with respect to each edge; consequently these oppositely traveling components flip directions upon undergoing diffraction at the edges to convert the incident pair of modal rays into the reflected pair



(a) GEOMETRY FOR THE REFLECTION COEFFICIENT  
 $[S_{22}]$  MATRIX



(b) EQUIVALENT PROBLEM

Figure 34. Geometry for the reflection coefficient matrix  $[S_{22}]$  calculation.

of modal rays. One may define a set of equivalent magnetic rim currents of strengths  $M_R^{\ell\hat{\ell}'} \hat{\ell}'$  and  $M_R^{\ell d\hat{z}}$  which produce the  $r^{\text{th}}$  modal reflected fields  $(\bar{E}_r^-; \bar{H}_r^-)$  when a set of  $s^{\text{th}}$  modal fields  $(\bar{E}_s^+; \bar{H}_s^+)$  is incident at the open end of the inlet. The fields entering back into the waveguide as reflected modes are produced entirely via edge diffracton of  $(\bar{E}_s^+; \bar{H}_s^+)$  as the ray picture reveals; hence, the equivalent magnetic line and line dipole rim currents  $M_R^{\ell}$  and  $M_R^{\ell d}$  can be expressed as in (49) and (50) but with the Ufimstev edge diffraction coefficients in those equations replaced by the complete (Keller type) edge diffraction coefficients  $D_h$  and  $D_s$ , respectively, as follows:

$$M_R^{\ell} = \sum_{j=1}^N M_{Rj}^{\ell} = \sum_{j=1}^N \left( -z_0 \sqrt{\frac{8\pi}{jk}} \right) \frac{D_h(\psi_j^r, \psi_j^s; \beta_{sj}, \beta_{rj})}{|\sqrt{\sin \beta_{sj} \sin \beta_{rj}}|} \frac{(\bar{H}_s^+ \cdot \hat{\ell}')}{2} \quad (72)$$

and

$$M_R^{\ell d} = \sum_{j=1}^N M_{Rj}^{\ell d} = \sum_{j=1}^N \left( \sqrt{\frac{8\pi}{jk}} \frac{1}{|\hat{s}_r^d \times \hat{z}|} \right) \frac{D_s(\psi_j^r, \psi_j^s; \beta_{sj}, \beta_{rj})}{|\sqrt{\sin \beta_{sj} \sin \beta_{rj}}|} \frac{(\bar{E}_s^+ \cdot \hat{\ell}')}{2} \quad (73)$$

where  $D_{s,h}$  in the above equations are given (as in (34)) by:

$$D_s^h(\psi_j^r, \psi_j^s; \beta_{sj}, \beta_{rj}) = \frac{-e^{-j\pi/4}}{2\sqrt{2\pi k}} \frac{1}{|\sqrt{\sin \beta_{sj} \sin \beta_{rj}}|} \cdot \left[ \sec \left( \frac{\psi_j^r - \psi_j^s}{2} \right) \mp \sec \left( \frac{\psi_j^r + \psi_j^s}{2} \right) \right] \quad (74)$$

Following the development of part B, the currents  $M_R^\ell$  and  $M_R^{\ell d}$  generate the reflected modal amplitude  $A_r^-$  associated with the reflected modal field  $(\bar{E}_r^-; \bar{H}_r^-)$  as in (52) and (53); thus:

$$A_{nm}^- = \frac{\sum_{j=1}^N \int_{\text{rim}(z=0)} (d\ell' [\bar{h}_{nm}^\ell \cdot M_R^\ell \hat{e}^\ell + \hat{z} h_{nm}^\ell \cdot M_R^{\ell d} \hat{e}^\ell] e^{-j\beta_{nm}^\ell z})}{2 \iint_{\text{aperture } (z=0)} ds \hat{z} \cdot (\bar{e}_{nm}^\ell \times \bar{h}_{nm}^\ell)} \quad (75)$$

and

$$B_{nm}^- = \frac{\sum_{j=1}^N \int_{\text{rim}(z=0)} (d\ell' [\bar{h}_{nm}^\ell \cdot M_R^\ell \hat{e}^\ell] e^{-j\beta_{nm}^\ell z})}{2 \iint_{\text{aperture } (z=0)} ds \hat{z} \cdot (\bar{e}_{nm}^\ell \times \bar{h}_{nm}^\ell)} \quad (76)$$

where

$$\begin{bmatrix} [A_r^-] \\ [A_{nm}^-] \\ [B_{nm}^-] \end{bmatrix} \equiv \begin{bmatrix} [A_r^+] \\ [A_{pq}^+] \\ [B_{pq}^+] \end{bmatrix} \quad (77)$$

$$\begin{bmatrix} [A_s^+] \\ [B_{pq}^+] \end{bmatrix} \quad . \quad (78)$$

It is clear that  $M_R^\ell$  and  $M_R^{\ell d}$  in (75) and (76) contain  $A_s^+$  which are the modal amplitudes of  $(\bar{E}_s^+; \bar{H}_s^+)$  via (72) and (73); hence, the elements of the reflection coefficient matrix  $[S_{22}]$  may be easily obtained (even by

inspection) from (16), (17), (75) and (76) together with (73), (74), (77) and (78).

The modal reflection coefficients or the elements of  $[S_{22}]$  for the circular inlet configuration, which are calculated by the equivalent current method (ECM) described above are compared with those based on the exact Wiener-Hopf solution in Figures 35 - 38. This comparison in Figures 35 - 38 is also quite good. Once again, it is noted that the exact Wiener-Hopf solution [17] is far more complicated than the present one based on the ECM. It is noted that the effects of the multiple diffractions of the rays across the aperture are included in the evaluation of the equivalent currents for the ECM analysis of  $[S_{22}]$  pertaining to the circular inlet cases as shown in Figures 35 - 38. The details of the procedure for including these multiple interactions can be found in [9]; that approach has been used here as well with the final expression given in Appendix IV. In Figures 39 - 40, results for the modal reflection coefficients are shown for open ended rectangular waveguides (or inlets), and a comparison of one such calculation with measurement [18] is shown in Figure 41 for the dominant  $TE_{10}$  rectangular waveguide mode. The comparison with measurements in Figure 41 is reasonable; one would expect this comparison to improve as the frequency increases. The measurements in Figure 41 were performed at a frequency for which the waveguide dimensions are quite small in terms of the wavelength, thereby straining the high frequency ECM solution; it is possible that multiple interactions of waves across the aperture can become important at such lower frequencies; on the other hand, the ECM

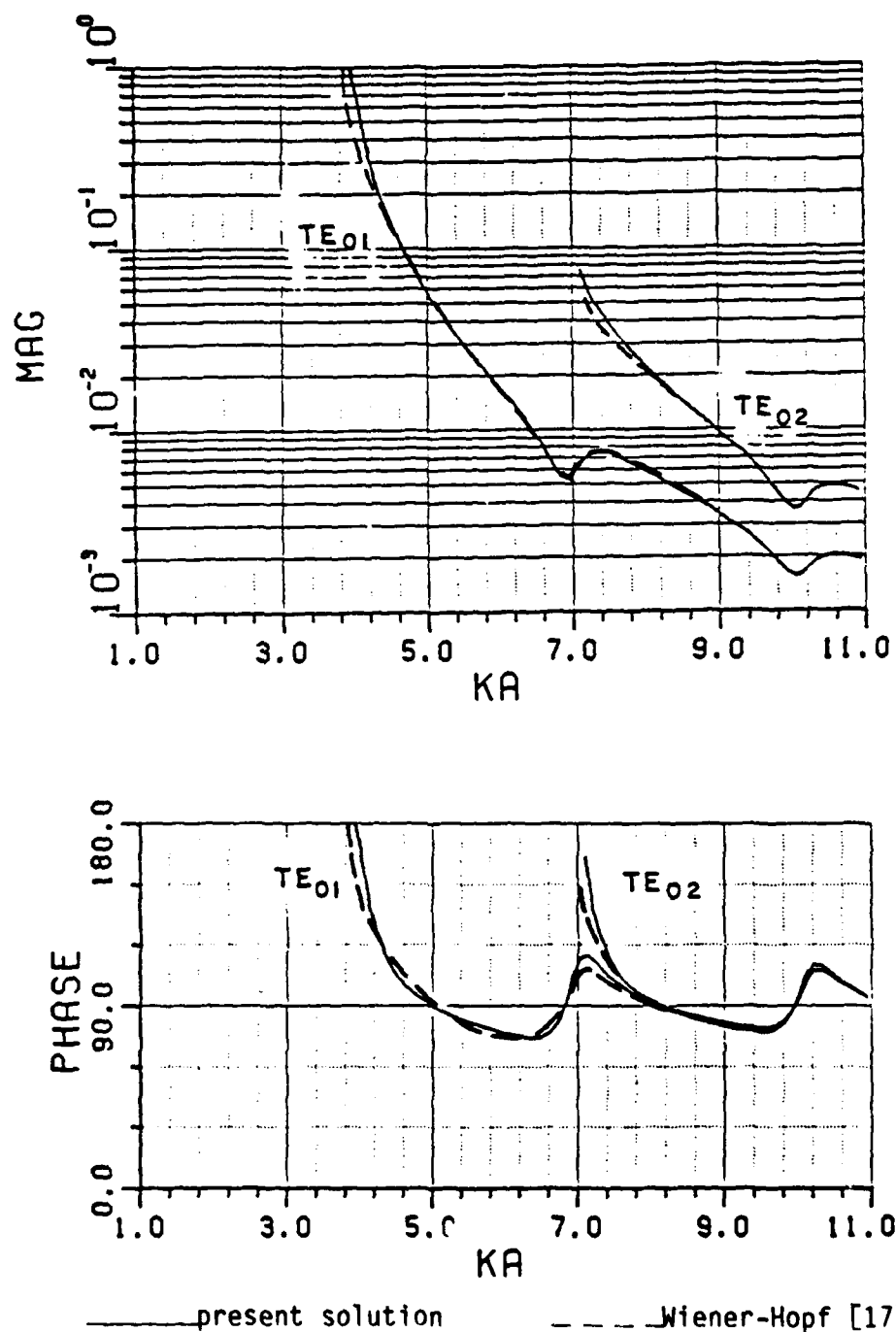


Figure 35. Modal reflection coefficients due to an incident  $TE_{01}$  mode in an open-ended circular waveguide.

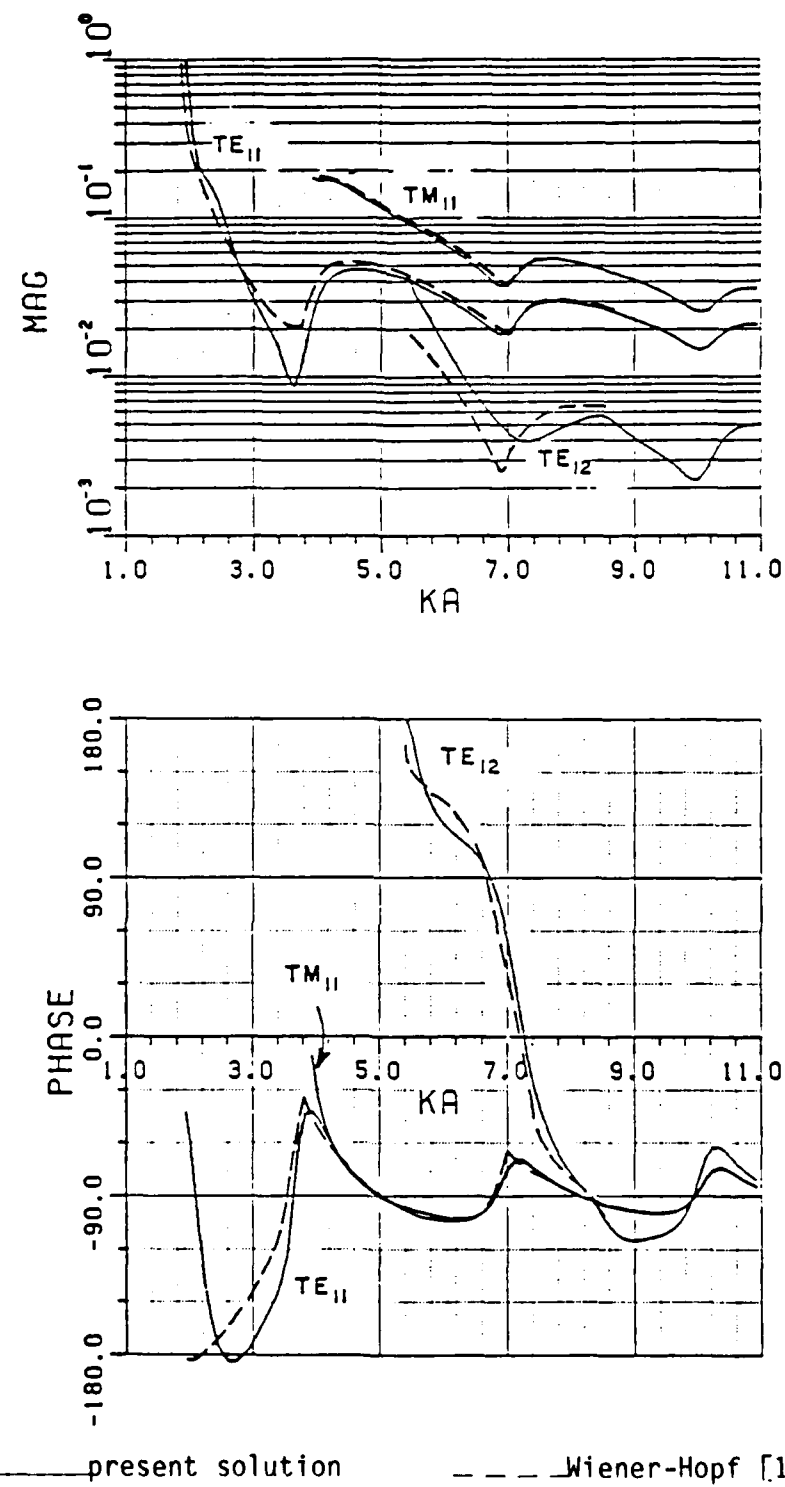


Figure 36. Modal reflection coefficients due to an incident  $TE_{11}$  mode in an open-ended circular waveguide.

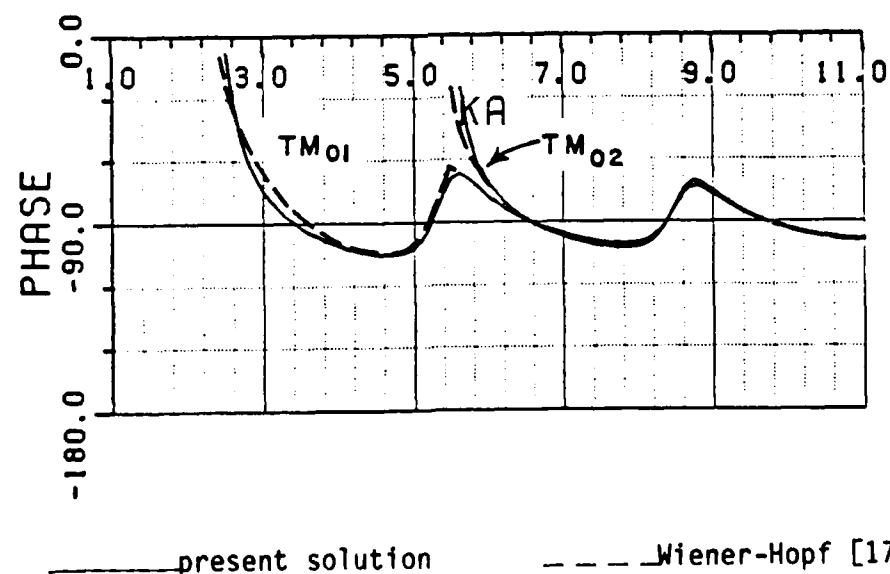
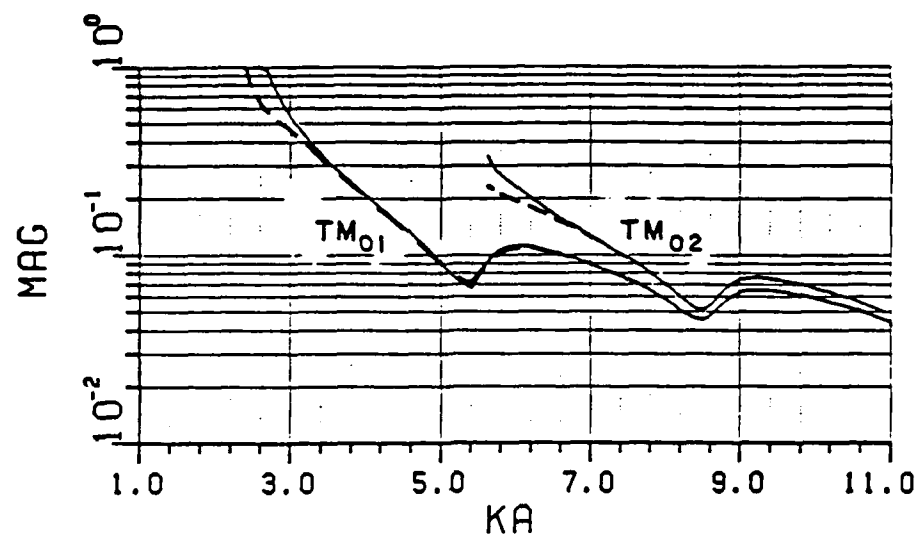


Figure 37. Modal reflection coefficients due to an incident  $TM_{01}$  mode in an open-ended circular waveguide.

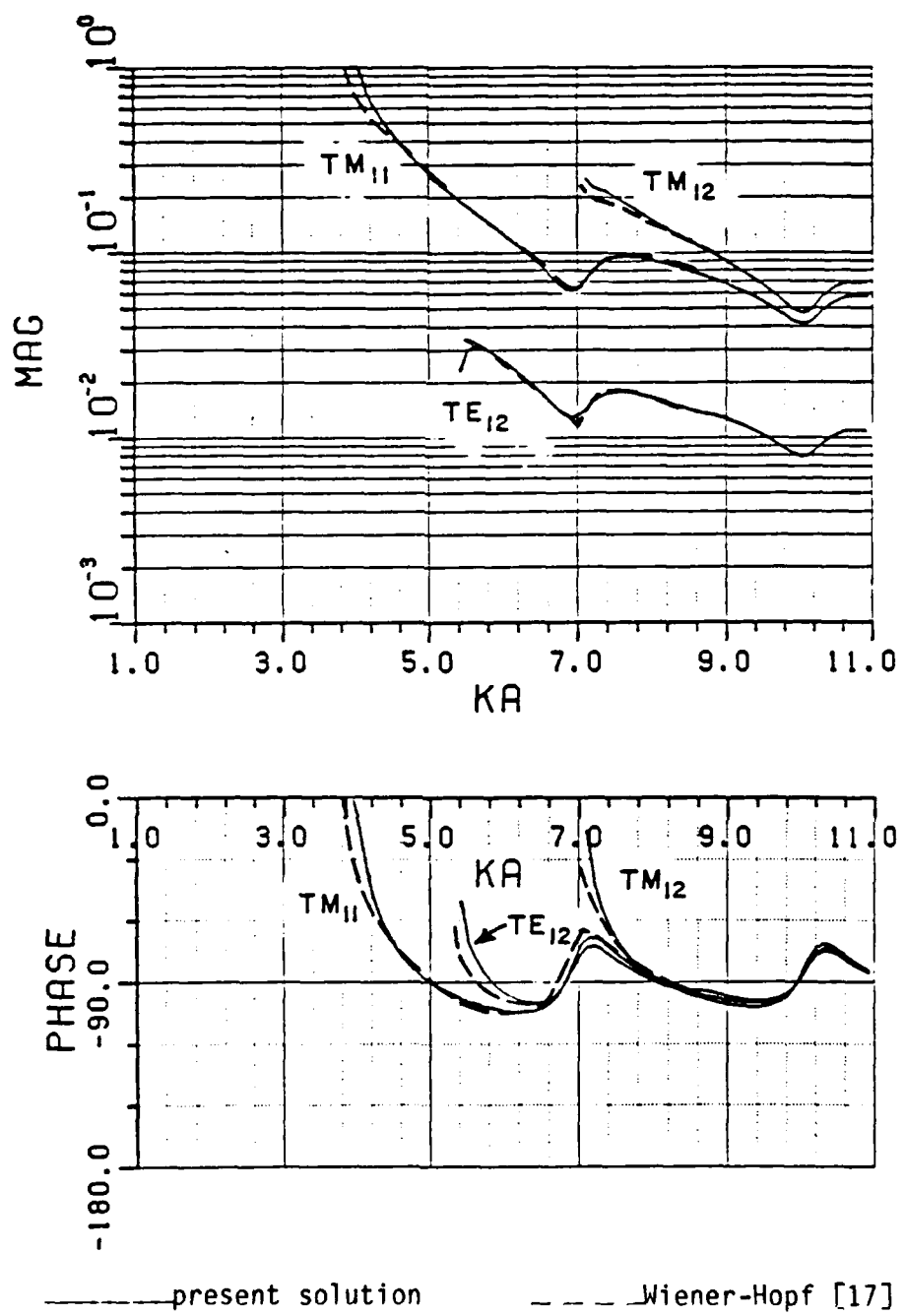


Figure 38. Modal reflection coefficients due to an incident  $TM_{11}$  mode in an open-ended circular waveguide.

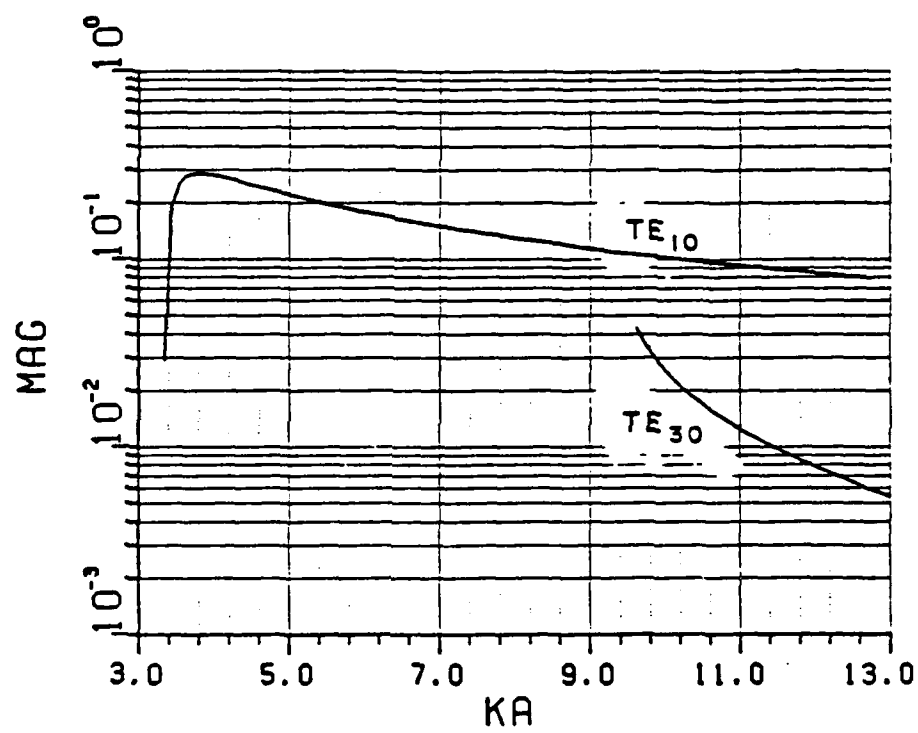


Figure 39. Modal reflection coefficients due to an incident  $TE_{10}$  mode in an open-ended rectangular waveguide ( $a=2b$ ).

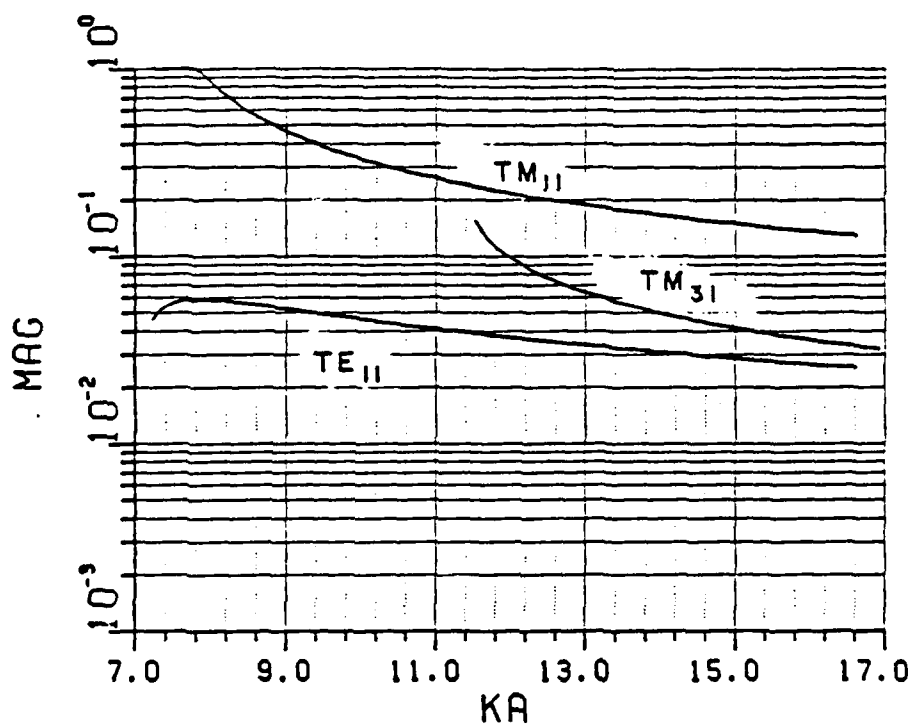


Figure 40. Modal reflection coefficients due to an incident  $TM_{11}$  mode in an open-ended rectangular waveguide ( $a=2b$ ).

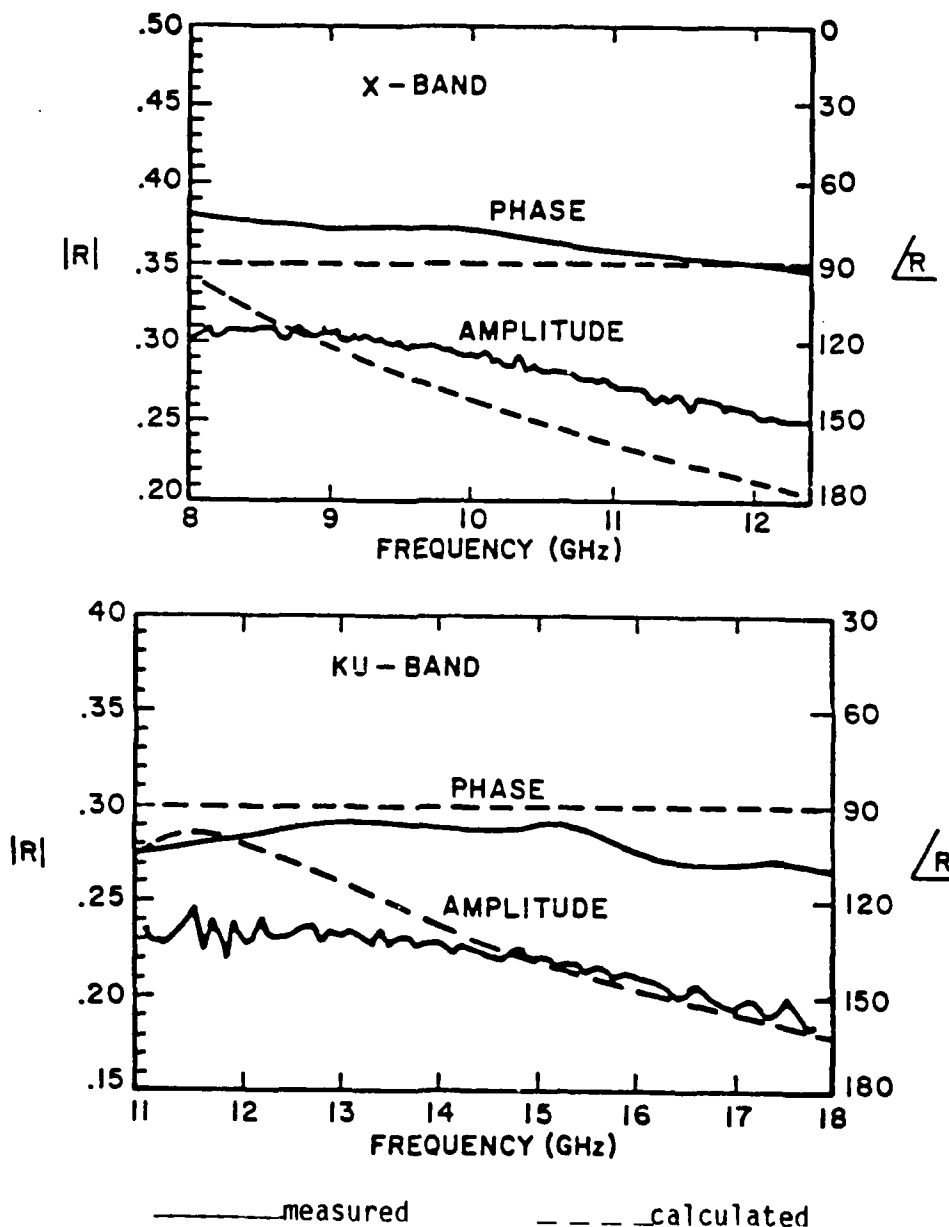


Figure 41. Comparisons of the calculated and measured reflection coefficients in an x-band and ku-band open-ended rectangular waveguide.

solution can become more cumbersome if these multiple wave interactions are included for the rectangular inlet case. The effect of multiple wave interactions across the aperture is more easily calculated in the case of the circular inlet geometry.

#### F. Development of $[S_r]$

The matrix  $[S_r]$  contains elements which are the reflection coefficients of the modes reflected from the termination at  $z=-L$  in Figure 6 when a set of modes is incident upon this termination. Let an  $r^{\text{th}}$  modal field  $(\bar{E}_r^-; \bar{H}_r^-)$  of the  $TE_r$  or  $TM_r$  type be incident on the termination at  $z=-L$  in Figure 6, and let  $(\bar{E}_s^+; \bar{H}_s^+)$  denote the fields of an  $s^{\text{th}}$   $TE_s$  or  $TM_s$  mode reflected from that termination. The matrix  $[\bar{S}_r^+]$  then relates the fields  $(\bar{E}_s^+; \bar{H}_s^+)$  reflected from the termination at  $z=-L$  to the incident fields  $(\bar{E}_r^-; \bar{H}_r^-)$ .

For an impedance termination, the matrix elements of  $[S_r]$  can be trivially obtained by enforcing the impedance boundary condition (at  $z=-L$ ) on the total fields; namely:

$$[\bar{E} - \hat{z} \hat{z} \cdot \bar{E} = Z_s \hat{z} \times \bar{H}]_{z=-L} \quad (79)$$

with

$$\bar{E} = \bar{E}_r^- A_r^- + \sum_s \bar{E}_s^+ A_s^+ ; \quad (80)$$

$$\bar{H} = \bar{H}_r^- A_r^- + \sum_s \bar{H}_s^+ A_s^+ \quad (81)$$

in which  $\sum_s (\bar{E}_s^+; \bar{H}_s^+)$  are the reflected fields of all the "s" modes when only an  $r^{\text{th}}$  set of modal fields  $(\bar{E}_r^-; \bar{H}_r^-)$  is incident on the impedance termination at  $z=-L$ . Here,  $Z_s$  denotes the value of the surface impedance. The elements of  $[S_T]$  as defined in (18) and (19) can be identified by simply incorporating (80) and (81) into (79), and by invoking the orthogonality property of the waveguide modes. It can be easily verified that  $[S_T]$  is a diagonal matrix.

For a planar isotropic homogeneous dielectric/ferrite at  $Z=-L$  which is characterized by the permeability  $\mu_r \mu_0$  and permittivity  $\epsilon_r \epsilon_0$ , the elements of the matrix  $[S_r]$  can be found as follows:

For TM modes:

$$S_r^{ee} = \frac{\tilde{\beta}_{nm} - \epsilon_r \beta_{nm}}{\tilde{\beta}_{nm} + \epsilon_r \beta_{nm}}$$

For TE modes:

$$S_r^{hh} = \frac{\mu_r \tilde{\beta}_{nm} - \tilde{\beta}_{nm}}{\mu_r \tilde{\beta}_{nm} + \tilde{\beta}_{nm}}$$

where

$$\tilde{\beta}_{nm} = \sqrt{k_0^2 \mu_r \epsilon_r - k_c^2}$$

$$\beta_{nm} = \sqrt{k_0^2 - k_c^2}$$

and

$$k_c^2 = \begin{cases} \left(\frac{n\pi}{a}\right)^2 + \left(\frac{m\pi}{b}\right)^2 & \text{for a rectangular waveguide.} \\ \left(\frac{p_{nm}}{a}\right)^2 & \text{for circular waveguide TM modes.} \\ \left(\frac{p'_{nm}}{a}\right)^2 & \text{for circular waveguide TE modes.} \end{cases}$$

For many materials of interest, the relative permeability  $\mu_r \approx 1$ , therefore the reflection from the termination for TE mode can be simplified as

$$S_r^{hh} = \frac{\beta_{nm} - \tilde{\beta}_{nm}}{\beta_{nm} + \tilde{\beta}_{nm}}.$$

The reflection coefficients for blade/disk and hub structure terminations in circular inlets are slightly more complicated and are presented in Appendix VI.

#### IV. NUMERICAL RESULTS AND COMPARISONS WITH MEASUREMENTS FOR THE SCATTERING BY THE COMPLETE INLET CONFIGURATIONS OF FIGURE 1.

In the previous section, the various generalized scattering matrices were developed corresponding to the canonical scattering events depicted in Figures 3 - 6; also, numerical results illustrating the behavior of these scattering mechanisms were included. Comparisons with exact calculations or measurements were made whenever reasonably possible to indicate the accuracy of the mathematical expressions which were developed to describe these scattering mechanisms; those

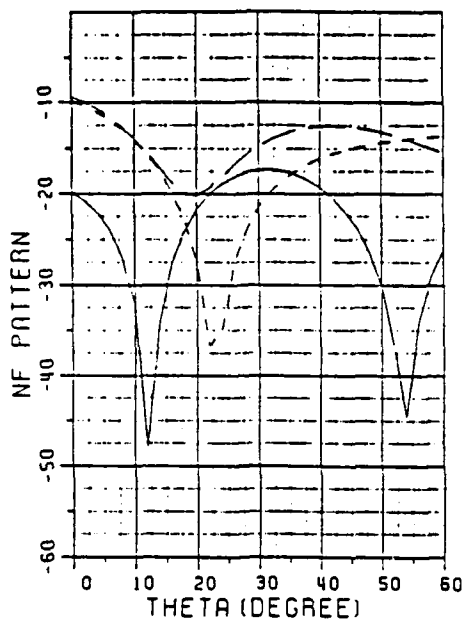
expressions were derived via asymptotic high frequency techniques (such as GTD, UTD, ECM or modified PTD). Asymptotic high frequency techniques by their very nature are approximate; they are expected to become increasingly more accurate with increase in frequency. However, most asymptotic high frequency solutions are known to work reasonably accurately almost down to frequencies where the characteristic dimensions of the radiating object are not much larger than a wavelength; this is also observed in the present study. In this development it is necessary that the inlet cross-section be large enough to where at least the dominant mode can be excited within the inlet waveguide region.

Also, because of the complexity of obtaining the eigenvalues in a circular inlet, the computer program for obtaining numerical results for the scattered fields can now handle a circular inlet with radius up to 5 wavelengths, or include up to 240 modes (with the understanding that there are two independent azimuthal wave functions  $\cos n\phi$  and  $\sin n\phi$  in each waveguide mode). For rectangular inlets, there is no such restriction, since the calculation of the eigenvalues is very simple. However, the calculation of scattering from extremely large inlets is still not practical due to the fact that numerous modes have to be included in the calculation. Further studies in selecting significant modes and different useful high frequency representations of waveguide modes are necessary in order to get a more efficient way to estimate the scattering of large waveguides [19,20].

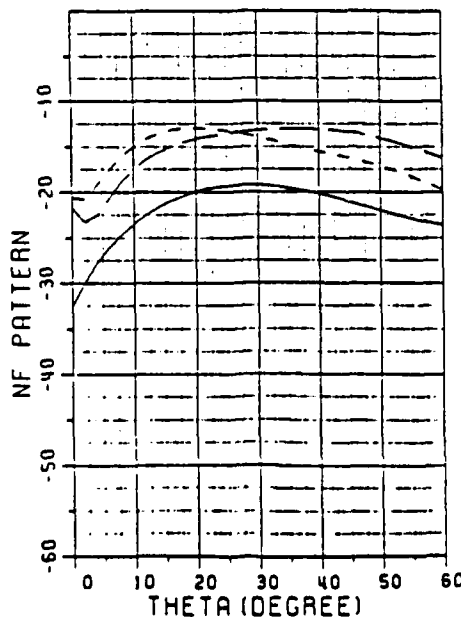
The calculated numerical results shown in Figures 42 - 48 include the effect of rim scattering (i.e., the solid line \_\_\_\_\_), the field

For the effect of rim scattering, the scattered field peaks up in the neighborhood of the specular region (i.e., close to  $\theta^r = \theta^i$ ,  $\phi^r = \phi^i + \pi$ ) as is to be expected from the GTD point of view. But for the field scattered by the termination, there are no special rules as to where the total field should peak up. The field scattered by the termination comes from a combination of the radiation from different modes, and the phase between the modes will change the radiation pattern dramatically. However, if one is only interested in a specific region, one can pick up the modes which contribute most significantly to that region using the concepts in [19,20]. In the latter instance, the distribution of the field within the inlet, which radiates out to correspond to the field scattered by the termination is controlled by the interaction of the propagating modes. Therefore, when the length of the inlet termination is changed, the energy will be redistributed within the various modes. For the case of a short circuited termination, the scattered field from the termination is usually greater than the field scattered from the rim except in the specular region. By changing the impedance of the termination, from zero (short circuit

VP( EPH ) CIRC. WAVEGUIDE (A,L) = ( 1.00, 10.00 )  
 UNIT=LUMO8A SHORT END JJP= 20  
 PLANE WAVE INCIDENCE (TH,PHI) = ( 30.0, 0.0 )  
 NEAR ZONE RECEIVING (R,PH) = ( 4.000,180.0 )



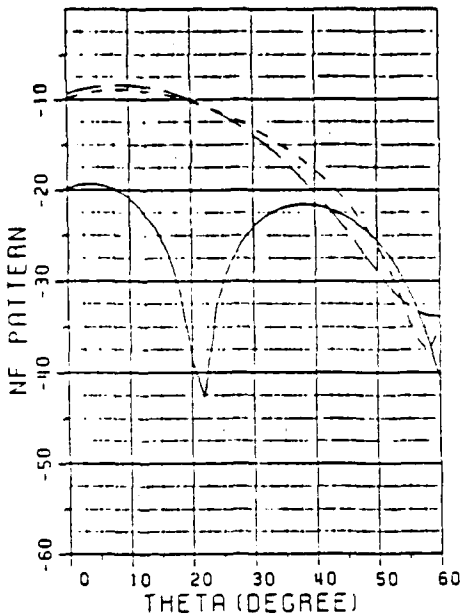
HP( ETH ) CIRC. WAVEGUIDE (A,L) = ( 1.00, 10.00 )  
 UNIT=LUMO8A SHORT END JJP= 20  
 PLANE WAVE INCIDENCE (TH,PHI) = ( 30.0, 0.0 )  
 NEAR ZONE RECEIVING (R,PH) = ( 4.000,180.0 )



——— rim scattering  
 - - - - return from termination  
 - - - - total field

Figure 42. Contributions to the  $\phi=180^\circ$  patterns for circular inlet.

VP( EPH ) CIRC. WAVEGUIDE (R,L) = ( 1.00, 10.00 )  
 UNIT=LUMINA SHORT END JJP= 20  
 PLANE WAVE INCIDENCE (TH,PHI) = ( 30.0, 0.0 )  
 NEAR ZONE RECEIVING (R,PHI) = ( 4.000, 0.0 )



HP( EPH ) CIRC. WAVEGUIDE (R,L) = ( 1.00, 10.00 )  
 UNIT=LUMINA SHORT END JJP= 20  
 PLANE WAVE INCIDENCE (TH,PHI) = ( 30.0, 0.0 )  
 NEAR ZONE RECEIVING (R,PHI) = ( 4.000, 0.0 )

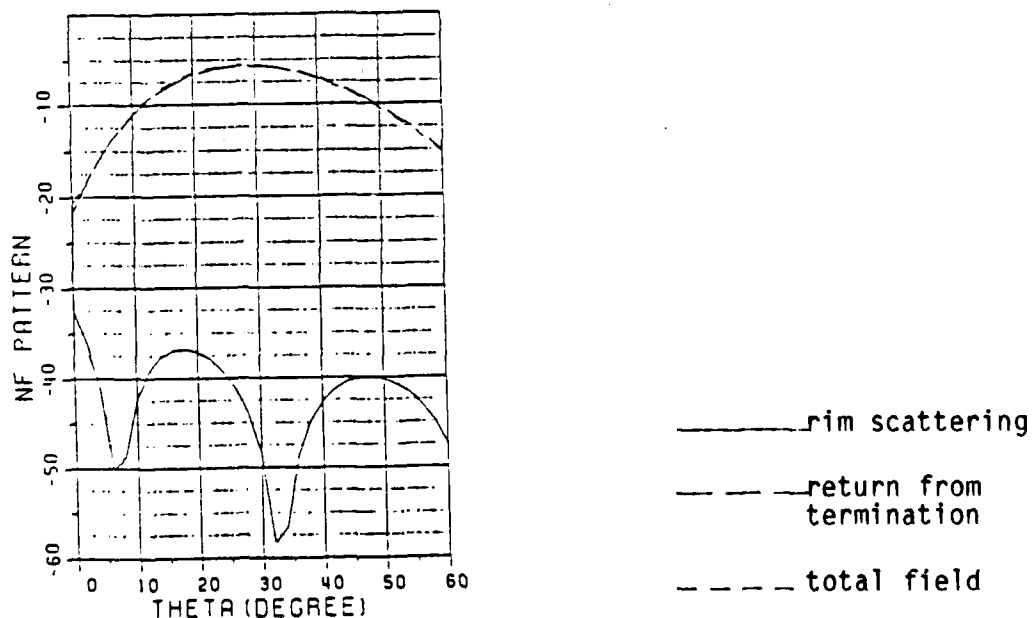
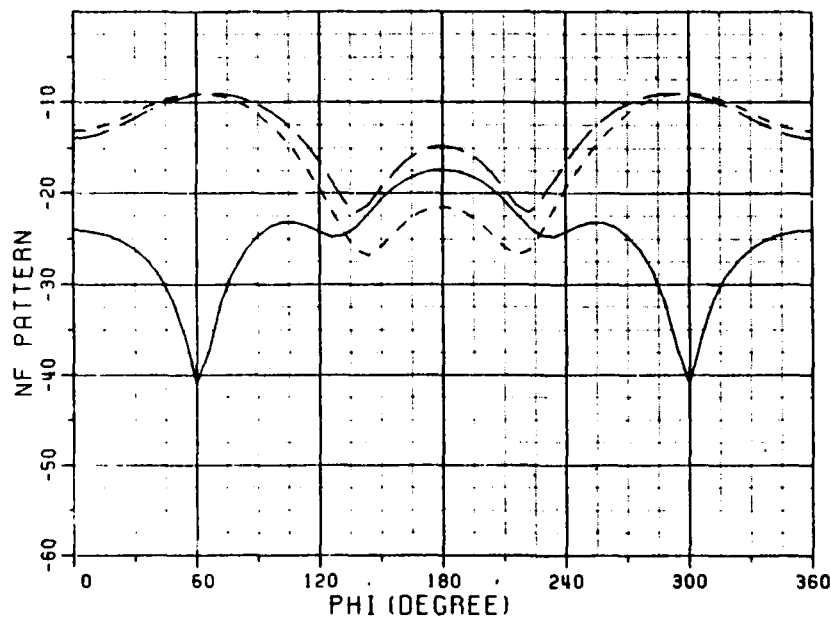


Figure 43. Contributions to the  $\phi=0^\circ$  patterns for circular inlet.

VP ( EPH ) CIRC. WAVEGUIDE (R,L) = ( 1.00, 10.00 )  
 UNIT=LUMDA SHORT END JJP= 20  
 PLANE WAVE INCIDENCE (TH,PHI) = ( 30.0, 0.0 )  
 NEAR ZONE RECEIVING (R,TH) = ( 4.000, 30.0 )



HP ( ETH ) CIRC. WAVEGUIDE (R,L) = ( 1.00, 10.00 )  
 UNIT=LUMDA SHORT END JJP= 20  
 PLANE WAVE INCIDENCE (TH,PHI) = ( 30.0, 0.0 )  
 NEAR ZONE RECEIVING (R,TH) = ( 4.000, 30.0 )

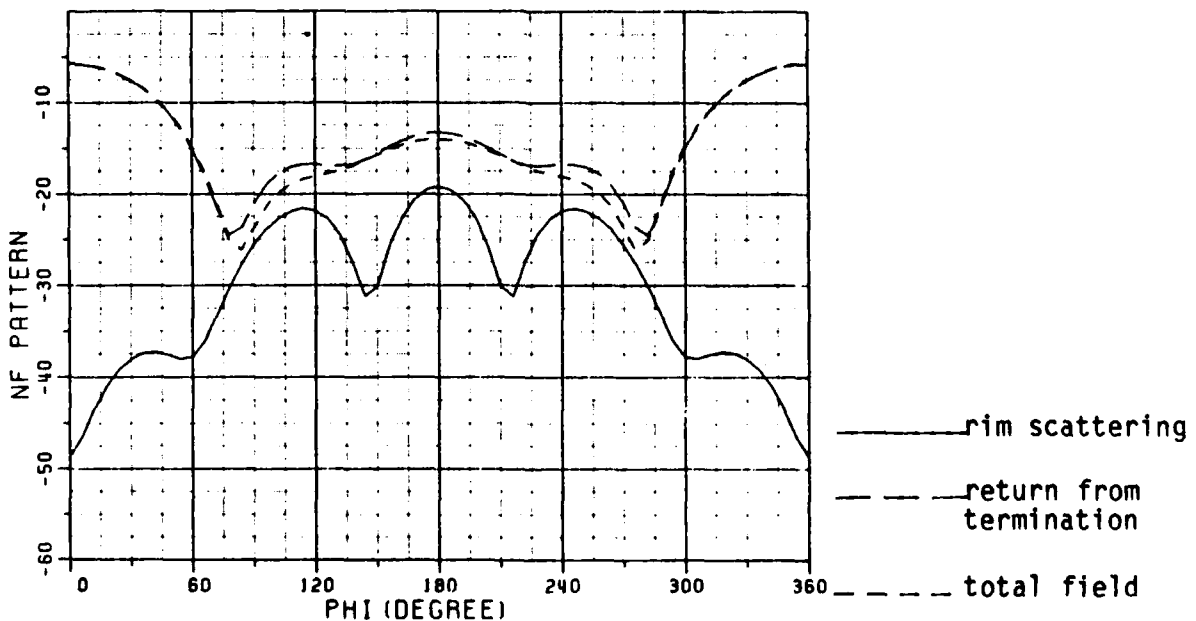
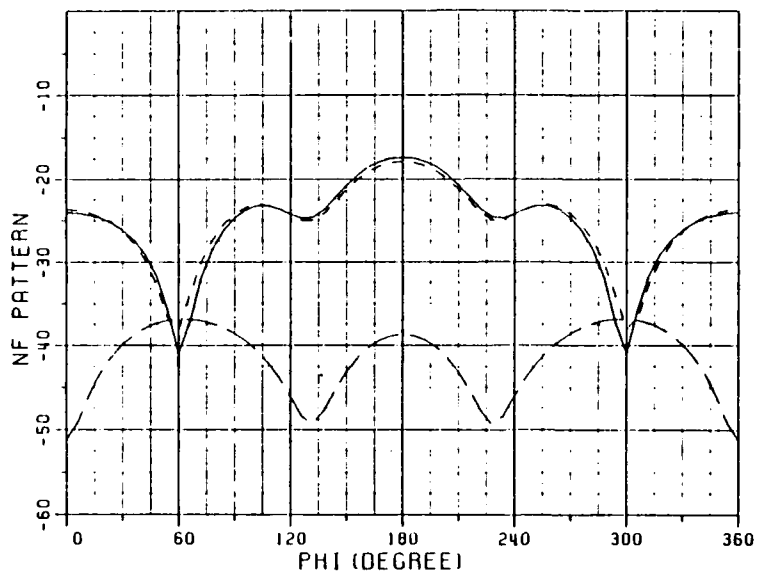


Figure 44. Contributions to the 30° cone scan patterns for circular inlet.

VP1 EPH1 CIRC. WAVEGUIDE (A,L) = ( 1.00, 10.00)  
 UNIT=LAMBD EPR=( 0.100E+01, -0.100E+00) JJP= 20  
 PLANE WAVE INCIDENCE (TH,PHI)=( 30.0, 0.0)  
 NEAR ZONE RECEIVING (R,THI)=( -4.000, 30.0)



HP1 EPH1 CIRC. WAVEGUIDE (A,L) = ( 1.00, 10.00)  
 UNIT=LAMBD EPR=( 0.100E+01, -0.100E+00) JJP= 20  
 PLANE WAVE INCIDENCE (TH,PHI)=( 30.0, 0.0)  
 NEAR ZONE RECEIVING (R,THI)=( -4.000, 30.0)

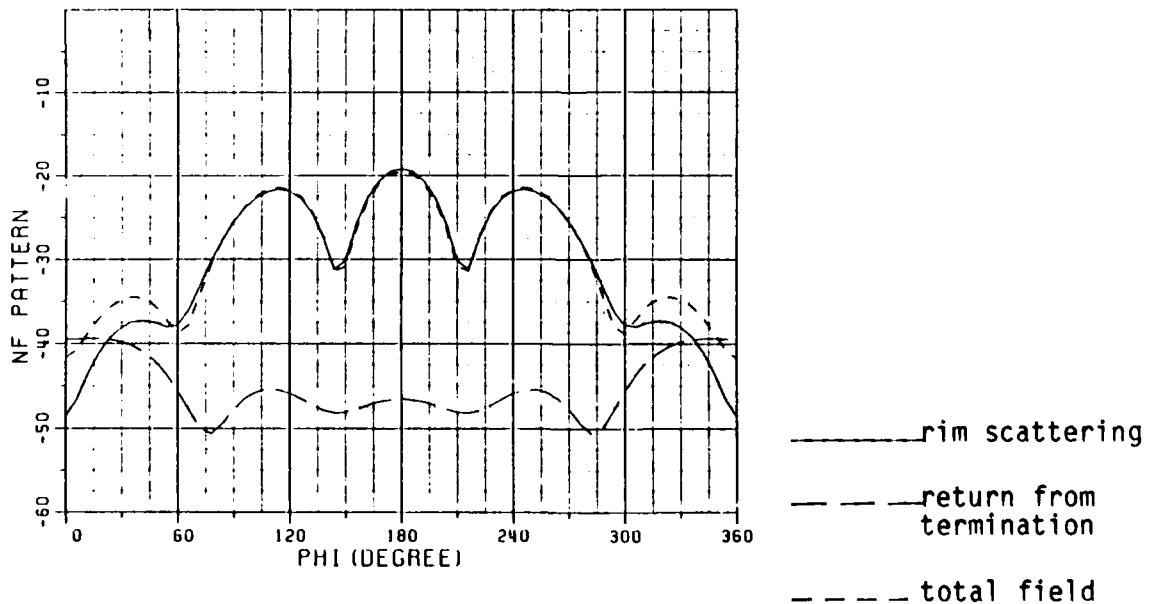
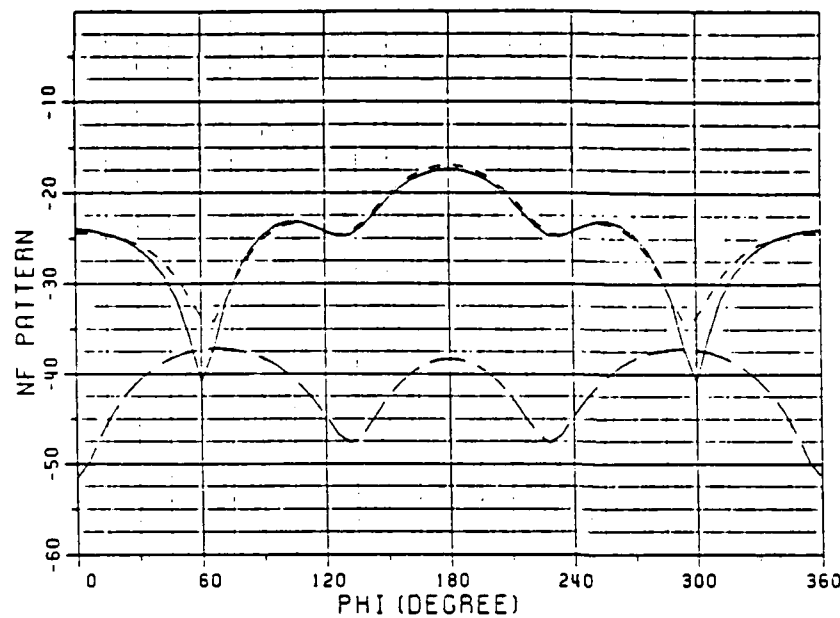


Figure 45. Contributions to the  $30^\circ$  cone scan patterns for circular inlet with almost matched termination. ( $\epsilon_r = 1-0.1j$ )

VP( EPH ) CIRC. WAVEGUIDE (A,L) = ( 1.00, 10.00 )  
 UNIT=LUMDA EPR=( 0.100E+01, 0.100E+00 ) JJP= 20  
 PLANE WAVE INCIDENCE (TH,PHI)=( 30.0, 0.0 )  
 NEAR ZONE RECEIVING (R,TH) = ( 4.000, 30.0 )



HP( ETH ) CIRC. WAVEGUIDE (A,L) = ( 1.00, 10.00 )  
 UNIT=LUMDA EPR=( 0.100E+01, 0.100E+00 ) JJP= 20  
 PLANE WAVE INCIDENCE (TH,PHI)=( 30.0, 0.0 )  
 NEAR ZONE RECEIVING (R,TH) = ( 4.000, 30.0 )

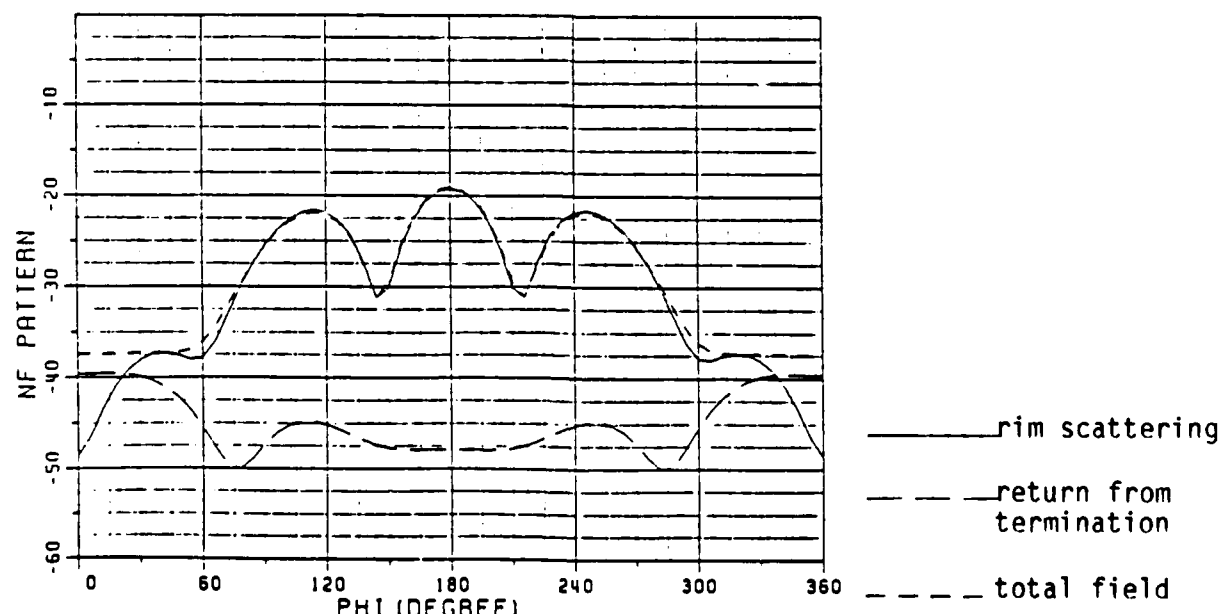
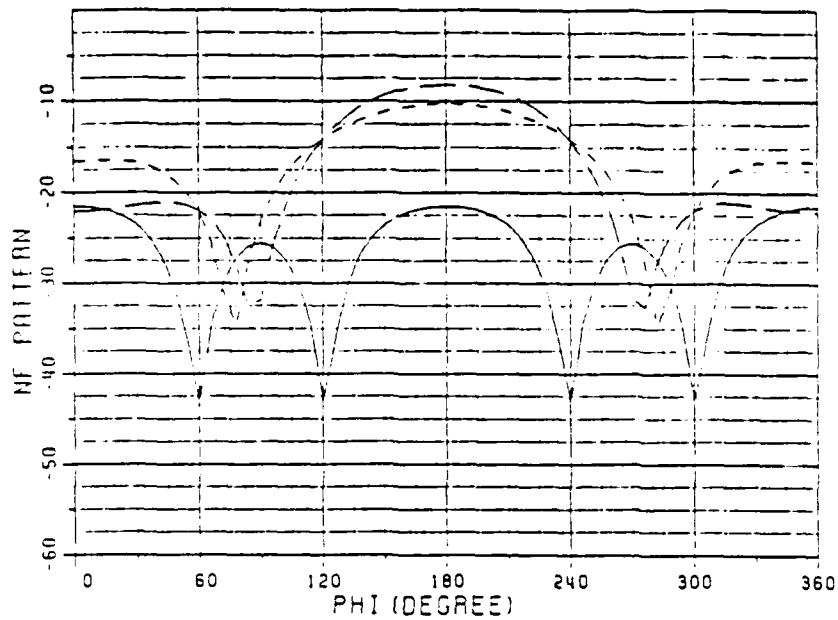


Figure 46. Contributions to the 30° cone scan patterns for rectangular inlet with size (A,B) = (2,1).

VP ( EPH 1 RECT. WAVEGUIDE (A,B,L) = ( 2.00, 1.00, 10.00  
 UNIT=LUMDA SHORT END JJP = 10  
 PLANE WAVE INCIDENCE (TH,PHI) = ( 30.0, 0.0)  
 NEAR ZONE RECEIVING (R,TH) = ( 4.000, 30.0)



HP ( ETH 1 RECT. WAVEGUIDE (A,B,L) = ( 2.00, 1.00, 10.00  
 UNIT=LUMDA SHORT END JJP = 10  
 PLANE WAVE INCIDENCE (TH,PHI) = ( 30.0, 0.0)  
 NEAR ZONE RECEIVING (R,TH) = ( 4.000, 30.0)

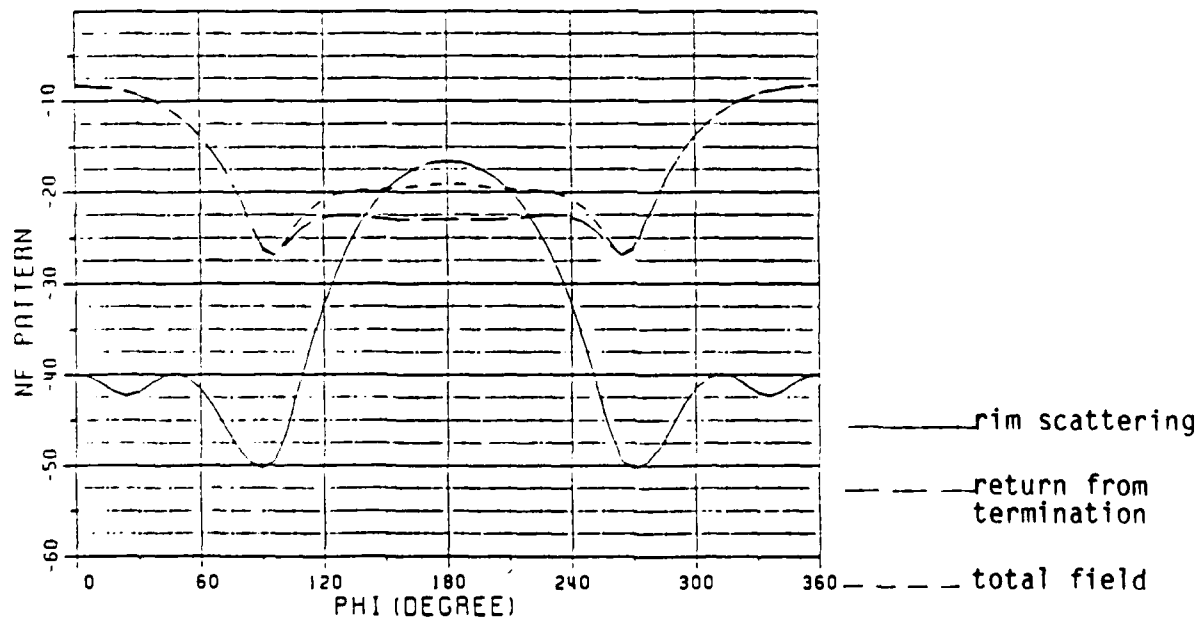
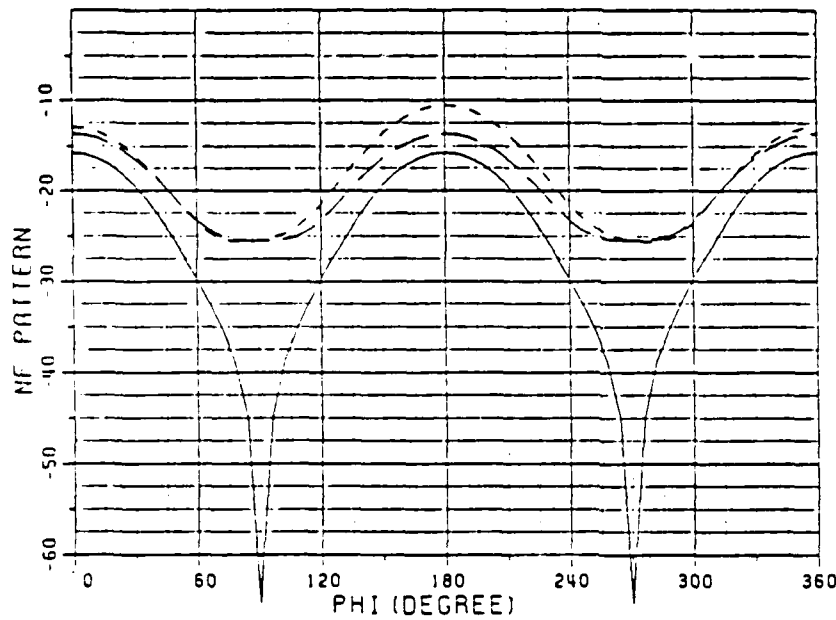


Figure 47. Contributions to the 30° cone scan patterns for a rectangular inlet with size (A,B) = (1,2).

VP, EPM 1 RECT. WAVEGUIDE (A,B,L) = ( 1.00, 2.00, 10.00  
 UNIT=LUMDA SHORT END JJP= 10  
 PLANE WAVE INCIDENCE (TH,PHI)=( 30.0, 0.0)  
 NEAR ZONE RECEIVING (R,THI) = ( 4.000, 30.0)



HP ( ETH ) RECT. WAVEGUIDE (A,B,L) = ( 1.00, 2.00, 10.00  
 UNIT=LUMDA SHORT END JJP= 10  
 PLANE WAVE INCIDENCE (TH,PHI)=( 30.0, 0.0)  
 NEAR ZONE RECEIVING (R,THI) = ( 4.000, 30.0)

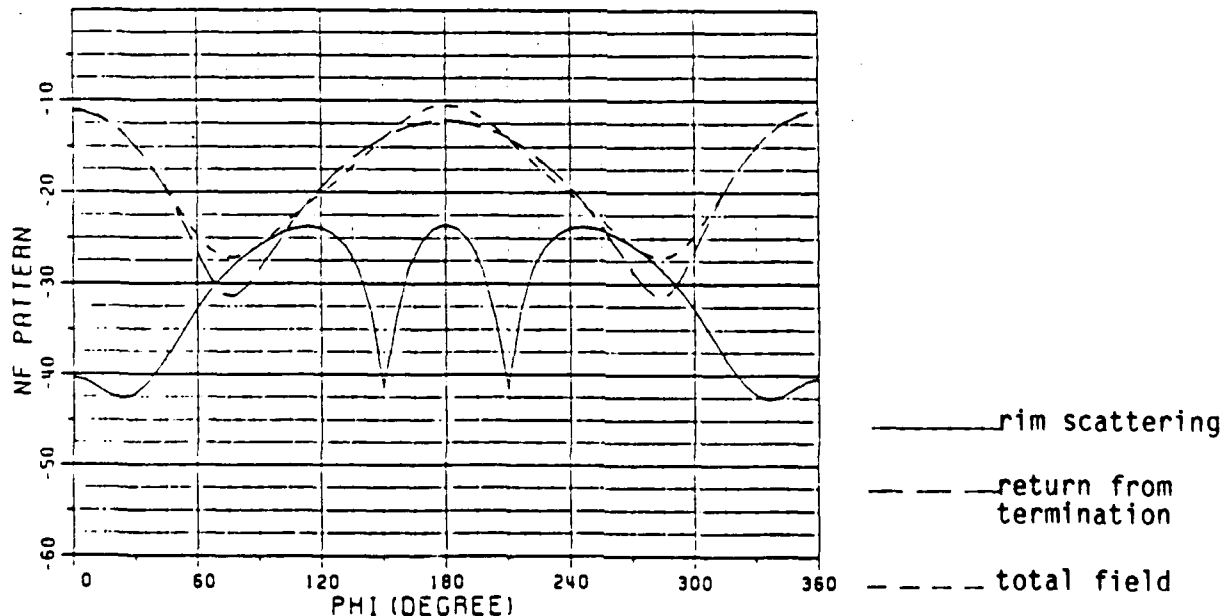
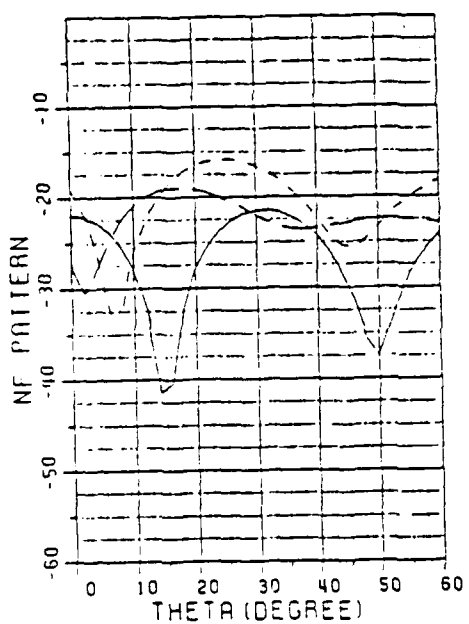


Figure 48. Contributions to the  $\phi=0^\circ$  patterns for a rectangular inlet with size  $(A,B) = (2,1)$ .

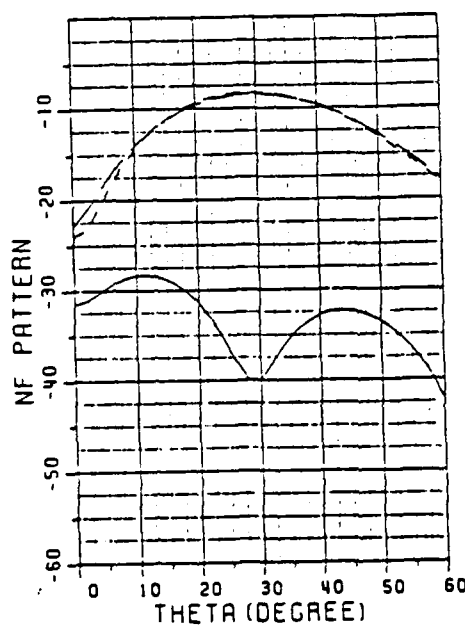
VP ( EPH ) RECT. WAVEGUIDE (A,B,L) = ( 2.00, 1.00, 10.00 )  
 UNIT=LUMDA SHORT END JJP= 10  
 PLANE WAVE INCIDENCE (T),PHI) = ( 30.0, 0.0 )  
 NEAR ZONE RECEIVING (R,PHI) = ( 4.000, 0.0 )



(a) On-axis RCS (normalized  $\pi a^2$ ) of a hollow, perfectly conducting finite length circular open at the front end and closed (shorted) at the back end.

Figure 49. On-axis RCS.

$HP(ETH) \text{ RECT. WAVEGUIDE } (A, B, L) = (2.00, 1.00, 10.00)$   
 UNIT=LUMDA SHORT END JJP= 10  
 PLANE WAVE INCIDENCE (TH, PH1)=(30.0, 0.0)  
 NEAR ZONE RECEIVING (A, PH1)=(4.000, 0.0)



(b) On-axis RCS (normalized  $\pi a^2$ ) of a hollow, perfectly conducting finite length circular cylinder open at both ends.

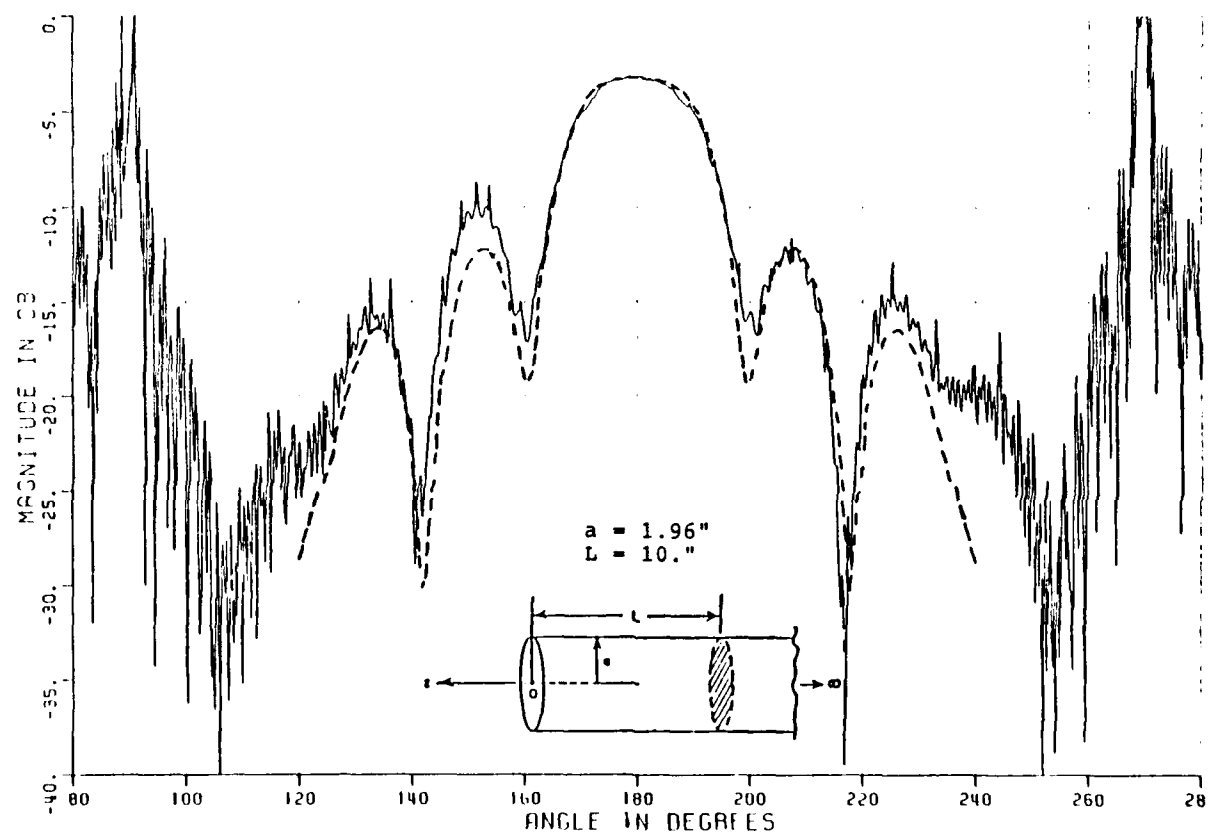
Figure 49. Continued.

case) to one which has a non-zero real part (corresponding to a lossy impedance), one can drop the level of the field scattered by the termination. Some related results which were computed previously [9] are also included in Figure 49 for completeness.

Comparisons of calculated and measured backscattering results for the circular inlet case are considered next. The measurements were performed at the Ohio State University ElectroScience Laboratory [21]. The circular inlet may be terminated inside by one of the following structures: a planar conductor (short circuit), a planar impedance surface, a blade-disk structure, and conical and hemispherical hubs which may sit on a planar disk or a disk-blade structure. In Figures 50 through 57, the solid curves are the measured and the dashed curves the calculated backscattering results. Figures 50 and 51 show the comparison of the calculated and measured backscattering patterns for a circular inlet with a short circuit termination at three different frequencies for vertical ( $\hat{\phi}$ ) and horizontal ( $\hat{\theta}$ ) polarizations, respectively. Additional horizontal polarization patterns at 10 GHz and 10.2 GHz are shown in Figure 52 which illustrates the sensitivity in the change of horizontal polarization patterns with frequency. A comparison of backscattering patterns for a disk-blade termination is shown in Figure 53; likewise, they are shown in Figures 54 and 55 for the case of conical and hemispherical hubs on a planar disk, respectively, and in Figures 56 and 57 for conical and hemispherical hubs on a blade structure, respectively. It is observed that the P.O. approximation for determining the reflection from the termination seems to give a good

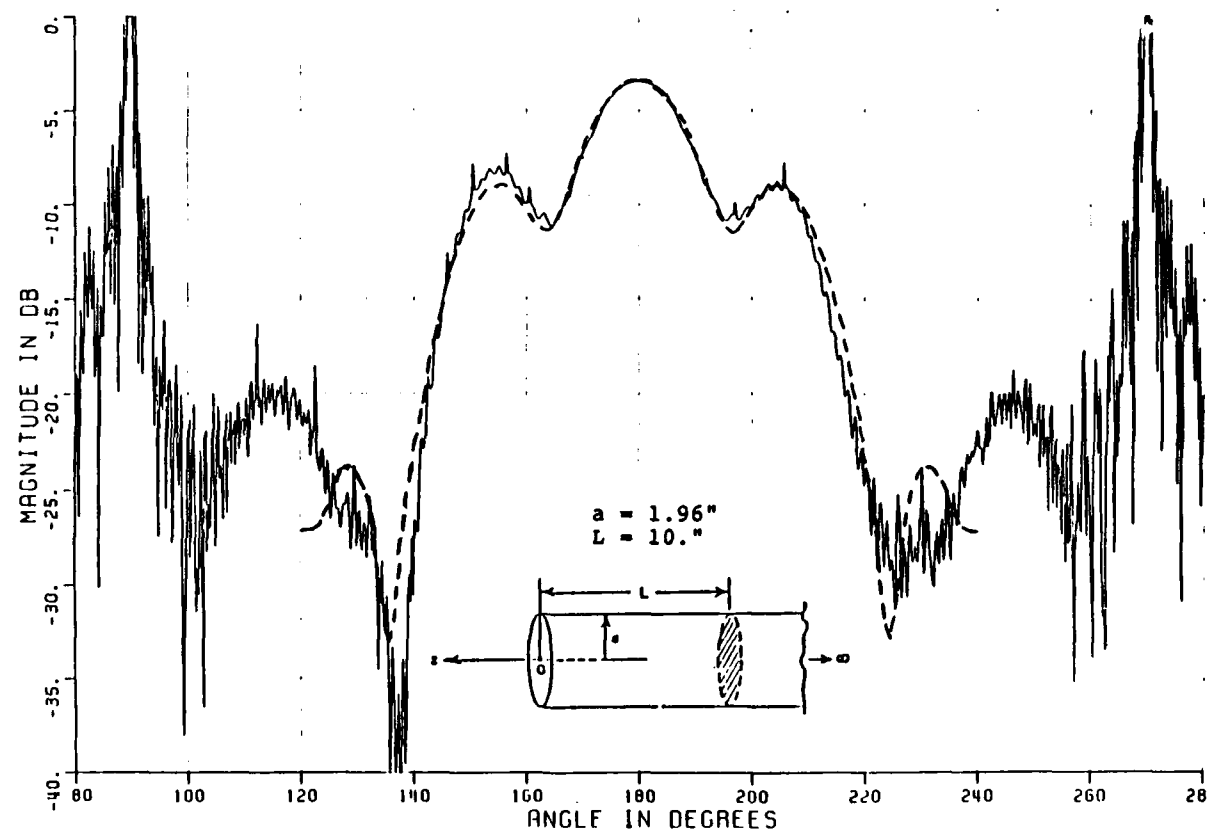
overall prediction of the patterns, except in a few cases involving blade terminations where the patterns may not compare sufficiently well with measurements, especially for the horizontal polarization case which appears to be more sensitive to parameter changes than the vertical polarization. This suggests that due to the presence of the blades, the interactions between the blades themselves, which are not accounted for in the P.O. approximation, could possibly have a non-negligible contribution to the scattering matrix  $S_r$ . Therefore, a refined analysis could be used to improve the accuracy of the calculated patterns for this case. In addition, the experimental model for the blades should be more carefully made than at present.

Due to the fast varying nature of the RCS patterns with frequency, some frequency scan patterns are also included. In particular, results for the calculated and measured frequency scan patterns are given in Figures 58 through 61. It is noted that the calculated backscattering returns in Figure 58 and 59 generally are stronger than the measured ones. This is due to the fact that in the measurements, the terminal conducting plane does not completely fill up the inlet cross section, allowing electromagnetic energy to pass through and this results in lower measured backscattering returns. It is important to note that the theoretical predictions show the same general trends in the variation of RCS with frequency as those predicted by the measurements.



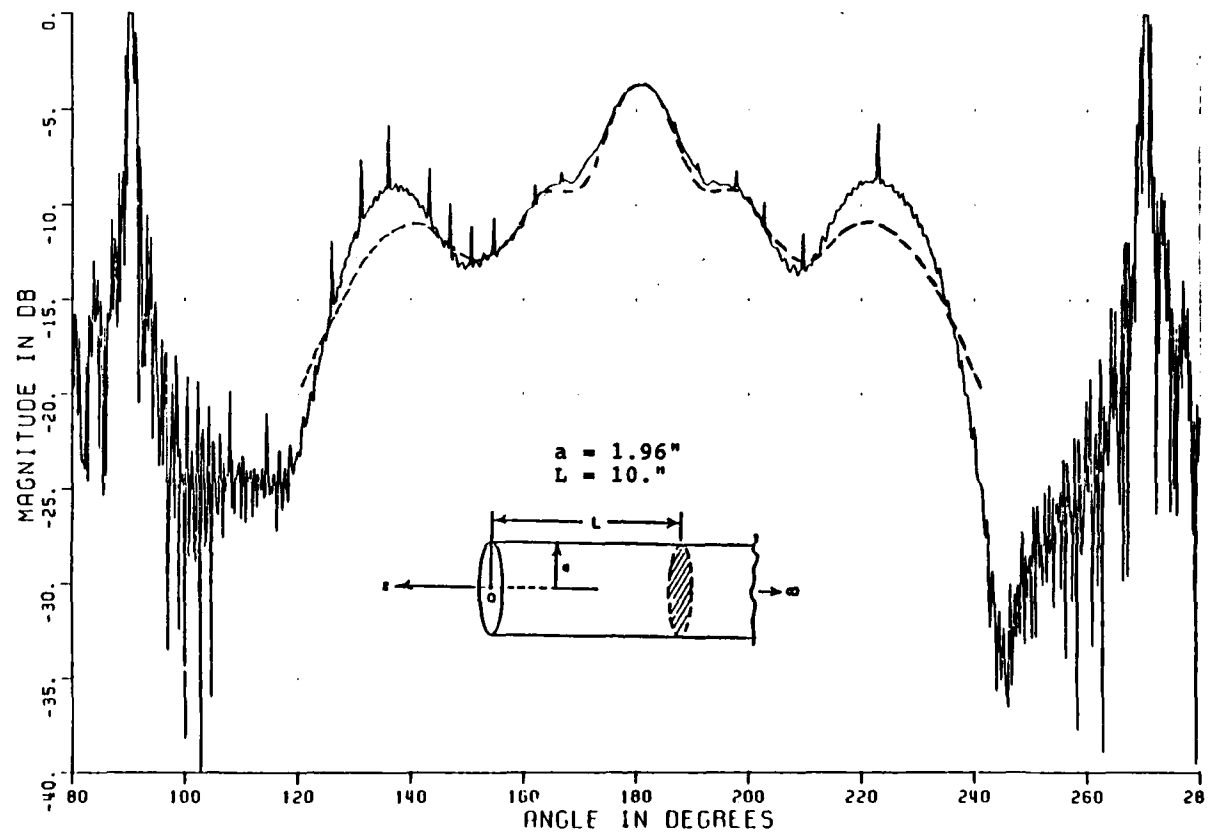
(a)

Figure 50. Comparisons of calculated and measured vertical polarization backscattering patterns at (a) 9 GHz, (b) 10 GHz, and (c) 11 GHz.



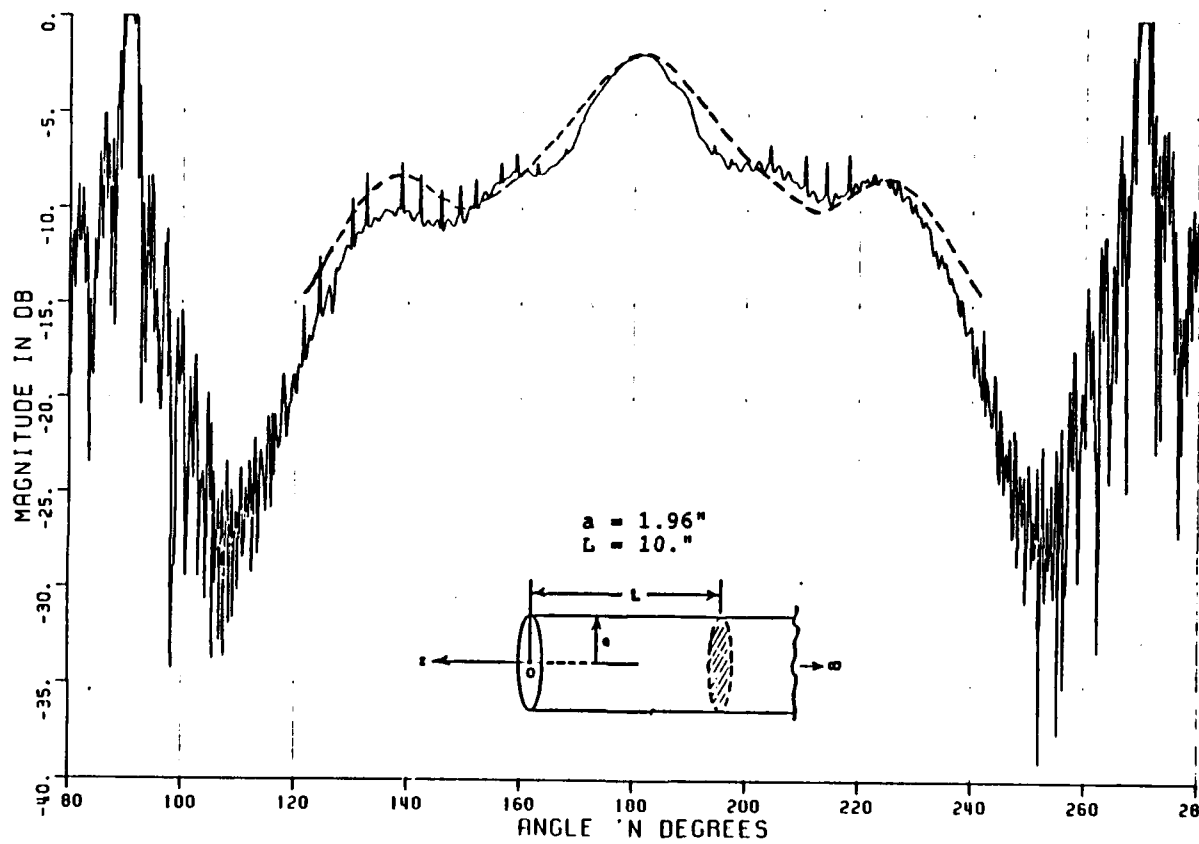
(b)

Figure 50. Continued.



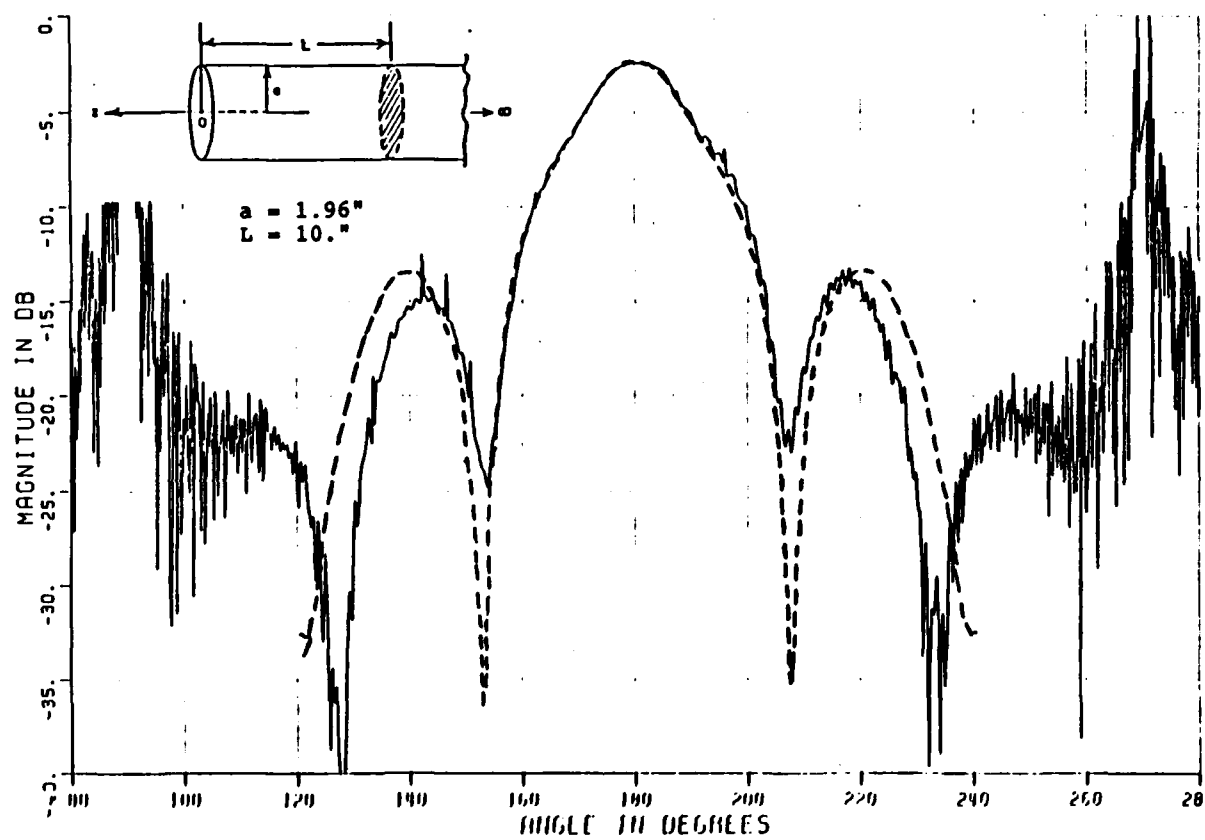
(c)

Figure 50. Continued.



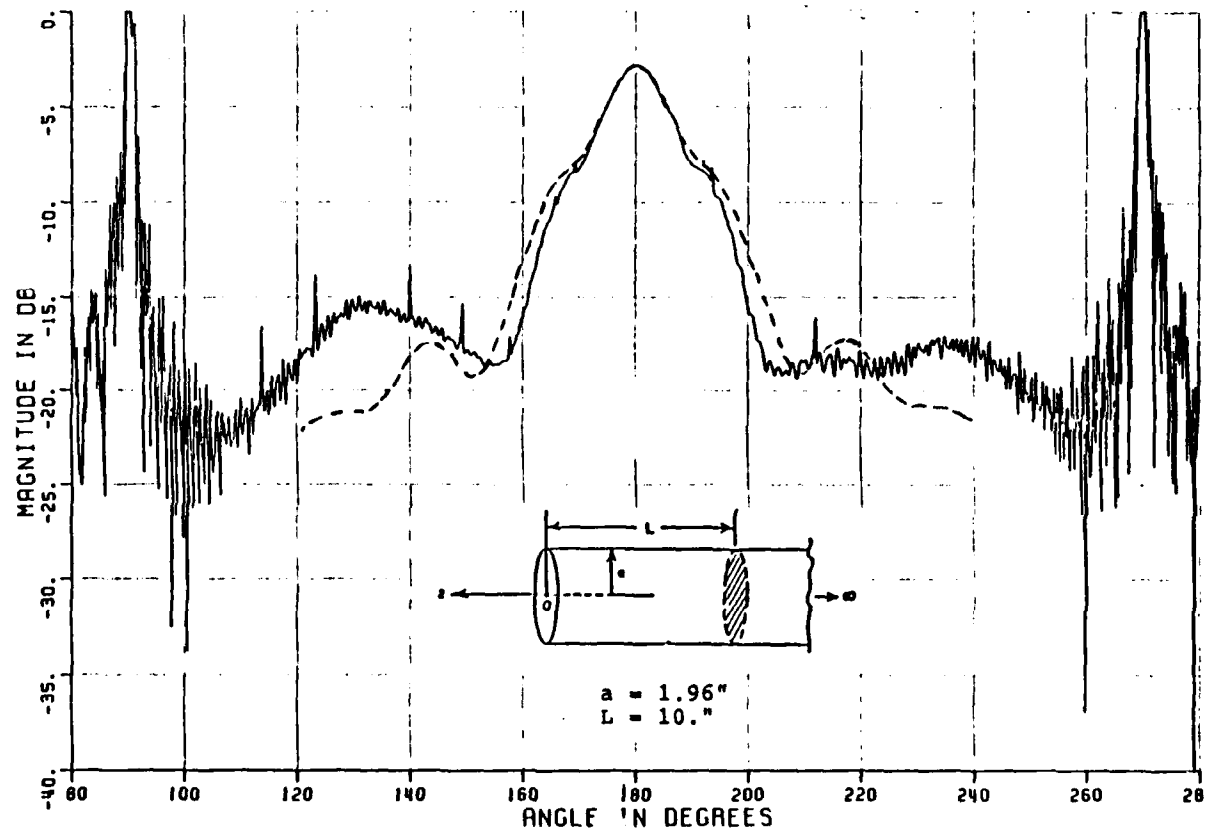
(a)

Figure 51. Comparisons of calculated and measured horizontal polarization backscattering patterns at (a) 9 GHz, (b) 10 GHz, and (c) 11 GHz.



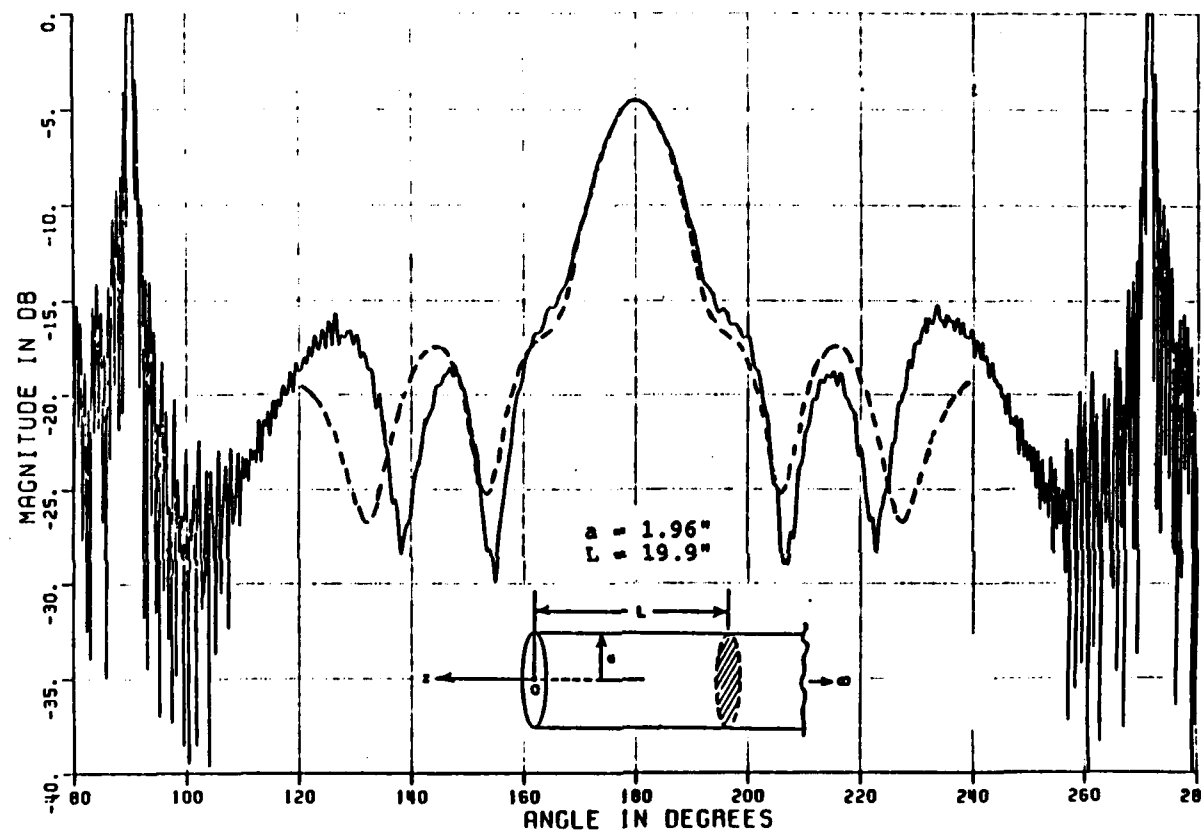
(b)

Figure 51. Continued.



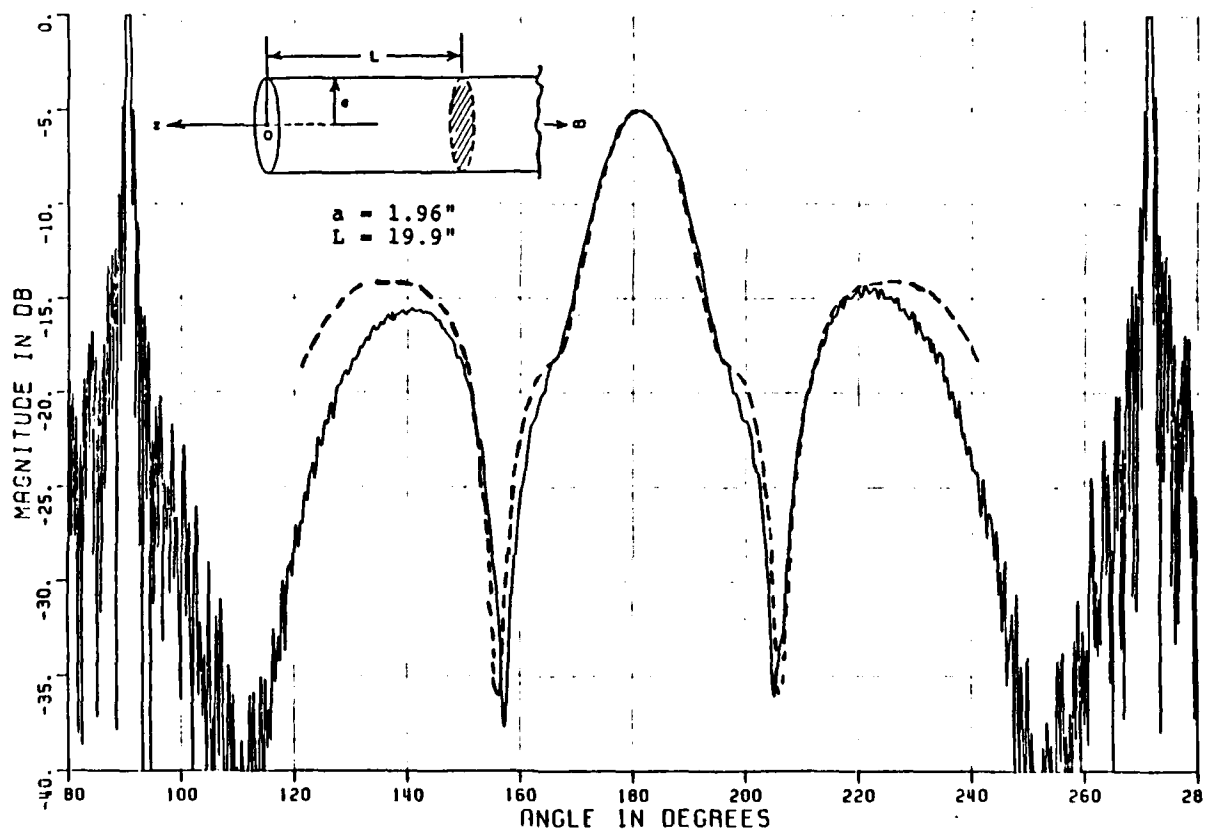
(c)

Figure 51. Continued.



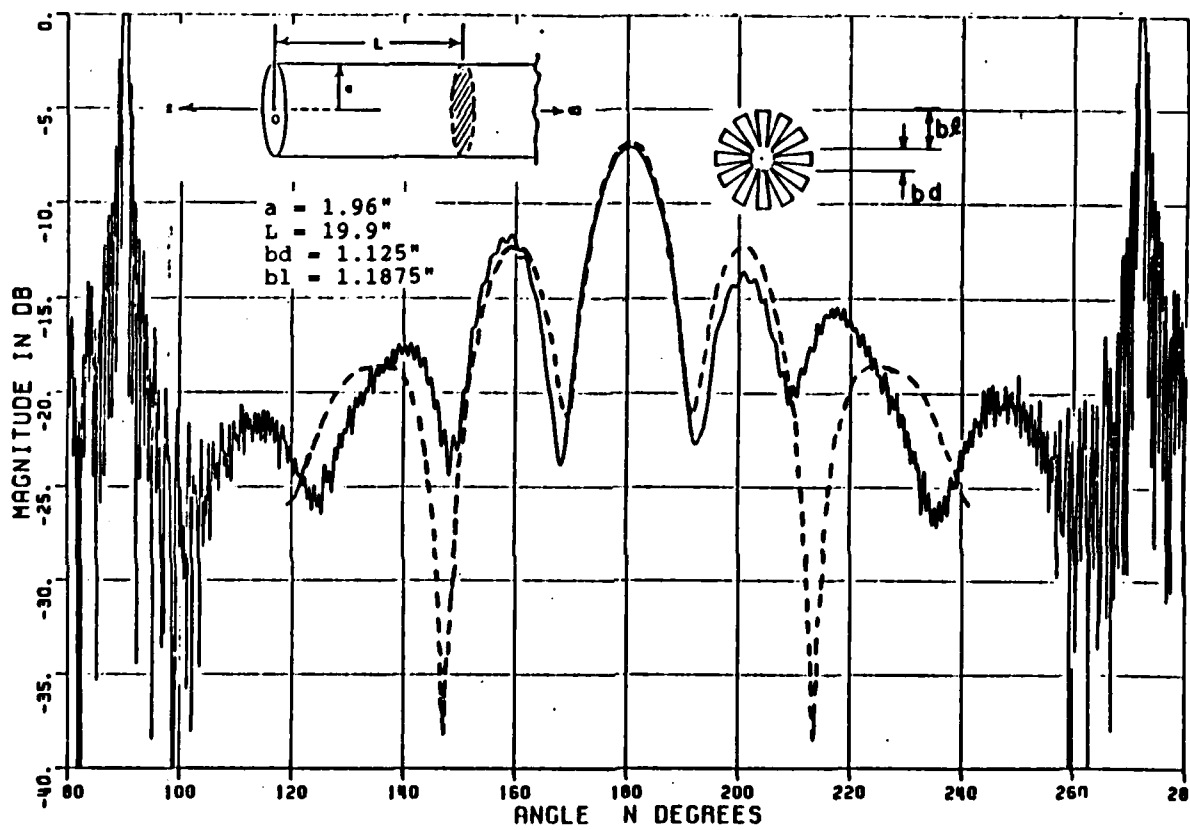
(a)

Figure 52. Comparisons of calculated and measured horizontal polarization backscattering patterns at (a) 10 GHz, (b) 10.2 GHz.



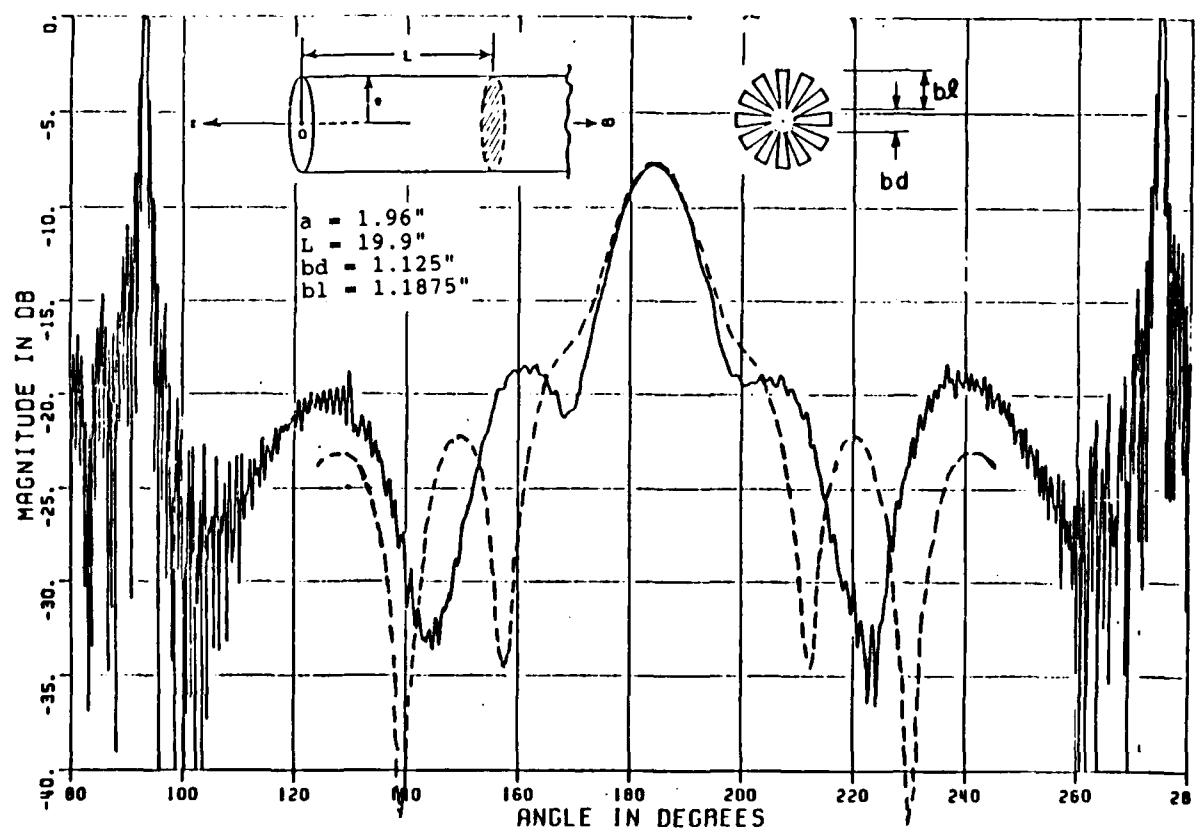
(b)

Figure 52. Continued.



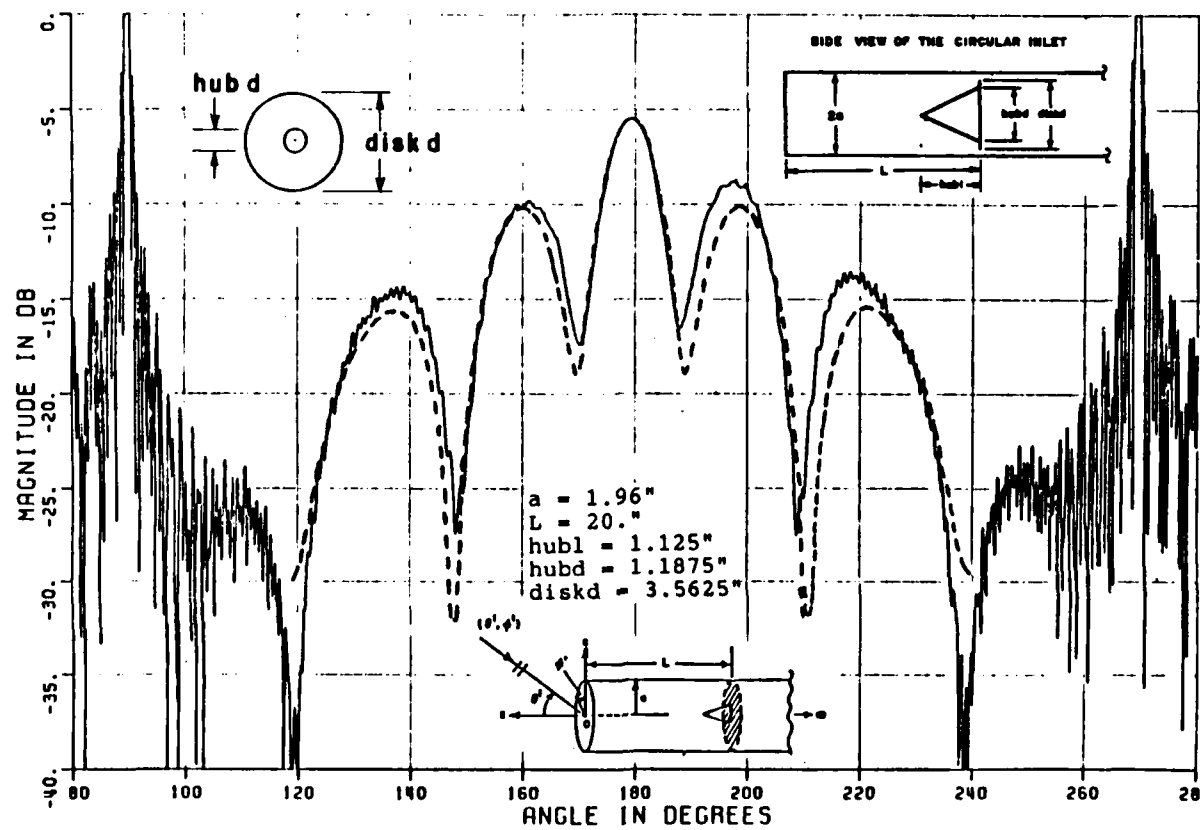
(a)

Figure 53. Comparison of calculated and measured backscattering patterns at 10 GHz (a) vertical polarization, (b) horizontal polarization.



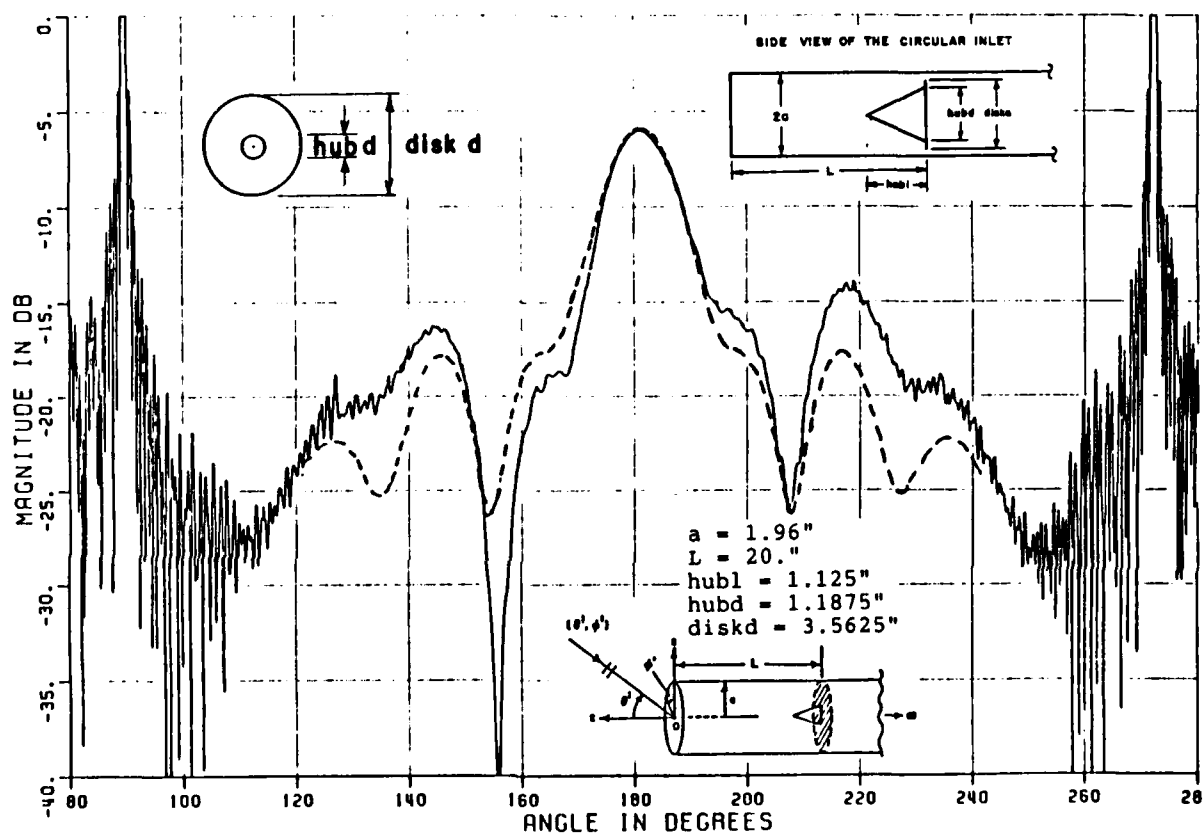
(b)

Figure 53. Continued.



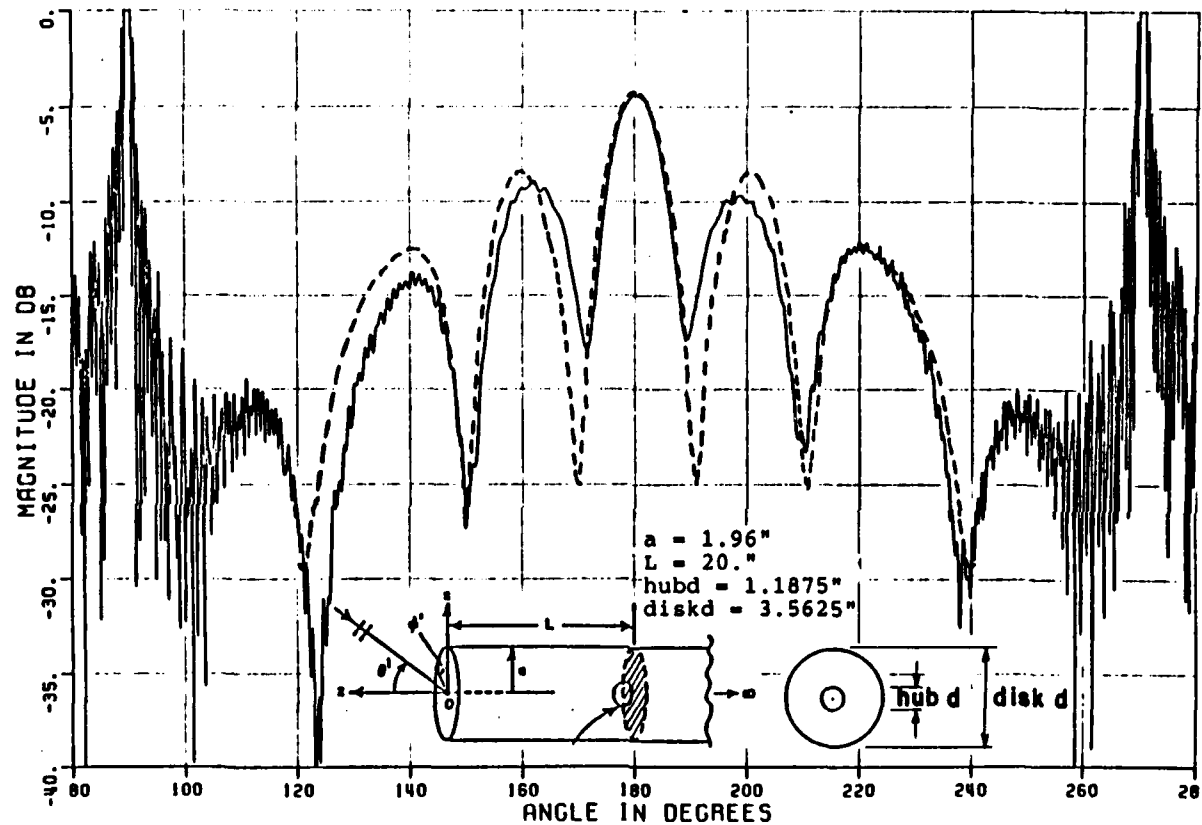
(a)

Figure 54. Comparison of calculated and measured backscattering patterns at 10 GHz, (a) vertical polarization, (b) horizontal polarization.



(b)

Figure 54. Continued.



(a)

Figure 55. Comparison of calculated and measured backscattering patterns at 10 GHz. (a) vertical polarization, (b) horizontal polarization.

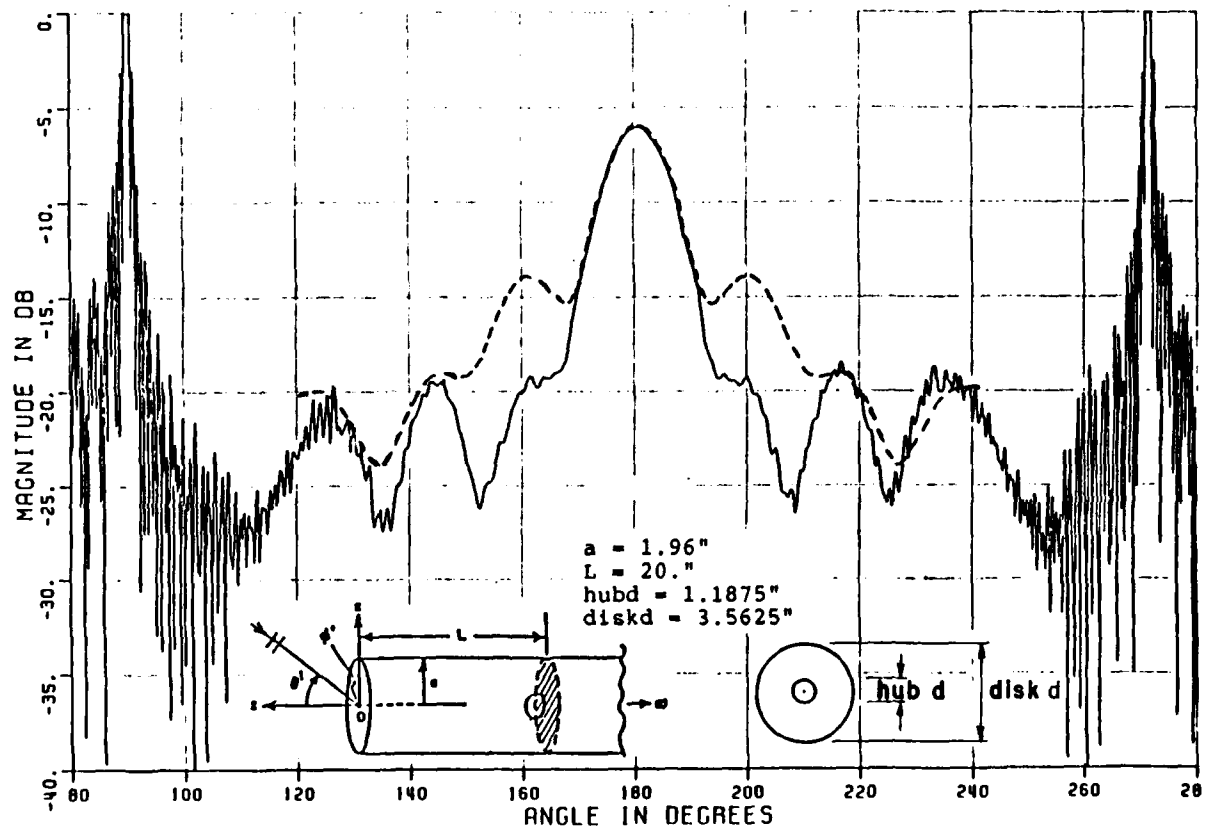
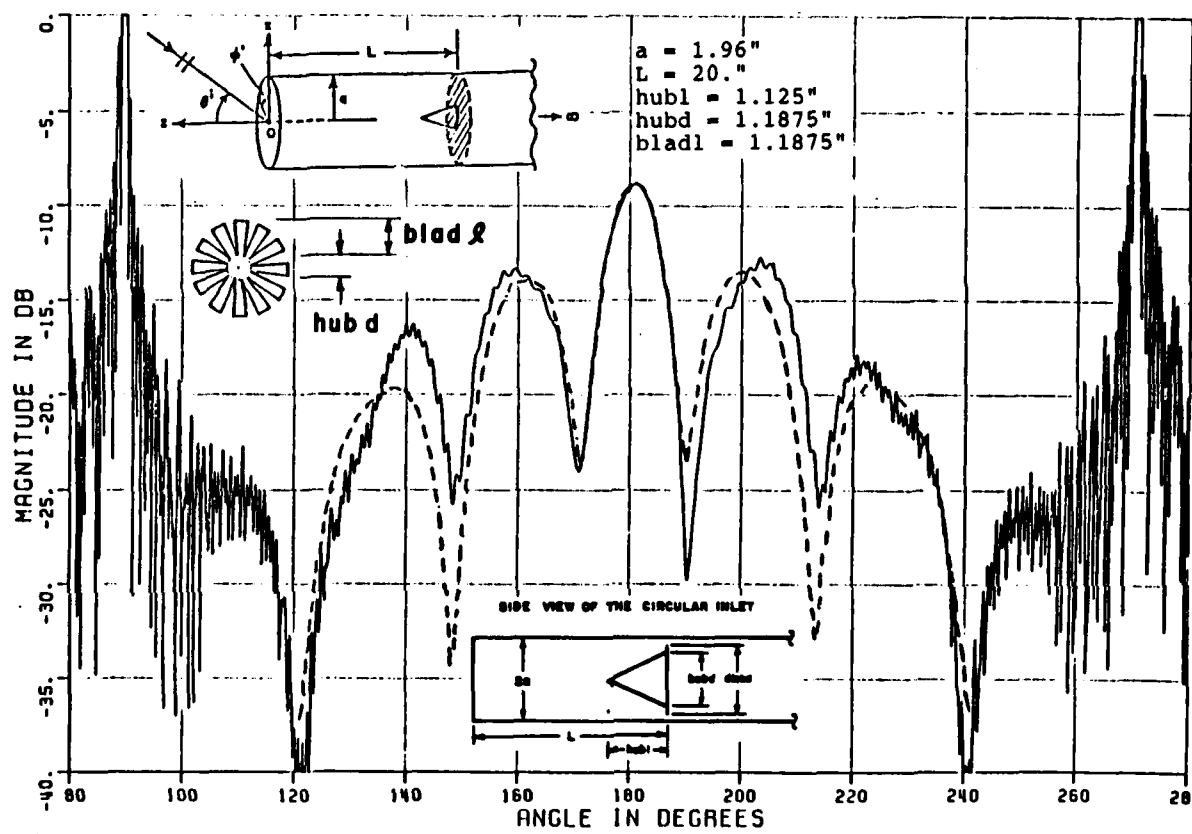
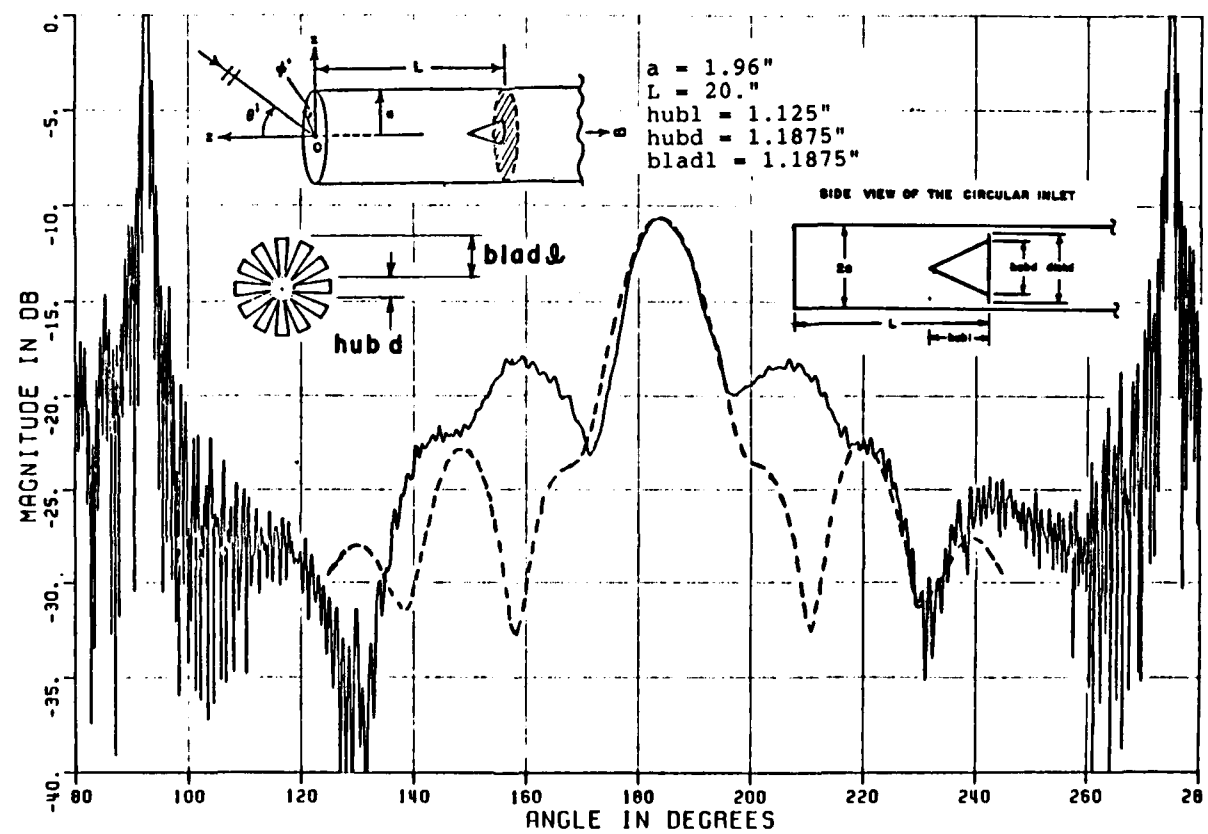


Figure 55. Continued.



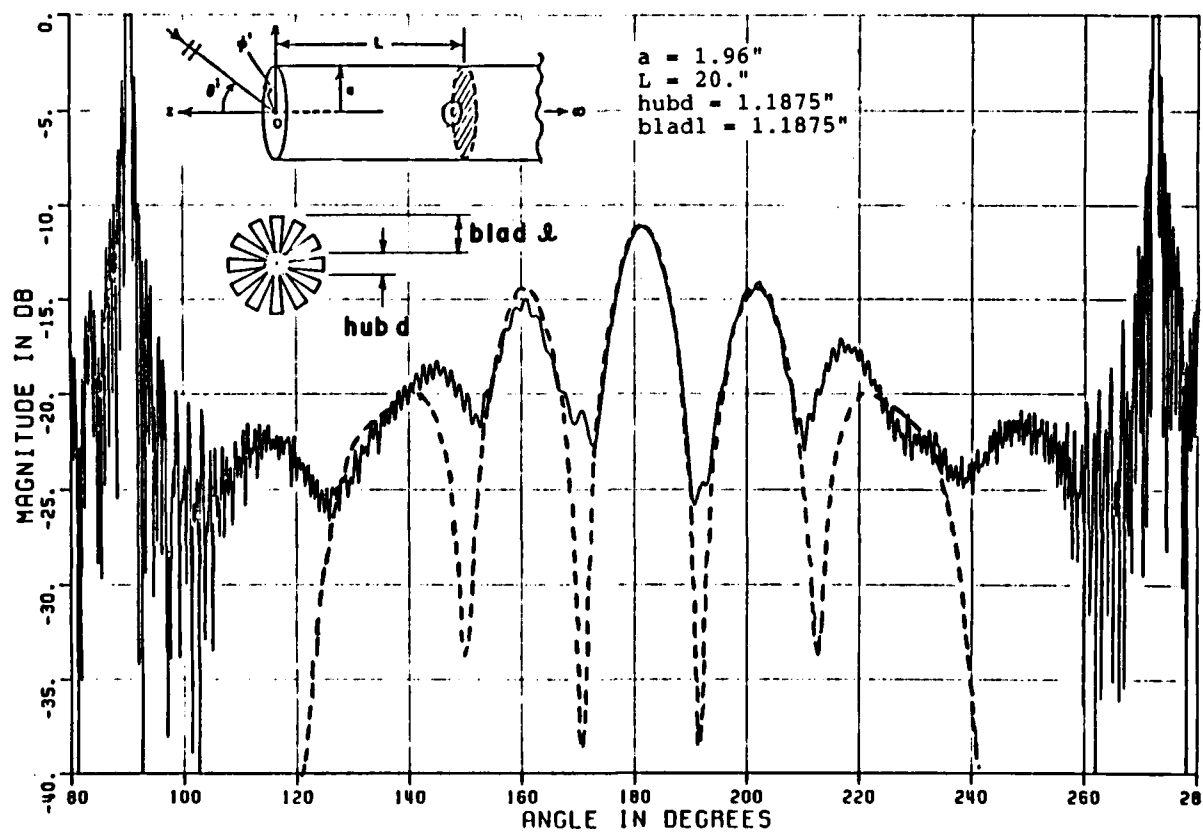
(a)

Figure 56. Comparisons of calculated and measured backscattering patterns at 10 GHz. (a) vertical polarization, (b) horizontal polarization.



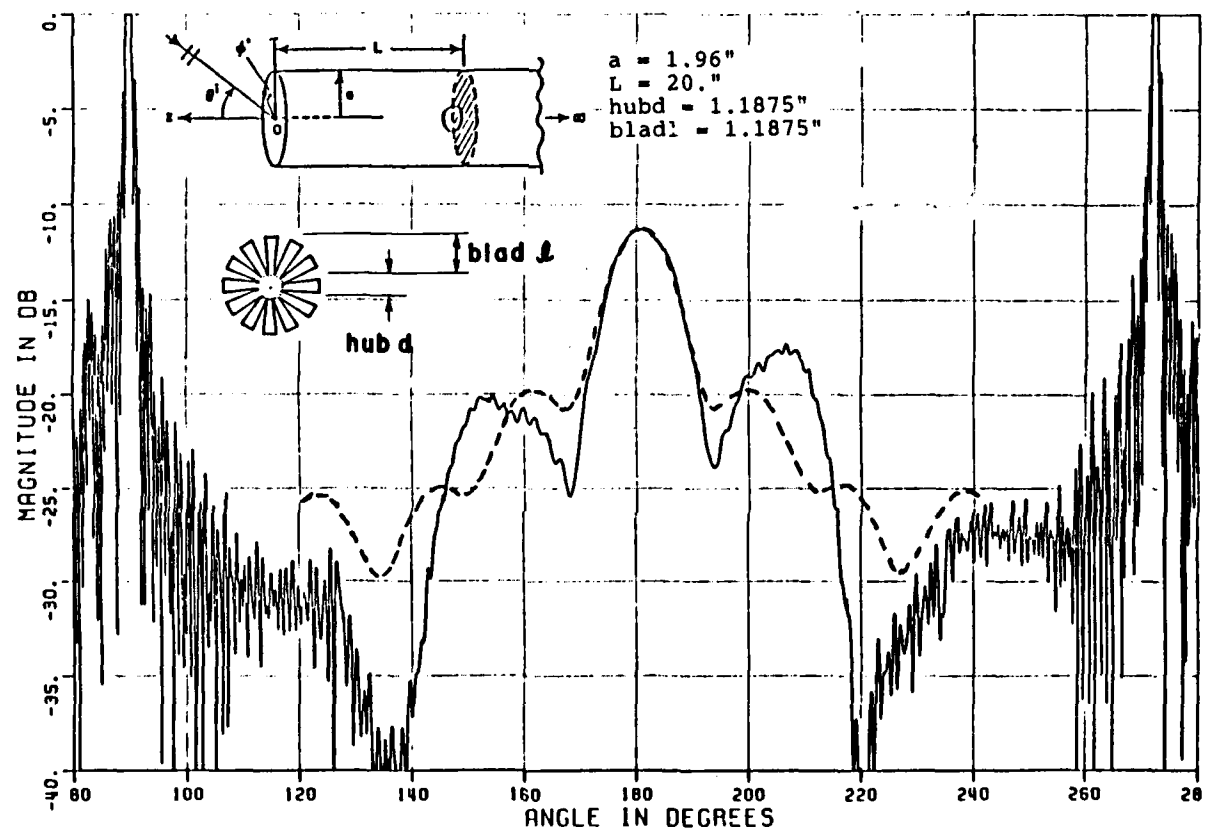
(b)

Figure 56. Continued.



(a)

Figure 57. Comparisons of calculated and measured backscattering patterns at 10 GHz. (a) vertical polarization, (b) horizontal polarization.



(b)

Figure 57. Continued.

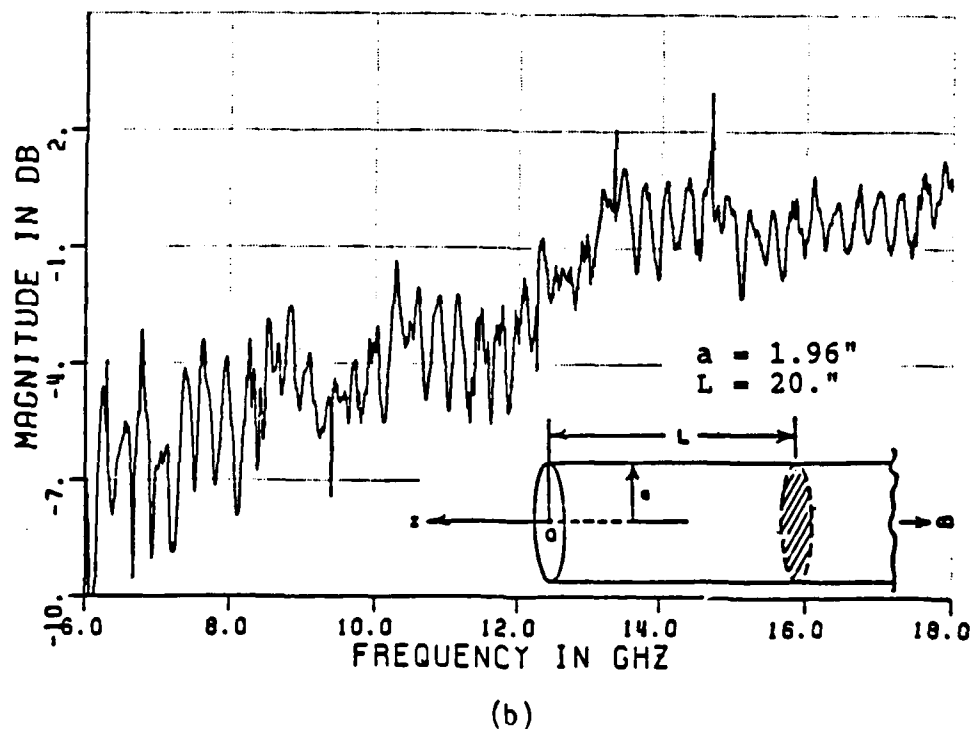
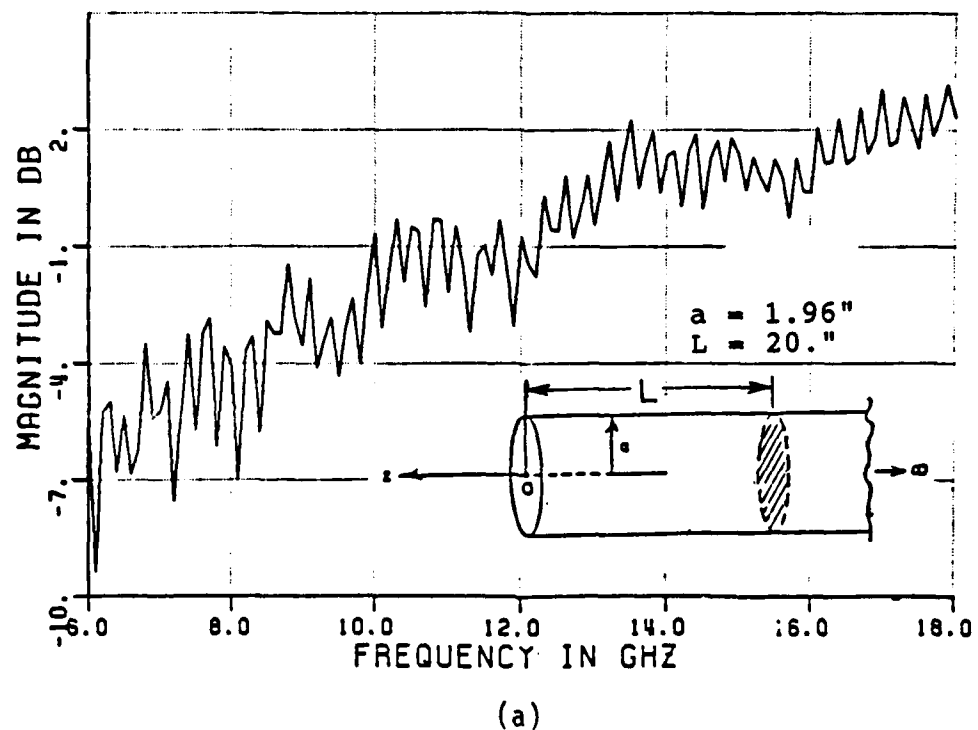
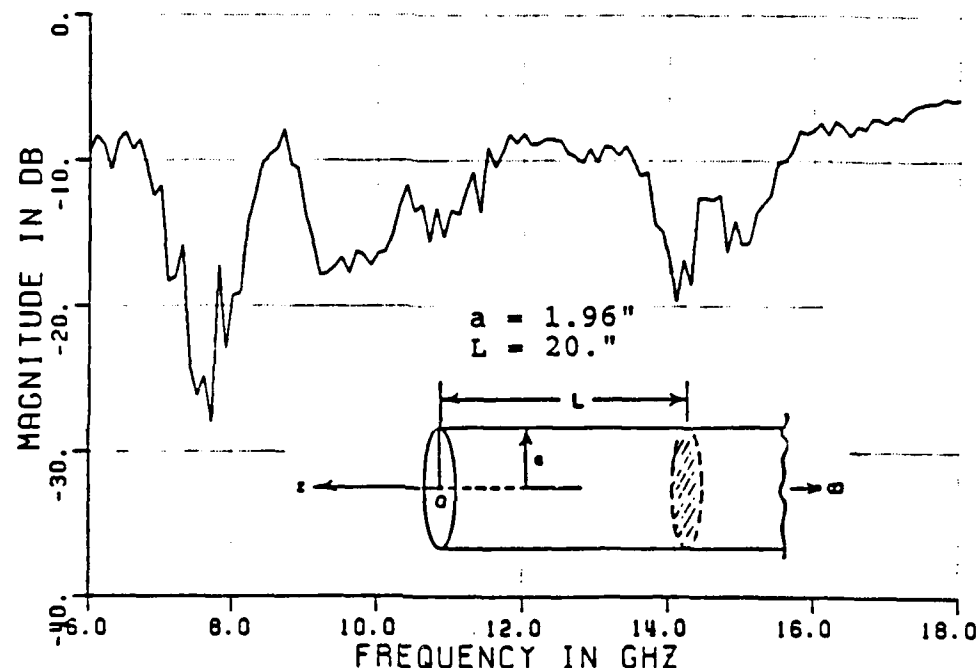
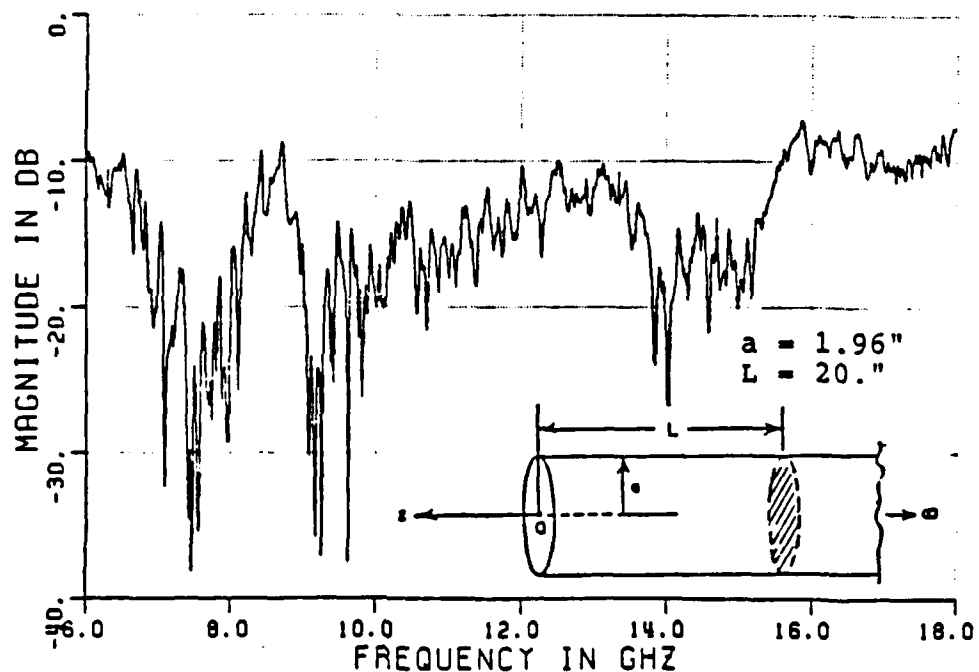


Figure 58. Horizontal polarization backscattering frequency scans with  $\theta^1=0$ . (a) calculated, (b) measured.

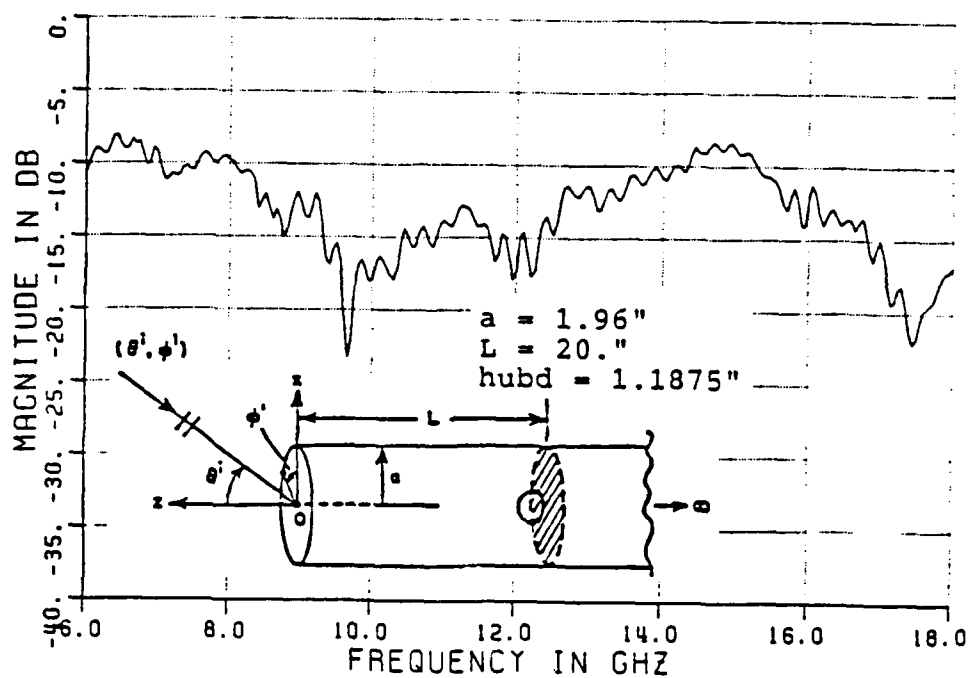


(a)

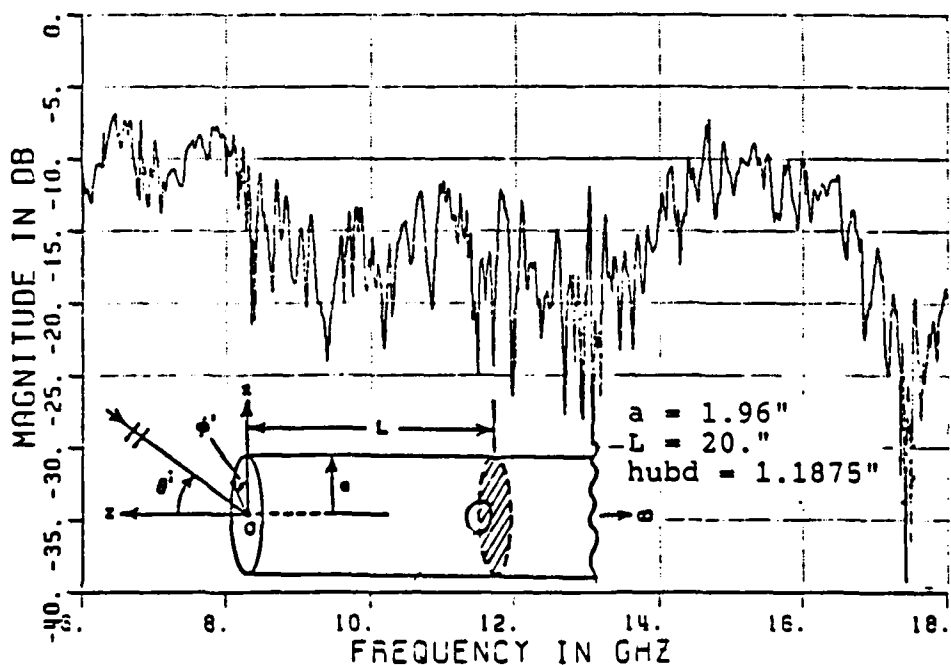


(b)

Figure 59. Horizontal polarization backscattering frequency scans with  $\theta_1 = 30^\circ$ . (a) calculated, (b) measured.

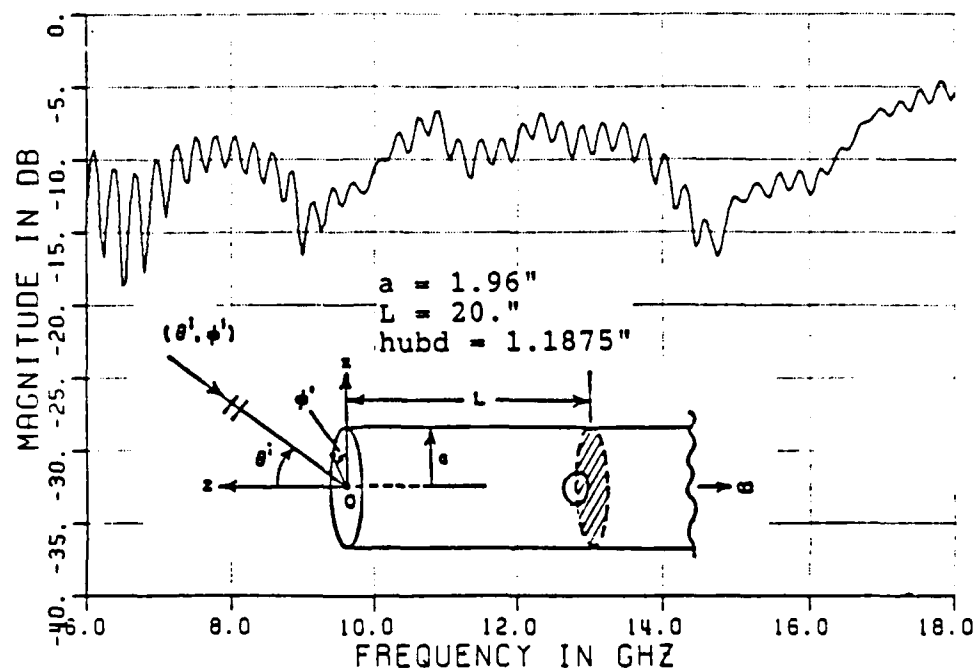


(a)

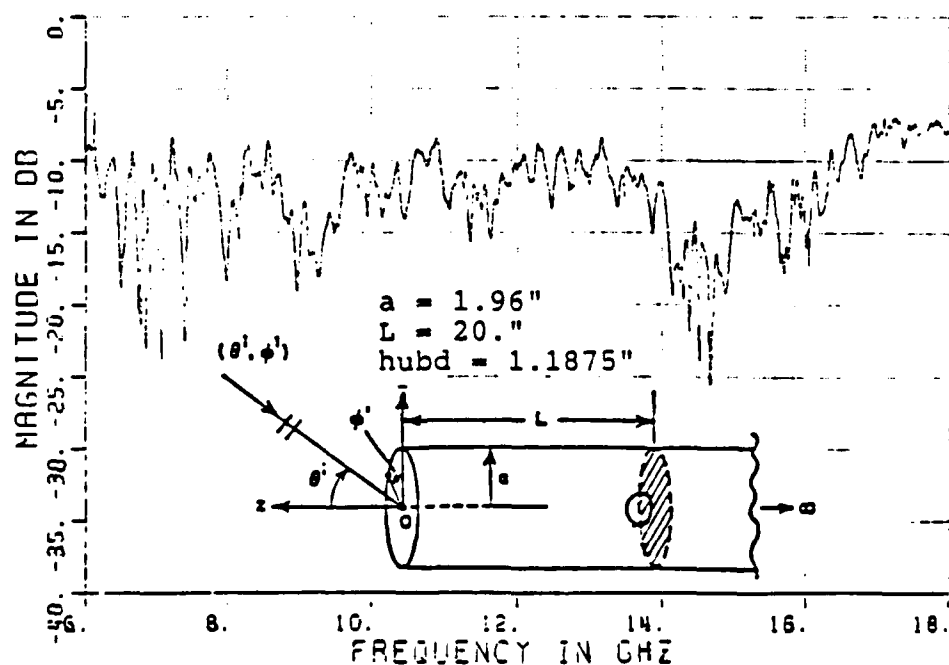


(b)

Figure 60. Horizontal polarization backscattering frequency scans with  $\theta^i = 15^\circ$ . (a) calculated, (b) measured.



(a)



(b)

Figure 61. Vertical polarization backscattering frequency scans with  $\theta^i = 15^\circ$ . (a) calculated, (b) measured.

An interesting observation as a consequence of using the P.O. approximation in determining the modal reflection coefficients from a conical hub termination in a circular inlet is depicted in Figure 62. As shown in the figure, an incident mode with a modal ray angle  $\beta$  is converted by the conical hub termination into reflected modes which are strong if their modal ray angles are close to  $\pi-2\alpha-\beta$  or  $\pi-2\alpha+\beta$ . The ability to convert an incident mode into several reflected modes can have a drastic effect on the backscattering return when the terminal position is changed. An example is shown in Figure 63, which compares calculated backscattering returns of a circular inlet with a conical hub termination at different positions. A simple explanation for the large change in the backscattering return for the axial incidence ( $\theta=0$ ) case is as follows. A strong  $TE_{11}$  mode is coupled through the open end into the circular inlet. Subsequently, it is converted by the conical hub termination into reflected  $TE_{11}$ ,  $TE_{12}$  and  $TE_{13}$  modes. The three modes radiate approximately equally in the axial direction. Thus when changing the terminal position, although the relative strengths of the three modes remain virtually unchanged, their different phase combinations can result in significant changes in the backscattering returns as shown in Figure 63. The same argument can also be applied to the non-axial incidence case, although the situation is more complicated there.

If the base length ( $hd$ ) of the conical hub termination in Figure 63 is reduced, but with everything else remaining the same, the backscattering return then becomes less sensitive to the change in the

terminal position of the conical hub, especially in the axial direction as shown in Figure 64. This is because for the case of axial incidence, only the  $TE_{11}$  mode plays an important role in contributing to the backscattering in contrast to the previous case of Figure 63 wherein three modes contributed equally to the on-axis backscattering return.

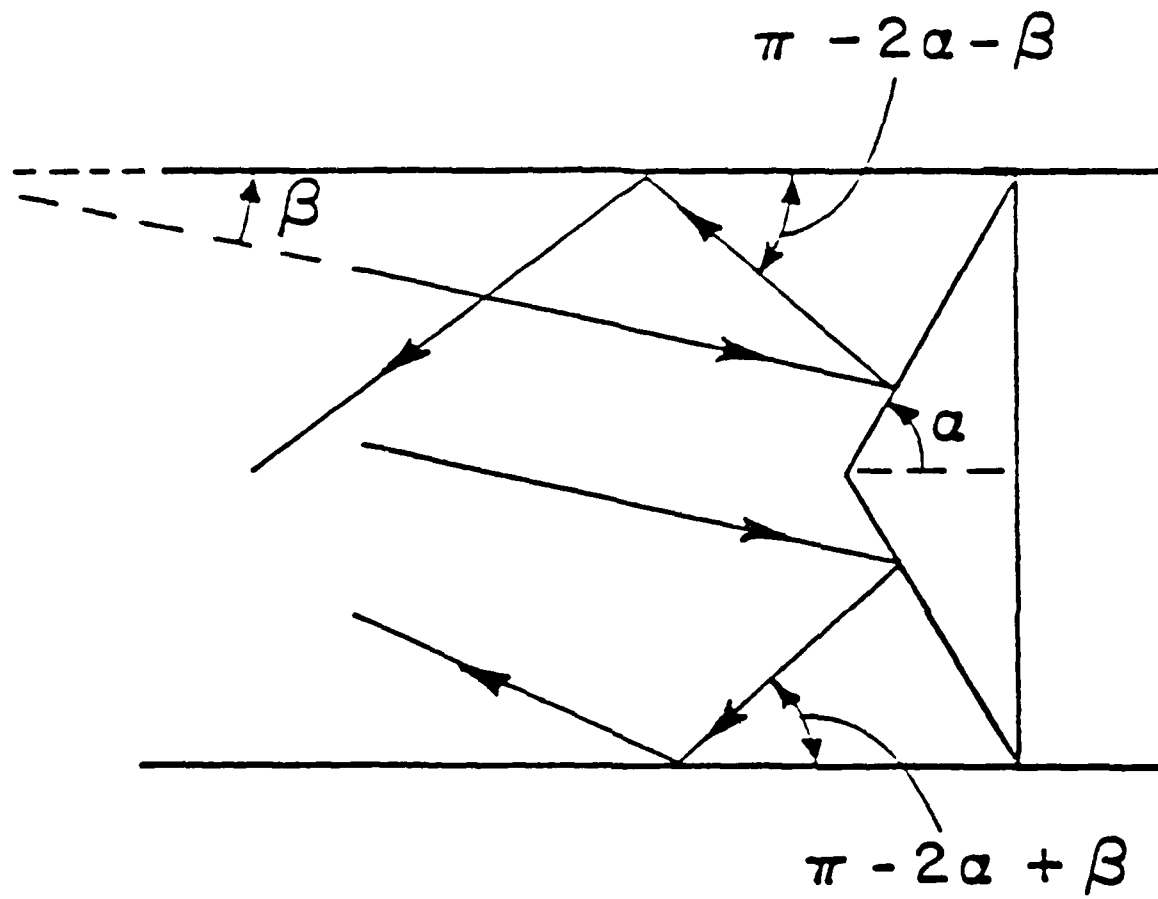
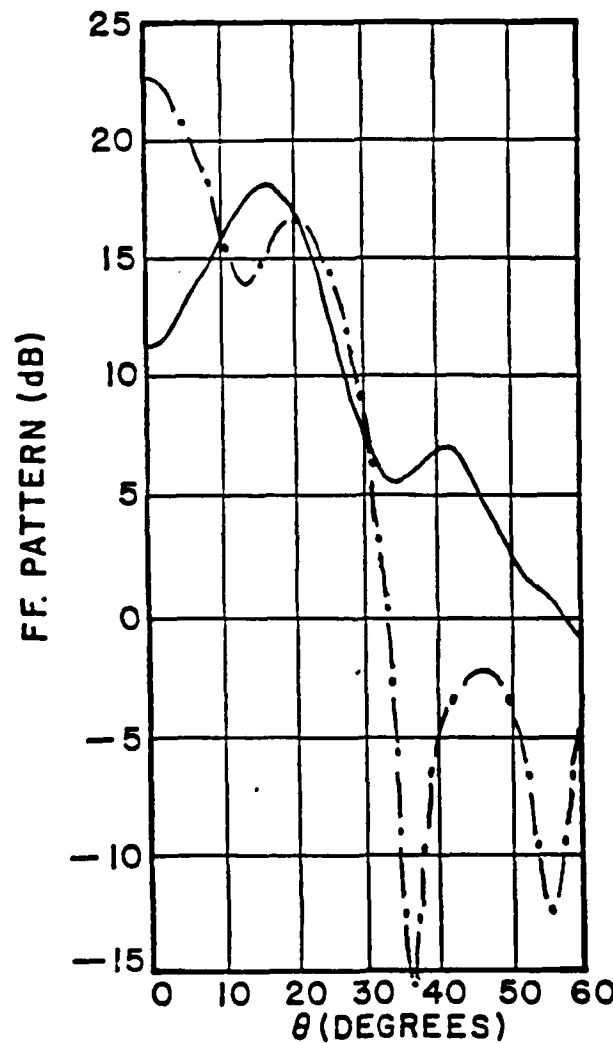
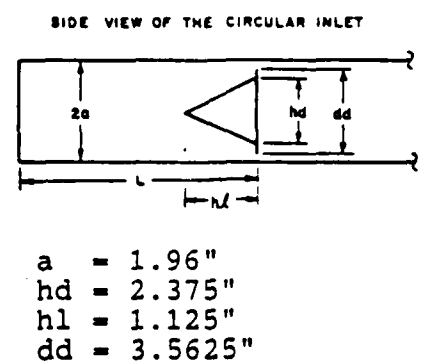


Figure 62. Incident and reflected modal rays associated with a conical hub termination.

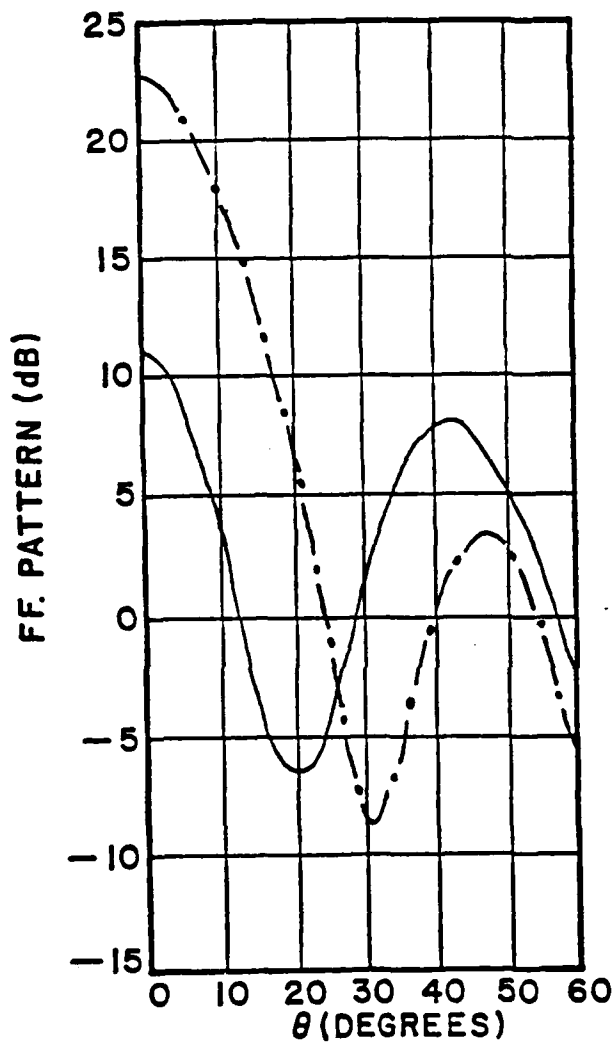


(a) vertical polarization

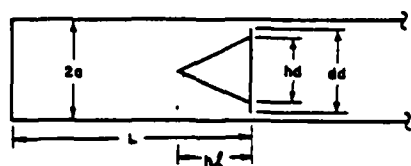
Figure 63. Comparison of the backscattering patterns for a circular waveguide with conical hub terminations at different terminal positions.



$— \quad L = 18"$   
 $— \cdot — \quad L = 20"$



SIDE VIEW OF THE CIRCULAR INLET



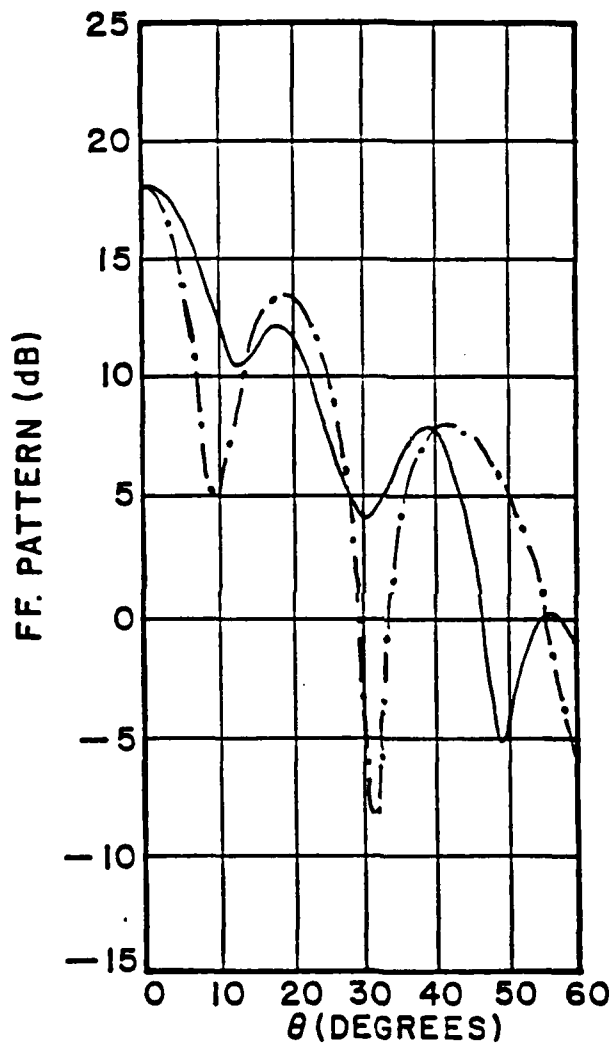
$a = 1.96"$   
 $hd = 2.375"$   
 $h1 = 1.125"$   
 $dd = 3.5625"$

— termination  
at 19"

— · — termination  
at 20"

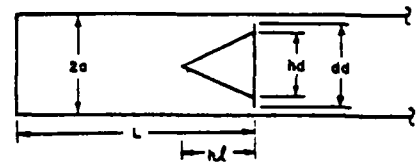
(b) horizontal polarization

Figure 63. Continued.



$a = 1.96"$   
 $hd = 1.1875"$   
 $hl = 1.125"$   
 $dd = 3.5625"$

SIDE VIEW OF THE CIRCULAR INLET

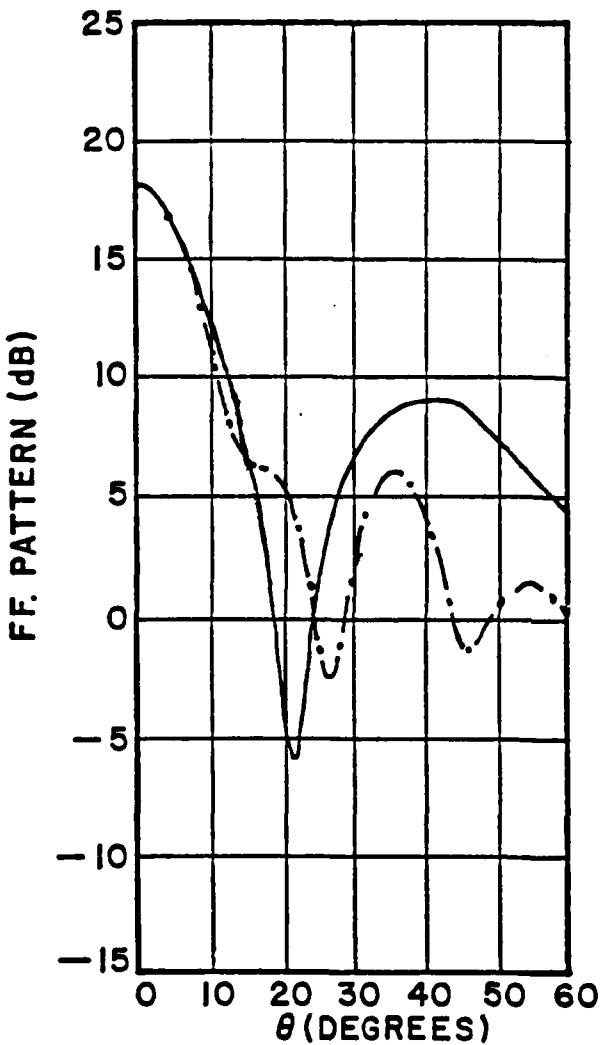


termination  
at 19"

termination  
at 20"

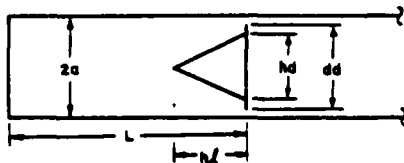
(a) vertical polarization

Figure 64. Comparison of the backscattering patterns for a circular waveguide with conical hub termination at different terminal positions.



$a = 1.96"$   
 $hd = 1.1875"$   
 $hl = 1.125"$   
 $dd = 3.5625"$

SIDE VIEW OF THE CIRCULAR INLET



— termination  
at 19"

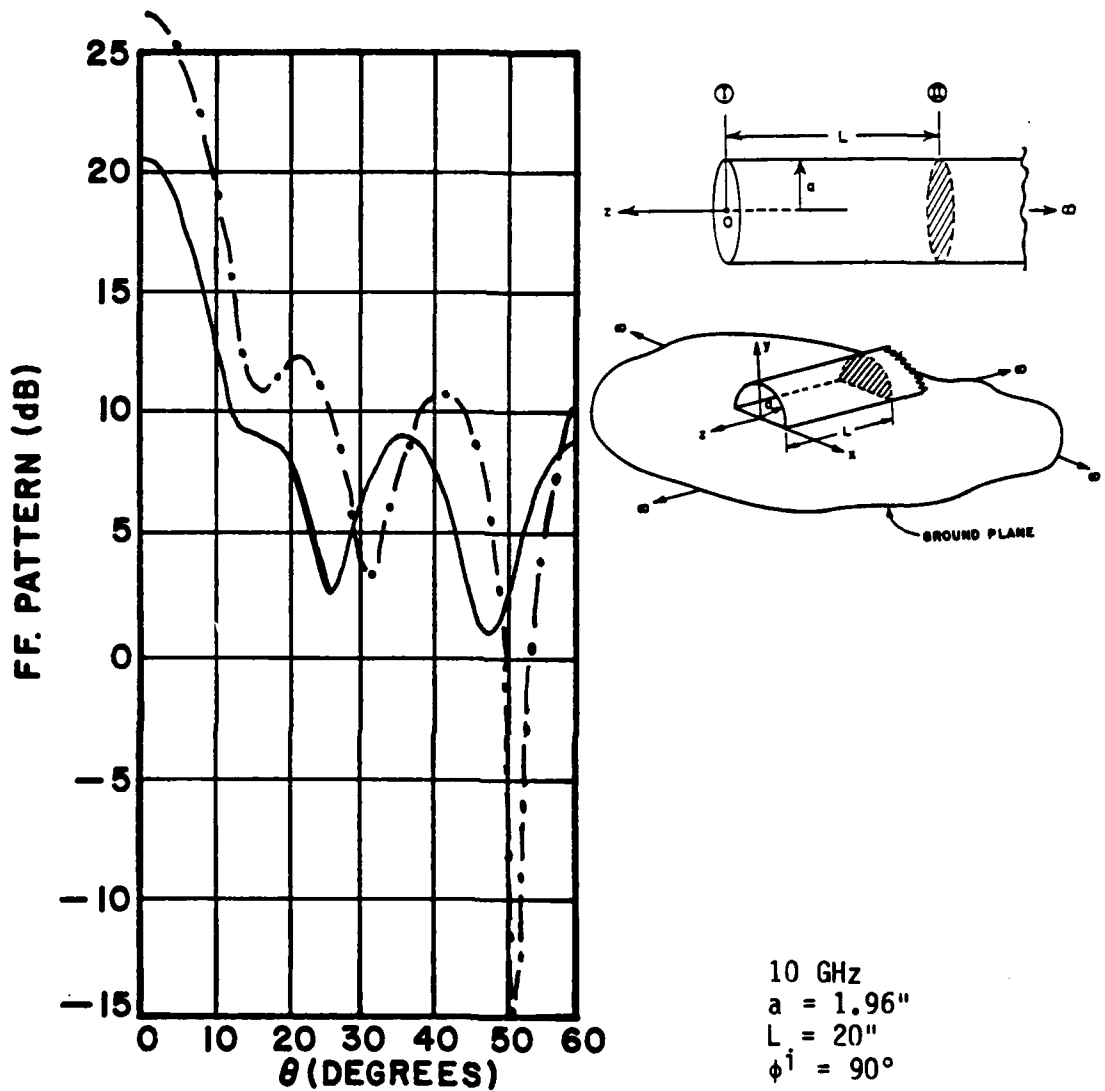
—·— termination  
at 20"

(b) horizontal polarization

Figure 64. Continued.

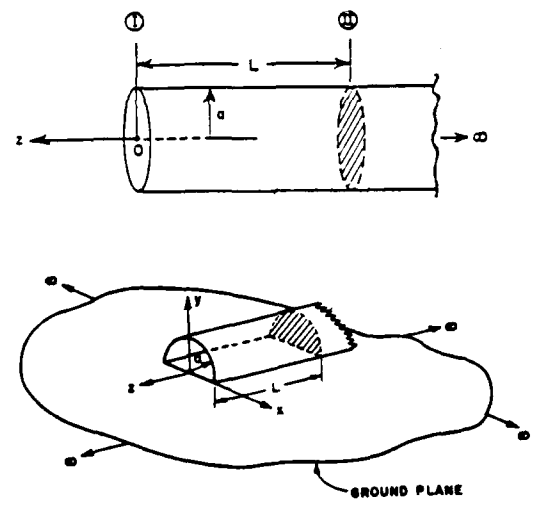
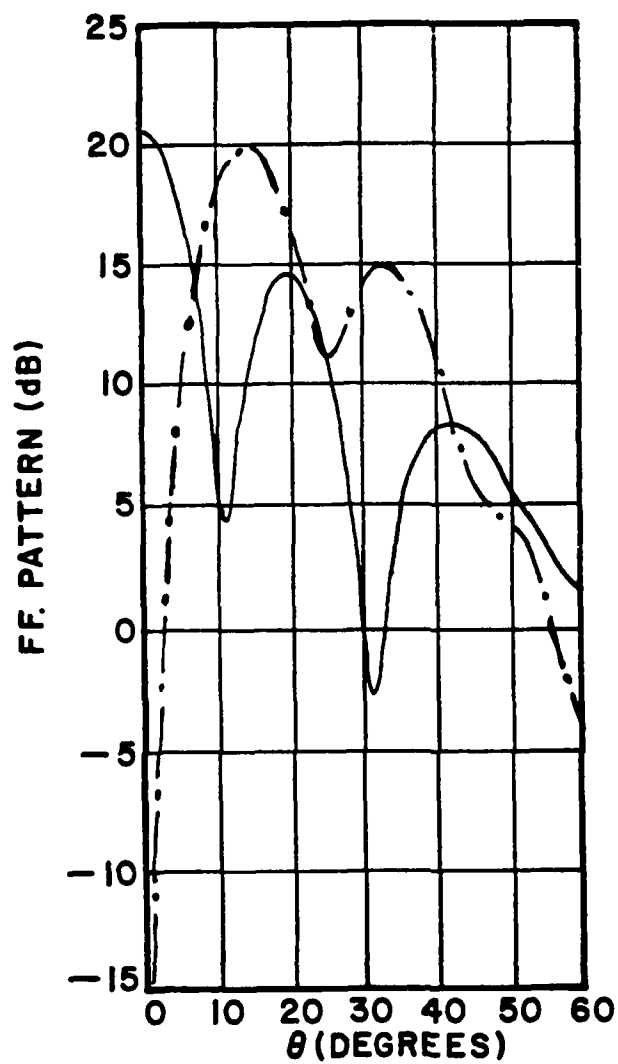
The method developed in the previous sections can also be applied to evaluating fields scattered by open-ended rectangular and semi-circular inlets mounted on a ground plane. This problem can be simplified using image theory. Thus, this problem simply reduces to that considered before; i.e., to evaluate the fields scattered by open-ended rectangular and circular inlets which are illuminated by two sources corresponding to the original one and its image.

Figure 65 illustrates a comparison of the calculated backscattering results from an open-ended circular waveguide and an open-ended semi-circular one mounted on a ground plane, both of which are terminated in the interior by a planar short circuit. For axial incidence, the existence of the ground plane effectively increases the backscattering return by 6 dB if the electric field is polarized perpendicular to the ground plane, and it reduces the backscattering return to zero if the electric field is polarized parallel to the ground plane, as shown in Figure 65. Finally, a comparison of the calculated near zone bistatic scattering from an open-ended rectangular waveguide and another one of half the size mounted on a ground plane, both of which possess a short circuit termination inside, is shown in Figure 66. It is interesting to note that for the  $\hat{\phi}$  polarization case (Figure 66b), the direction of incidence and the size of the waveguide are chosen in such a way that the rim scattering of the incident plane wave and its image by the rectangular waveguide mounted on the ground plane exactly cancel each other. Thus, for this case, the entire scattering (dashed curve) is due only to the reradiation of the field reflected back by the short circuit termination. On the other hand, such a cancellation of the rim



(a)  $\hat{\theta}$  polarization

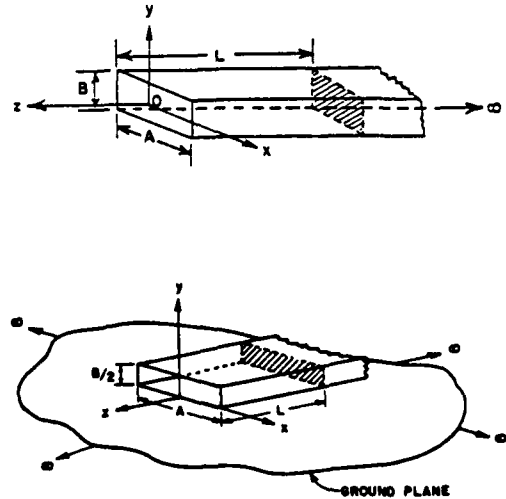
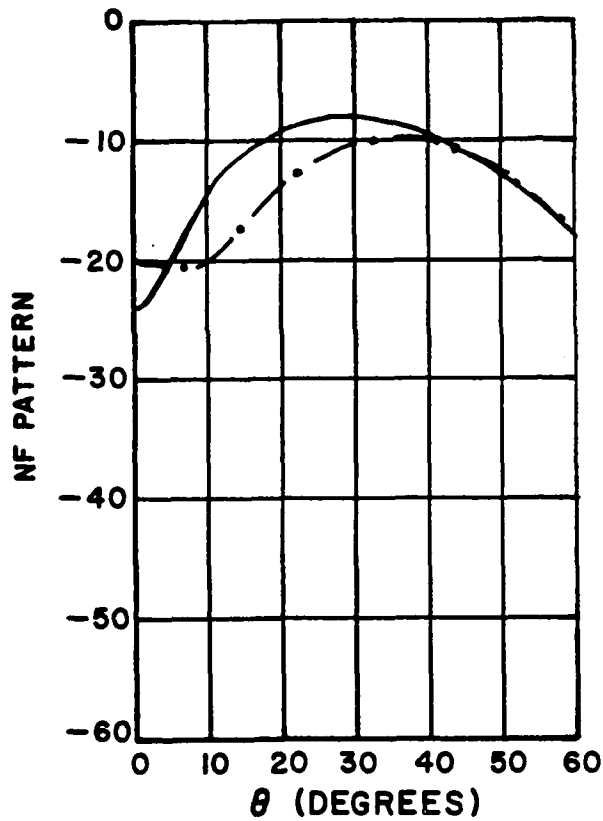
Figure 65. Comparison of backscattering returns from an open-ended circular waveguide (solid curve) and an open-ended semi-circular waveguide mounted on a ground plane (broken curve).



10 GHz  
 $a = 1.96''$   
 $L = 20''$   
 $\phi^i = 90^\circ$

(b)  $\hat{\phi}$  polarization

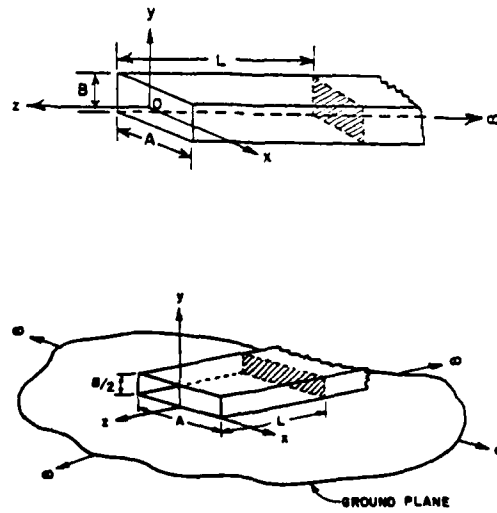
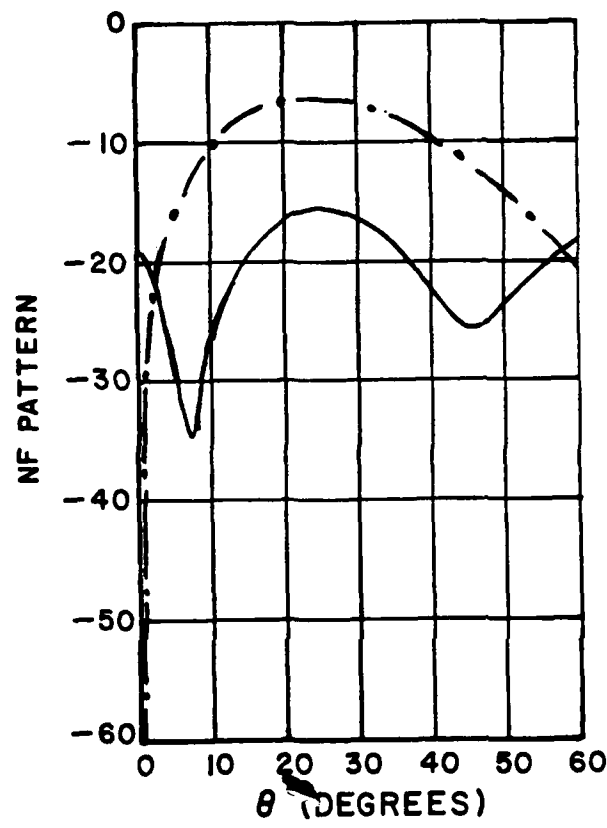
Figure 65. Continued.



$$\begin{aligned}
 A &= 1\lambda \\
 B &= 2\lambda \\
 C &= 10\lambda \\
 \theta^1 &= 30^\circ \\
 \phi^1 &= 90^\circ
 \end{aligned}$$

(a)  $\hat{\theta}$  polarization

Figure 66. Comparison of near zone bistatic scattering from an open-ended rectangular waveguide (solid curve) and another one of half the vertical dimension mounted on a ground plane (broken curve) for observation at ( $r=4\lambda, \phi=90^\circ$ ).



$$\begin{aligned}
 A &= 1\lambda \\
 B &= 2\lambda \\
 C &= 10\lambda \\
 \theta_i &= 30^\circ \\
 \phi_i &= 90^\circ
 \end{aligned}$$

(b)  $\hat{\phi}$  polarization

Figure 66. Continued.

scattering by the image may not occur for the  $\hat{\theta}$  polarization, because the main contribution in that case comes from the vertical plates.

## V. CONCLUSION

The work described in this report provides relatively efficient solutions which are based on a combination of high frequency and modal techniques for the problems of near and far zone bistatic scattering of EM plane waves incident on open ended semi-infinite, perfectly conducting circular and rectangular inlet configurations with an interior termination. The interior terminations could be either a planar perfectly conducting surface or a planar impedance (or dielectric) surface termination. It is noted that when the impedance vanishes then the impedance surface termination reduces to the perfectly-conducting case.

Some additional simple interior terminations have also been considered in this work for the case of the circular inlet geometry; they are:

- a) a conducting disk-blade termination
- b) a conducting conical or hemi-spherical hub placed on a conducting disk, or on a conducting disk-blade structure.

Moreover, the related problems of the EM scattering by an open ended, semi-infinite perfectly conducting semi-circular and rectangular inlets on a perfectly conducting ground plane have been analyzed directly via an application of image theory in combination with the solutions which have been obtained for the circular and rectangular inlets without the ground plane.

It is seen that the RCS of the above structures are quite sensitive to frequency. Also, the scattering patterns of the horizontally polarized wave are very sensitive to small changes in structure. The calculations for the far zone EM backscattering case which have been performed in this work are compared with corresponding measurements. The overall agreement between the calculation and measurement is quite good. No measurements have been performed on this contract for the case of the near zone bistatic scattering by such inlets. In the future, it would be worthwhile to make near and far zone measurements of scattering by somewhat more improved experimental models than those used presently. Also, it would be worth extending the research effort to find ways to analyze the more complex problem of scattering by non-uniform inlet geometries in a relatively efficient manner.

## APPENDIX I

### WAVEGUIDE EXCITATION PROBLEM

Let a source  $\bar{S}$  be located inside waveguide as shown in Figure A.1.  $\bar{S}$  can be an electric current source  $\bar{J}$  or a magnetic current source  $\bar{M}$ , which generates  $\bar{E}^\pm, \bar{H}^\pm$ . Thus,

$$\bar{E}^\pm, \bar{H}^\pm = \sum_p A_p^\pm (\bar{E}_p^\pm, \bar{H}_p^\pm) \quad (A.1)$$

are the fields generated by  $\bar{S}$  in the  $\pm\hat{z}$  directions. In this summation  $p$  is the compact summation index representing the double summation over mode indices "n" and "m". It is of interest to find  $(\bar{E}^\pm; \bar{H}^\pm)$ . Here,  $\bar{E}^\pm$  will be determined via an application of the reciprocity theorem as in [13].

The modal fields can be decomposed into transverse and axial components as follows:

$$\bar{H}_p^\pm = A_p^\pm (\pm \bar{H}_{pt} + \bar{H}_{pz}) e^{\mp j\beta_p z} \quad (A.2a)$$

$$\bar{E}_p^\pm = A_p^\pm (E_{pt} \pm E_{pz}) e^{\mp j\beta_p z} \quad (A.2b)$$

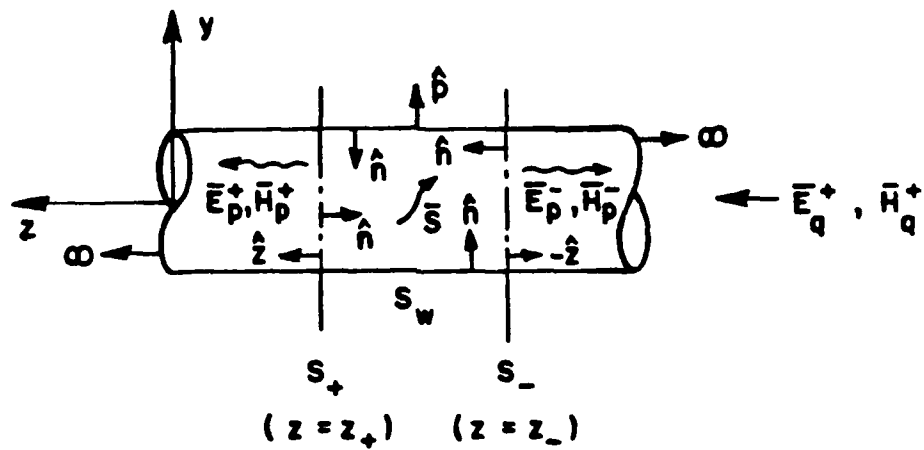


Figure A.1. Waveguide geometry.

where for  $TE_{nm}$  modes;

$$\bar{H}_{pt} = \bar{h}_{nm}^i ; \bar{H}_{pz} = \bar{h}_{z,nm}^i ; \bar{E}_{pt} = \bar{e}_{nm}^i \text{ and } \bar{E}_{pz} = 0$$

and for  $TM_{nm}$  modes;

$$\bar{H}_{pt} = \bar{h}_{nm}^i ; \bar{H}_{pz} = 0 ; \bar{E}_{pt} = \bar{e}_{nm}^i \text{ and } \bar{E}_{pz} = \bar{e}_{z,nm}^i .$$

Case (i):

It is of interest to find the strength of the mode  $\bar{E}_q^-$ ,  $\bar{H}_q^-$  generated by  $\bar{S}$ . (Here,  $q$  is the compact index representing the mode indices "ij".)

From the reciprocity theorem:

$$-\iint_{S_+ + S_W} [\bar{E} \times \bar{H}_q^+ - \bar{E}_q^+ \times \bar{H}] \cdot \hat{n} \, ds = \begin{cases} \iint_V \bar{E}_q^+ \cdot \bar{J} \, dv & \text{for } \bar{S} = \bar{J} \\ -\iint_V \bar{H}_q^+ \cdot \bar{M} \, dv & \text{for } \bar{S} = \bar{M} \end{cases} \quad (A.3)$$

where  $\bar{E}, \bar{H} = \bar{E}^+, \bar{H}^+$  on  $S_+$  and  $\bar{E}, \bar{H} = \bar{E}^-, \bar{H}^-$  on  $S_-$ . Also,  $E_q \times \hat{n} \Big|_{S_W} = 0$  and  $E_p^+ \times \hat{n} \Big|_{S_W} = 0$ .

Thus, the above reciprocity relation simplifies to:

$$\begin{aligned} & \iint_{S_+} [\bar{E}^+ \times \bar{H}_q^+ - \bar{E}_q^+ \times \bar{H}^+] \cdot \hat{z} \, ds + \iint_{S_-} [\bar{E}^- \times \bar{H}_q^+ - \bar{E}_q^+ \times \bar{H}^-] \cdot (-\hat{z}) \, ds \\ &= \begin{cases} \iint_V \bar{E}_q^+ \cdot \bar{J} \, dv & \text{for } \bar{S} = \bar{J} \\ -\iint_V \bar{H}_q^+ \cdot \bar{M} \, dv & \text{for } \bar{S} = \bar{M} \end{cases} \quad . \end{aligned} \quad (A.4)$$

Substituting  $\bar{E}^+, \bar{H}^+$  and  $\bar{E}^-, \bar{H}^-$  from Equation (A.1) and using the orthogonality condition:

$$\iint_{S_\pm} [\bar{E}_p^\pm \times \bar{H}_q^\pm] \cdot \hat{n} \, ds = 0 \quad \text{for } q \neq p \quad (A.5)$$

one obtains a relationship in terms of only  $q^{\text{th}}$  mode (i.e.,  $p=q$  case)

$$\begin{aligned}
& \iint_{S_+} A_q^+ [(\bar{E}_{qt} + \bar{E}_{qz}) \times (\bar{H}_{qt} + \bar{H}_{qz}) e^{-j2\beta_q z} + \\
& \quad - (\bar{E}_{qt} + \bar{E}_{qz}) \times (\bar{H}_{qt} + \bar{H}_{qz}) e^{-j2\beta_q z}] \cdot \hat{z} \, ds \\
& - \iint_{S_-} A_q^- [(\bar{E}_{qt} - \bar{E}_{qz}) \times (\bar{H}_{qt} + \bar{H}_{qz}) \\
& \quad - (\bar{E}_{qt} + \bar{E}_{qz}) \times (-\bar{H}_{qt} + \bar{H}_{qz})] \cdot \hat{z} \, ds \\
& = \begin{cases} \iiint_V \bar{E}_q^+ \cdot \bar{J} \, dv & \text{for } \bar{S} = \bar{J} \\ -\iiint_V \bar{H}_q^+ \cdot \bar{M} \, dv & \text{for } \bar{S} = \bar{M} \end{cases} \quad (A.6)
\end{aligned}$$

or;

$$-2A_q^- \iint_{S_-} \bar{E}_{qt} \times \bar{H}_{qt} \cdot \hat{z} \, ds = \begin{cases} \iiint_V (\bar{E}_{qt} + \bar{E}_{qz}) \cdot \bar{J} e^{-j\beta_q z} \, dv & \text{for } \bar{S} = \bar{J} \\ -\iiint_V (\bar{H}_{qt} + \bar{H}_{qz}) \cdot \bar{M} e^{-j\beta_q z} \, dv & \text{for } \bar{S} = \bar{M} \end{cases} \quad (A.7)$$

Thus,

$$A_q^- = -\frac{1}{2 \iint_{S_-} \bar{E}_{qt} \times \bar{H}_{qt} \cdot \hat{z} \, ds} \begin{cases} \iiint_V (\bar{E}_{qt} + \bar{E}_{qz}) \cdot \bar{J} e^{-j\beta_q z} \, dv & \text{for } \bar{S} = \bar{J} \\ -\iiint_V (\bar{H}_{qt} + \bar{H}_{qz}) \cdot \bar{M} e^{-j\beta_q z} \, dv & \text{for } \bar{S} = \bar{M} \end{cases} \quad (A.8)$$

where  $A_q^-$  is the excitation coefficient of the mode  $\bar{E}_q^-$  traveling to the right of the source, i.e., in the region  $z < z_-$  shown in Figure A.1.

Case (ii):

If  $\bar{E}_q^-$ ,  $\bar{H}_q^-$  is chosen as the waveguide mode of interest as in Figure A.2, then the coefficient  $A_q^+$  of the mode  $\bar{E}_q^+$  traveling to the left of the source ( $z > z_+$ ) is given by:

$$A_q^+ = - \frac{1}{2 \iint_{S_-} \bar{E}_{qt} \times \bar{H}_{qt} \cdot \hat{z} \, ds} \left[ \begin{array}{l} \iint_V (\bar{E}_{qt} - \bar{E}_{qz}) \cdot \bar{J} e^{j\beta_q z} \, dv \\ - \iint_V (-\bar{H}_{qt} + \bar{H}_{qz}) \cdot \bar{M} e^{j\beta_q z} \, dv \end{array} \right]. \quad (A.9)$$

Note that  $\iint_{S_-} \bar{E}_{qt} \times \bar{H}_{qt} \cdot \hat{z} \, ds = \iint_{S_+} \bar{E}_{qt} \times \bar{H}_{qt} \cdot \hat{z} \, ds = \iint_{S_c} \bar{E}_{qt} \times \bar{H}_{qt} \cdot \hat{z} \, ds$  where  $S_c$  is any cross-sectional area of the waveguide.

Although Equations (A.8) and (A.9) are given for a volume source distribution, it is very simple to modify them for a surface (or line) source distribution. For this purpose, the volume integral on the right hand side of Equations (A.8) or (A.9) should be replaced by a surface (or line) integral over the extent of the surface (or line) source distribution.

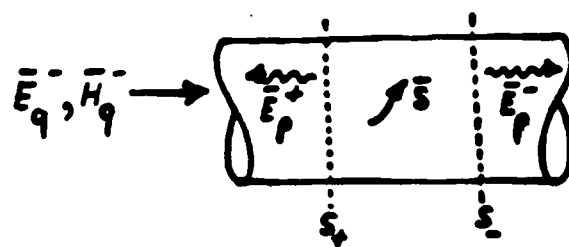


Figure A.2. Waveguide geometry with fields radiated to the left ( $z > z_+$ ) of  $\mathcal{S}$  being of interest.

**APPENDIX II**

**TABLES FOR THE CIRCULAR AND RECTANGULAR  
WAVEGUIDE MODE FUNCTIONS**

TABLE 1  
PROPERTIES OF MODES IN CIRCULAR WAVEGUIDE

TE <sub>nm</sub>	TM <sub>nm</sub>
$h_z = jN_{nm} \frac{P_{nm}^2}{a^2} J_n \left(\frac{P_{nm}^1}{a}\right) \left(\frac{\cos n\phi}{\sin n\phi}\right)$	0
$e_z = 0$	$jN_{nm} \frac{P_{nm}^2}{a^2} J_n \left(\frac{P_{nm}^1}{a}\right) \left(\frac{-\sin n\phi}{\cos n\phi}\right)$
$h_\rho = N_{nm} \frac{\beta_{nm} P_{nm}^1}{a} J_n' \left(\frac{P_{nm}^1}{a}\right) \left(\frac{\cos n\phi}{\sin n\phi}\right)$	$N_{nm} \frac{kY_0 n}{\rho} J_n \left(\frac{P_{nm}^1}{a}\right) \left(\frac{\cos n\phi}{\sin n\phi}\right)$
$h_\phi = N_{nm} \frac{n\beta_{nm}}{\rho} J_n \left(\frac{P_{nm}^1}{a}\right) \left(\frac{-\sin n\phi}{\cos n\phi}\right)$	$N_{nm} \frac{kY_0 P_{nm}}{a} J_n' \left(\frac{P_{nm}^1}{a}\right) \left(\frac{-\sin n\phi}{\cos n\phi}\right)$
$e_\rho = N_{nm} \frac{kZ_0 n}{\rho} J_n \left(\frac{P_{nm}^1}{a}\right) \left(\frac{-\sin n\phi}{\cos n\phi}\right)$	$N_{nm} \frac{\beta_{nm} P_{nm}}{a} J_n' \left(\frac{P_{nm}^1}{a}\right) \left(\frac{-\sin n\phi}{\cos n\phi}\right)$
$e_\phi = -N_{nm} \frac{kZ_0 P_{nm}^1}{a} J_n' \left(\frac{P_{nm}^1}{a}\right) \left(\frac{\cos n\phi}{\sin n\phi}\right)$	$-N_{nm} \frac{n\beta_{nm}}{\rho} J_n \left(\frac{P_{nm}^1}{a}\right) \left(\frac{\cos n\phi}{\sin n\phi}\right)$
$N_{nm} = \left[ \frac{1}{2} J_n \left(P_{nm}^1\right) \sqrt{\pi k Z_0 \beta_{nm} \epsilon_{on} (P_{nm}^2 - n^2)} \right]^{-1}$	$\left[ \frac{1}{2} J_n' \left(P_{nm}^1\right) P_{nm} \sqrt{\pi k Y_0 \beta_{nm} \epsilon_{on}} \right]^{-1}$
$\beta_{nm} = \sqrt{k^2 - \left(\frac{P_{nm}^1}{a}\right)^2}$	$\sqrt{k^2 - \left(\frac{P_{nm}^1}{a}\right)^2}$
$\epsilon_{on} = \begin{cases} 2 & n=0 \\ 1 & n \neq 0 \end{cases}$	

TABLE 2  
PROPERTIES OF MODES IN RECTANGULAR WAVEGUIDE

TE <sub>nm</sub>	TM <sub>nm</sub>
$h_z = N_{nm} Y_{nm} \frac{n_a^2 + m_b^2}{j\beta_{nm}} \cos n_a x \cos m_b y$	0
$e_z = 0$	$-N_{nm} \frac{n_a^2 + m_b^2}{j\beta_{nm}} \sin n_a x \sin m_b y$
$h_x = N_{nm} Y_{nm} n_a \sin n_a x \cos m_b y$	$-N_{nm} Y_{nm} m_b \sin n_a x \cos m_b y$
$h_y = N_{nm} Y_{nm} m_b \cos n_a x \sin m_b y$	$N_{nm} Y_{nm} n_a \cos n_a x \sin m_b y$
$e_x = N_{nm} m_b \cos n_a x \sin m_b y$	$N_{nm} n_a \cos n_a x \sin m_b y$
$e_y = -N_{nm} n_a \sin n_a x \cos m_b y$	$N_{nm} m_b \sin n_a x \cos m_b y$
$Y_{nm} = Y_0 \beta_{nm} / k$	$Y_0 k / \beta_{nm}$
$0 < x < a, \quad 0 < y < b$	

Note that for both modes:

$$N_{nm} = 4 [2\epsilon_{on} \epsilon_{om} Y_{nm} ab (n_a^2 + m_b^2)]^{-1/2}$$

$$\beta_{nm} = [k^2 - n_a^2 - m_b^2]^{1/2}$$

$$n_a = n\pi/a$$

$$\epsilon_{on} = \begin{cases} 2 & n=0 \\ 1 & n \neq 0 \end{cases}$$

$$m_b = m\pi/b$$

### APPENDIX III

#### EXPLICIT RADIATION COEFFICIENT FOR CIRCULAR AND RECTANGULAR INLETS

As mentioned in the text, the coupling coefficient  $\tilde{[S_{21}]}$  is related to the radiation coefficient  $[S_{12}]$  by reciprocity.

Therefore, if one is known, the other can be easily calculated from reciprocity relationship given in Section III.D.

For the near zone radiation case, there is no simple closed form analytic solution that can be obtained to calculate these coefficients; whereas, in the far zone radiation case, one can find simple closed analytic forms for the radiation coefficients and/or coupling coefficients.

In the following, the explicit form of the radiation coefficients in the far zone are given for both circular and rectangular waveguide modes.

##### A. For Circular Inlets:

In this case, the far zone field can be written as

$$\vec{E}^r = [\hat{\theta} E_\theta \left( \begin{smallmatrix} -\sin n\phi \\ \cos n\phi \end{smallmatrix} \right) + \hat{\phi} E_\phi \left( \begin{smallmatrix} \cos n\phi \\ \sin n\phi \end{smallmatrix} \right)] \frac{e^{-jkr}}{r}$$

where  $E_\theta$  and  $E_\phi$  can be separated as contributions from the Kirchhoff approximation and the equivalent Ufimtsev edge currents,

$$E_\theta = E_{\theta k} + E_{\theta u}$$

$$E_\phi = E_{\phi k} + E_{\phi u}$$

The contribution from the Kirchhoff approximation becomes:

**TE<sub>nm</sub> modes incidence:**

$$E_{\theta k} = j^n k Z_0 N_{nm} n \frac{1 + \cos\theta \cos\delta_{nm}}{2 \sin\theta} J_n(P_{nm}') J_n''(k \sin\theta)$$

$$E_{\phi k} = j^n k Z_0 N_{nm} P_{nm}' \frac{\sin\delta_{nm}}{2(\cos\delta_{nm} - \cos\theta)} J_n(P_{nm}') J_n''(k \sin\theta)$$

$$\delta_{nm} = \cos^{-1}(\beta_{nm}/k)$$

**TM<sub>nm</sub> modes incidence:**

$$E_{\theta k} = j^n k N_{nm} P_{nm} \frac{\sin\theta}{2(\cos\delta_{nm} - \cos\theta)} J_n'(P_{nm}) J_n''(k \sin\theta)$$

$$E_{\phi k} = 0$$

Likewise, the contribution from the equivalent Ufimtsev edge currents is given by:

**TE<sub>nm</sub> modes incidence:**

$$E_{\theta u} = j^n Z_0 N_{nm} n f(\theta, \delta_{nm}) J_n(P_{nm}') [\beta_{nm} \sin \frac{\theta}{2} J_n''(k \sin\theta)$$

$$- k P_{nm}' \sin \frac{\delta_{nm}}{2} \frac{\cos\theta}{k \sin\theta} J_n''(k \sin\theta)]$$

$$E_{\phi u} = j^n Z_0 N_{nm} f(\theta, \delta_{nm}) J_n'(P_{nm}) \left\{ k P_{nm} \sin \frac{\delta_{nm}}{2} J_n'(k \sin \theta) \right. \\ \left. - n^2 \beta_{nm} \sin \frac{\theta}{2} \frac{\cos \theta}{k \sin \theta} [J_n'(k \sin \theta) - \frac{J_n(k \sin \theta)}{k \sin \theta}] \right\}$$

**TM<sub>nm</sub> modes incidence:**

$$E_{\theta u} = j^n N_{nm} f(\theta, \delta_{nm}) J_n'(P_{nm}) \left[ n^2 \beta_{nm} \sin \frac{\delta_{nm}}{2} \frac{\cos \theta}{k \sin \theta} J_n(k \sin \theta) \right. \\ \left. + k P_{nm} \sin \frac{\theta}{2} J_n''(k \sin \theta) \right] .$$

$$E_{\phi u} = - j^n N_{nm} f(\theta, \delta_{nm}) J_n'(P_{nm}) \left\{ \beta_{nm} \sin \frac{\delta_{nm}}{2} J_n'(k \sin \theta) \right. \\ \left. + k P_{nm} \sin \frac{\theta}{2} \frac{\cos \theta}{k \sin \theta} [J_n'(k \sin \theta) - \frac{J_n(k \sin \theta)}{k \sin \theta}] \right\}$$

where

$$f(\theta, \delta_{nm}) = \frac{\cos \frac{\theta}{2} - \cos \frac{\delta_{nm}}{2}}{\cos \delta_{nm} - \cos \theta}$$

### B. For Rectangular Inlets:

In this case, the far zone field can also be expressed as:

$$E_\theta = E_{\theta k} + E_{\theta u}$$

$$E_\phi = E_{\phi k} + E_{\phi u}$$

The contribution from the Kirchhoff approximation becomes:

$$E_{\theta k} = \frac{j^{n+m} k N_{nm}}{4\pi} \frac{e^{-jkr}}{r} e^{j\frac{1}{2}k(a \cos\phi + b \sin\phi) \sin\theta}$$

$$\left\{ u \cos\phi \left(1 + \frac{Y_{nm}}{Y_0} \cos\theta\right) [A_+ + (-1)^n A_-] [B_+ - (-1)^m B_-] \right.$$

$$\left. - v \sin\phi \left(1 + \frac{Y_{nm}}{Y_0} \cos\theta\right) [A_+ - (-1)^n A_-] [B_+ + (-1)^m B_-] \right\}$$

$$E_{\phi k} = \frac{j^{n+m} k N_{nm}}{4\pi} \frac{e^{-jkr}}{r} e^{j\frac{1}{2}k(a \cos\phi + b \sin\phi) \sin\theta}$$

$$\left\{ -u \sin\phi \left(\cos\theta + \frac{Y_{nm}}{Y_0}\right) [A_+ + (-1)^n A_-] [B_+ - (-1)^m B_-] \right.$$

$$\left. - v \cos\phi \left(\cos\theta + \frac{Y_{nm}}{Y_0}\right) [A_+ - (-1)^n A_-] [B_+ + (-1)^m B_-] \right\}$$

$$\text{where } A_{\pm} = \frac{\sin [\frac{1}{2}(k \sin\theta \cos\phi \pm n_a) a]}{k \sin\theta \cos\phi \pm n_a}$$

$$B_{\pm} = \frac{\sin [\frac{1}{2}(k \sin\theta \sin\phi \pm m_b) b]}{k \sin\theta \sin\phi \pm m_b}$$

$$u = \begin{cases} m_b & \text{for TE mode} \\ n_a & \text{for TM mode} \end{cases}$$

$$v = \begin{cases} n_a & \text{for TE mode} \\ -m_b & \text{for TM mode} \end{cases}$$

Likewise the contribution from the equivalent Ufimtsev Edge Currents is given by:

$$E_{\theta u} = \sqrt{\frac{k}{8\pi j}} N_{nm} \frac{e^{-jkr}}{r} e^{j\frac{1}{2}k(a\cos\phi + b\sin\phi)} \sin\theta$$

$$\left\{ \frac{j^n}{\sqrt{\sin\beta_{oh}\sin\beta_h}} [e^{-j\frac{1}{2}kbs\sin\theta\sin\phi} - (-1)^m e^{j\frac{1}{2}kbs\sin\theta\sin\phi}] \right.$$

$$\cdot [D_s^u (\psi_h, \psi_h) u (A_+ + (-1)^n A_-) \cos\theta \cos\phi]$$

$$- \frac{\gamma_{nm}}{\gamma_0} D_h^u (\psi_h, \psi_h) v (A_+ - (-1)^n A_-) \sin\phi]$$

$$+ \frac{j^m}{\sqrt{\sin\beta_{ov}\sin\beta_v}} [e^{-j\frac{1}{2}kas\sin\theta\cos\phi} - (-1)^n e^{j\frac{1}{2}kas\sin\theta\cos\phi}]$$

$$\cdot [-D_s^u (\psi_v, \psi_v) v (B_+ + (-1)^m B_-) \cos\theta \sin\phi]$$

$$+ \frac{\gamma_{nm}}{\gamma_0} D_h^u (\psi_v, \psi_v) u (B_+ - (-1)^m B_-) \cos\phi] \right\}$$

$$E_{\phi u} = \sqrt{\frac{k}{8\pi j}} N_{nm} \frac{e^{-jkr}}{r} e^{j\frac{1}{2}k(a\cos\phi + b\sin\phi)} \sin\theta$$

$$\left\{ \frac{-j^n}{\sqrt{\sin\beta_{oh}\sin\beta_h}} [e^{-j\frac{1}{2}kbs\sin\theta\sin\phi} - (-1)^m e^{j\frac{1}{2}kbs\sin\theta\sin\phi}] \right.$$

$$\cdot [D_s^u (\psi_h, \psi_h') u (A_+ + (-1)^n A_-) \sin\phi$$

$$+ \frac{\gamma_{nm}}{\gamma_0} D_h^u (\psi_h, \psi_h') v (A_+ - (-1)^n A_-) \cos\theta\cos\phi]$$

$$- \frac{j^m}{\sqrt{\sin\beta_{ov}\sin\beta_v}} [e^{-j\frac{1}{2}kas\sin\theta\cos\phi} - (-1)^n e^{j\frac{1}{2}kas\sin\theta\cos\phi}]$$

$$\cdot [D_s^u (\psi_v, \psi_v') v (B_+ + (-1)^m B_-) \cos\phi$$

$$+ \frac{\gamma_{nm}}{\gamma_0} D_h^u (\psi_v, \psi_v') u (B_+ - (-1)^m B_-) \cos\theta\sin\phi] \right\}$$

where  $u$ ,  $v$ ,  $A_{\pm}$ ,  $B_{\pm}$  are defined as before, and

$$\cos\psi_h = \frac{\beta_{nm}/k}{\sin\beta_{oh}}$$

$$\cos\psi_h = - \frac{\cos\theta}{\sin\beta_h}$$

$$\sin\beta_{oh} = [1 - (n_a/k)^2]^{1/2}$$

$$\sin\beta_h = (1 - \sin^2\theta\cos^2\phi)^{1/2}$$

$$\cos\psi_v = \frac{\beta_{nm}/k}{\sin\beta_{ov}}$$

$$\cos\psi_v = - \frac{\cos\theta}{\sin\beta_v}$$

$$\sin\beta_{ov} = [1 - (m_b/k)^2]^{1/2}$$

$$\sin\beta_v = [1 - \sin^2\theta\sin^2\phi]^{1/2}$$

## APPENDIX IV

### EXPLICIT MODAL REFLECTION COEFFICIENTS AT THE OPEN END FOR THE CIRCULAR AND RECTANGULAR INLETS

As mentioned in the text, the modal reflection coefficients at the open end can be calculated from the equivalent magnetic currents  $M^l$  and  $M^{ld}$ , i.e.,

$$R_{pq;nm} = \frac{\int (\vec{h}_{pq} \cdot \vec{M}^l + \vec{h}_{zpq} \cdot \vec{M}) dl}{2 \int \vec{e}_{pq} \times \vec{h}_{pq} \cdot \hat{z} ds}$$

and

$$\frac{1}{2} \int \vec{e}_{pq} \times \vec{h}_{pq} \cdot \hat{z} ds = 1$$

So that

$$R_{pq;nm} = \frac{1}{4} \int (\vec{h}_{pq} \cdot \vec{M}^l + \vec{h}_{zpq} \cdot \vec{M}^{ld}) dl$$

The advantage of using this form is that  $R_{pq;nm}$  satisfies the reciprocity principle, i.e.,

$$R_{pq;nm} = R_{nm;pq}$$

An explicit expression for the reflection coefficient from an nm incident mode to pq reflected mode can be found from the explicit form of above equations, which is given by:

**A. For Circular Inlets:**

$$R_{pq;nm} = 0 \quad \text{if } p \neq n$$

$$R_{nq;nm}^h = \frac{\pi k Z_o}{j4a} \frac{N_{nq} N_{nm} J_n(P'_{nq}) J_n(P'_{nm})}{\cos \delta_{nq} + \cos \delta_{nm}} [n^2 \cos \delta_{nq} \cos \delta_{nm} \cdot f - k^2 a^2 \epsilon_{on} \sin \delta_{nq} \sin \delta_{nm} \cdot g]$$

$$R_{nq;nm}^e = \frac{\pi k Y_o}{j4a} \frac{N_{nq} N_{nm} J'_n(P'_{nq}) J'_n(P'_{nm})}{\cos \delta_{nq} + \cos \delta_{nm}} [k^2 a^2 \epsilon_{on} \sin \delta_{nq} \sin \delta_{nm} \cdot f - n^2 \cos \delta_{nq} \cos \delta_{nm} \cdot g]$$

$$R_{nq;nm}^h = R_{nm;nq}^e$$

$$= \frac{\pi k^2}{j4} \frac{N_{nq} N_{nm} n J_n(P'_{nq}) J'_n(P'_{nm})}{\cos \delta_{nq} + \cos \delta_{nm}} [\cos \delta_{nq} \sin \delta_{nm} \cdot f + \sin \delta_{nq} \cos \delta_{nm} \cdot g]$$

where

$$f = \cos \frac{\delta_{nq}}{2} \cos \frac{\delta_{nm}}{2} [1 + 2 (\sec \delta_{nq} + \sec \delta_{nm}) \frac{AD}{1-AD}]$$

$$g = \sin \frac{\delta_{nq}}{2} \sin \frac{\delta_{nm}}{2} [1 - 2 (\sec \delta_{nq} + \sec \delta_{nm}) \frac{AC}{1-AC}]$$

$$A = (-1)^n \frac{e^{-j(2ka - \pi/4)}}{4\sqrt{\pi ka}}$$

$$C = 1 + \sum_{\ell=1}^{\infty} (jB)^{\ell} / \sqrt{\ell+1}$$

$$D = 1 + \sum_{\ell=1}^{\infty} (-jB)^{\ell} / \sqrt{\ell+1}$$

$$B = (-1)^n \frac{1}{2} e^{-j2ka}$$

Due to the orthogonality of the trigonometric functions,  $\cos n\phi$  and  $\sin n\phi$ , which appear in the model functions, the above reflection coefficients apply only to modes with the same  $\phi$  variation and there is no coupling between modes with different  $\phi$  variations. It is noted that the effect of all the multiply interacting rays across the aperture are included in the above expressions for the circular inlet opening; in particular, that information is contained in the "f" and "g" terms given above. Unfortunately it is not a simple matter to include multiple interactions for the rectangular inlet opening which is dealt with next.

B. For Rectangular Inlets:

$$R_{pq;nm} = -\frac{1}{4} \sqrt{\frac{\pi}{2jk}} \frac{[1+(-1)^{n+p}][1+(-1)^{m+q}]}{4} \frac{N_{nm} N_{pq} Y_{nm} Y_{pq}}{Y_0}$$

$$\left\{ \begin{array}{l} \frac{a \delta_{np}}{\sqrt{\sin \beta_{oh} \sin \beta_h}} \left[ D_h(\psi_h, \psi_h') V_{nm} V_{pq} (1-\delta_{no}) \right. \\ \left. + D_s(\psi_h, \psi_h') \frac{Y_0 U_{nm}}{Y_{nm} \sin \psi_h} (\epsilon_{on} W_{pq} \frac{p_a^2 + q_b^2}{\beta_{pq}} \sin \beta_h - \frac{U_{pq} p_a}{k} \cos \psi_h) \right] \\ + \frac{b \delta_{mq}}{\sqrt{\sin \beta_{ov} \sin \beta_v}} \left[ D_h(\psi_v, \psi_v') U_{nm} U_{pq} (1-\delta_{mo}) \right. \\ \left. + D_s(\psi_v, \psi_v') \frac{Y_0 V_{nm}}{Y_{nm} \sin \psi_v} (\epsilon_{om} W_{pq} \frac{p_a^2 + q_b^2}{\beta_{pq}} \sin \beta_v - \frac{U_{pq} q_b}{k} \cos \psi_v) \right] \end{array} \right\}$$

where

$$D_s(\psi, \psi') = \frac{-e^{-j\pi/4}}{2\sqrt{2\pi k}} [\sec(\frac{\psi-\psi'}{2}) \mp \sec(\frac{\psi+\psi'}{2})] / \sqrt{\sin \beta_o \sin \beta_h}$$

$$\delta_{pq} = \begin{cases} 0 & p \neq q \\ 1 & p = q \end{cases}$$

$$\epsilon_{on} = \begin{cases} 2 & n=0 \\ 1 & n \neq 0 \end{cases}$$

$$\sin\beta_{oh} = [1 - (n_a/k)^2]^{1/2}$$

$$\sin\beta_h = [1 - (p_a/k)^2]^{1/2}$$

$$\sin\beta_{ov} = [1 - (m_b/k)^2]^{1/2}$$

$$\sin\beta_v = [1 - (q_b/k)^2]^{1/2}$$

$$\cos(\psi_h) = \frac{\beta_{nm}/k}{\sin\beta_{oh}}$$

$$\cos(\psi_h) = \frac{\beta_{pq}/k}{\sin\beta_h}$$

$$\cos(\psi_v) = \frac{\beta_{nm}/k}{\sin\beta_{ov}}$$

$$\cos(\psi_v) = \frac{\beta_{pq}/k}{\sin\beta_v}$$

$$v_{nm} = \begin{cases} n_a & \text{for } TE_{nm} \text{ mode} \\ -m_b & \text{for } TM_{nm} \text{ mode} \end{cases}$$

$$u_{nm} = \begin{cases} m_b & \text{for } TE_{nm} \text{ mode} \\ n_a & \text{for } TM_{nm} \text{ mode} \end{cases}$$

$$w_{nm} = \begin{cases} 1 & \text{for } TE_{nm} \text{ mode} \\ 0 & \text{for } TM_{nm} \text{ mode} \end{cases}$$

$N_{nm}$ ,  $Y_{nm}$ ,  $n_a$ , and  $m_b$  are defined as in Table 2, Appendix III.

**APPENDIX V**  
**DEFINITIONS OF THE GENERALIZED SCATTERING MATRICES**  
**FOR THE FAR-ZONE SCATTERING SITUATION**

When the observation point recedes to infinity, i.e., the far zone case, the scattering matrices are defined as follows [9]:

$[S_{11}]$  Matrix:

$$\begin{bmatrix} E_{\theta 0}^s \\ E_{\phi 0}^s \end{bmatrix} = [S_{11}] \begin{bmatrix} E_{\theta}^i \\ E_{\phi}^i \end{bmatrix} \frac{e^{-jkr}}{r}$$

$$[S_{11}] = \begin{bmatrix} S_{\theta\theta} & S_{\theta\phi} \\ S_{\phi\theta} & S_{\phi\phi} \end{bmatrix}$$

$[S_{12}]$  Matrix:

$$\begin{bmatrix} E_{\theta}^r \\ E_{\phi}^r \end{bmatrix} = [S_{12}] \begin{bmatrix} [A_{nm}^+] \\ [B_{nm}^+] \end{bmatrix} \frac{e^{-jkr}}{r}$$

$$[S_{12}] = \begin{bmatrix} [S'_{\theta nm}] & [S_{\theta nm}] \\ [S'_{\phi nm}] & [S_{\phi nm}] \end{bmatrix}$$

And the definitions of  $[S_{21}]$ ,  $[S_{22}]$  and  $[S_r]$  remain the same as before. Note that in this far zone case the range ( $r$ ) dependence is brought out of  $[S_{11}]$  and  $[S_{12}]$ , and the entry of the matrices has been changed from  $x, y, z$  components to  $\theta, \phi$  components.

## APPENDIX VI

### MODAL REFLECTION COEFFICIENTS FOR DISK-BLADE AND HUB STRUCTURE TERMINATIONS IN CIRCULAR INLETS

To find the reflection coefficients from the disk, disk-blade and hub structures in circular waveguides the method of P.O. approximation is employed. Although the P.O. approximation does not take into account the proper boundary conditions at the end of the structure, it certainly picks up the dominant effect and yields good approximation to the scattering results as compared with the measurements.

Due to the symmetry in the geometries of the terminal structures studied here, the coupling coefficients between modes with different  $\phi$  variations are small, so that they are neglected in the following discussion. Only the mutual coupling between those modes with the same  $\phi$  variation are included.

An explicit reflection coefficient for a disk-blade termination is given by

$$R_{nq;nm} = \frac{\pi}{2} (Z_{nq} + Z_{nm}) \epsilon_{on} \cdot \left[ \int_0^b (h_{\phi nq} h_{\phi nm} + h_{pnq} h_{pnm}) \rho d\rho + \frac{\alpha}{\alpha+\beta} \int_b^{b+d} (h_{\phi nq} h_{\phi nm} + h_{pnq} h_{pnm}) \rho d\rho \right],$$

where the integration from  $\rho=0$  to  $\rho=b$  is over the disk region and that from  $\rho=b$  to  $\rho=b+d$  is over the blade structure;  $\alpha$  is the angle extension

of the blade and  $\beta$  the angle extension of the air slot;  $Z_{nm} = \frac{k}{\beta_{nm}} Z_0$  for a  $TE_{nm}$  mode and  $\frac{B_{nm}}{k} Z_0$  for a  $TM_{nm}$  mode. The model functions are those given in Appendix II.

For a hemispherical hub termination with radius  $b$  the reflection coefficients are

$$R_{nq;nm}^{hh} = -\frac{\pi}{4} k Z_0 N_{nm} N_{nq} \epsilon_{on} \int_0^b d\rho e^{j(\beta_{nm} + \beta_{nq})\sqrt{b^2 - \rho^2}} \left\{ \begin{array}{l} \rho(\beta_{nm} + \beta_{nq}) \left[ J_n' \left( \frac{P_{nm}\rho}{a} \right) J_n' \left( \frac{P_{nq}\rho}{a} \right) \frac{P_{nm}P_{nq}}{a^2} + \frac{n^2}{\rho^2} J_n' \left( \frac{P_{nm}\rho}{a} \right) J_n' \left( \frac{P_{nq}\rho}{a} \right) \right] \\ + \frac{j\rho^2}{\sqrt{b^2 - \rho^2}} \frac{P_{nm}P_{nq}}{a^2} \left[ J_n' \left( \frac{P_{nm}\rho}{a} \right) \frac{P_{nm}}{a} \cdot J_n' \left( \frac{P_{nq}\rho}{a} \right) \right. \\ \left. + J_n' \left( \frac{P_{nq}\rho}{a} \right) \frac{P_{nq}}{a} \cdot J_n' \left( \frac{P_{nm}\rho}{a} \right) \right] \end{array} \right\},$$

$$R_{nq;nm}^{he} = -\frac{\pi}{4} k^2 N_{nm} N_{nq} \int_0^b d\rho e^{j(\beta_{nm} + \beta_{nq})\sqrt{b^2 - \rho^2}} n(1 + \beta_{nm} \beta_{nq}) \cdot \left[ \frac{P_{nq}}{a} J_n' \left( \frac{P_{nm}\rho}{a} \right) J_n' \left( \frac{P_{nq}\rho}{a} \right) + \frac{P_{nm}}{a} J_n' \left( \frac{P_{nm}\rho}{a} \right) J_n' \left( \frac{P_{nq}\rho}{a} \right) \right] + j \cdot \frac{\rho}{\sqrt{b^2 - \rho^2}} \cdot \left( \frac{P_{nm}^2}{a^2} \cdot \beta_{nq} + \left( \frac{P_{nq}}{a^2} \right)^2 \cdot \beta_{nm} \right) J_n' \left( \frac{P_{nm}\rho}{a} \right) J_n' \left( \frac{P_{nq}\rho}{a} \right),$$

$$\begin{aligned}
R_{nq;nm}^{ee} = & -\frac{\pi}{4} k Y_0 N_{nm} N_{nq} E_{cn} \cdot \int_0^b d\rho e^{j(\beta_{nm} + \beta_{nq})\sqrt{b^2 - \rho^2}} \\
& \left\{ \rho(\beta_{nm} + \beta_{nq}) \left[ J_n' \left( \frac{P_{nm}\rho}{a} \right) J_n' \left( \frac{P_{nq}\rho}{a} \right) \frac{P_{nm}P_{nq}}{a^2} \right. \right. \\
& \left. \left. + \frac{n^2}{\rho^2} J_n' \left( \frac{P_{nm}\rho}{a} \right) J_n' \left( \frac{P_{nq}\rho}{a} \right) \right] \right. \\
& \left. + j \frac{\rho}{\sqrt{b^2 - \rho^2}} \frac{P_{nm}P_{nq}}{a^2} \left[ - \frac{P_{nq}}{a} J_n' \left( \frac{P_{nm}\rho}{a} \right) J_n' \left( \frac{P_{nq}\rho}{a} \right) \right. \right. \\
& \left. \left. + \frac{P_{nm}}{a} J_n' \left( \frac{P_{nq}\rho}{a} \right) J_n' \left( \frac{P_{nm}\rho}{a} \right) \right] \right\}
\end{aligned}$$

Similarly, for a conical hub termination with base  $2b$  and height  $d$ , the reflection coefficients are

$$\begin{aligned}
R_{nq;nm}^{hh} = & -\frac{\pi}{4} k Z_0 N_{nm} N_{nq} \epsilon_{on} \int_0^b d\rho e^{j(\beta_{nm} + \beta_{nq}) \frac{d}{b} (b - \rho)} \\
& \cdot \left\{ \rho(\beta_{nm} + \beta_{nq}) \left[ J_n' \left( \frac{P_{nm}\rho}{a} \right) J_n' \left( \frac{P_{nq}\rho}{a} \right) \frac{P_{nm}P_{nq}}{a^2} \right. \right. \\
& \left. \left. + \frac{n^2}{\rho^2} J_n' \left( \frac{P_{nm}\rho}{a} \right) J_n' \left( \frac{P_{nq}\rho}{a} \right) \right] \right. \\
& \left. + \frac{j\rho d}{b} \frac{P_{nm}P_{nq}}{a^2} \left[ - J_n' \left( \frac{P_{nm}\rho}{a} \right) \frac{P_{nm}}{a} J_n' \left( \frac{P_{nq}\rho}{a} \right) \right. \right. \\
& \left. \left. + J_n' \left( \frac{P_{nq}\rho}{a} \right) \frac{P_{nq}}{a} J_n' \left( \frac{P_{nm}\rho}{a} \right) \right] \right\}.
\end{aligned}$$

$$R_{nq;nm}^{he} = -\frac{\pi}{4} k^2 N_{nm} N_{nq} \int_0^b d\rho e^{j((\beta_{nm} + \beta_{nq}) \frac{d}{b}(b-\rho))} \left\{ n(1+\beta_{nm}\beta_{nq}) \left[ -\frac{P_{nq}}{a} J_n'(\frac{P_{nm}\rho}{a}) J_n'(\frac{P_{nq}\rho}{a}) \right. \right. \\ \left. \left. + \frac{P_{nm}}{a} J_n'(\frac{P_{nm}\rho}{a}) J_n'(\frac{P_{nq}\rho}{a}) \right] \right. \\ \left. + j \frac{\rho d}{b} \cdot \left( \frac{P_{nm}^2}{a^2} \beta_{nq} + \frac{P_{nq}^2}{a^2} \cdot \beta_{nm} \right) J_n(\frac{P_{nm}\rho}{a}) J_n(\frac{P_{nq}\rho}{a}) \right\} ,$$

$$R_{nq;nm}^{ee} = -\frac{\pi}{4} k Y_0 N_{nm} N_{nq} \epsilon_{on} \cdot \int_0^b d\rho e^{j(\beta_{nm} + \beta_{nq}) \frac{d}{b}(b-\rho)} \left\{ \rho(\beta_{nm} + \beta_{nq}) \left[ -J_n'(\frac{P_{nm}\rho}{a}) J_n'(\frac{P_{nq}\rho}{a}) \frac{P_{nm}P_{nq}}{a^2} \right. \right. \\ \left. \left. + \frac{n^2}{\rho^2} J_n(\frac{P_{nm}\rho}{a}) J_n(\frac{P_{nq}\rho}{a}) \right] + j \frac{\rho d}{b} \frac{P_{nm}P_{nq}}{a^2} \right. \\ \left. \left[ -\frac{P_{nq}}{a} J_n'(\frac{P_{nm}\rho}{a}) J_n(\frac{P_{nq}\rho}{a}) + \frac{P_{nm}}{a} J_n'(\frac{P_{nq}\rho}{a}) J_n(\frac{P_{nm}\rho}{a}) \right] \right\} ,$$

## REFERENCES

- [1] J.B. Keller, "Geometrical Theory of Diffraction", *J. Opt. Soc. Am.*, Vol. 52, pp. 116-130, 1962.
- [2] R.G. Kouyoumjian, "The Geometrical Theory of Diffraction and its Applications", in Numerical and Asymptotic Techniques in Electromagnetics, R Mittra, ed., New York, Springer Verlag, 1975.
- [3] R.G. Kouyoumjian, P.H. Pathak, and W.D. Burnside, "A Uniform GTD for the Diffraction by Edges, Vertices, and Convex Surfaces", in Theoretical Methods for Determining the Interaction of Electromagnetic Waves with Structures, J.K. Skwirzynski, ed., Netherlands, Sijthoff and Noordhoff, 1981.
- [4] W.D. Burnside and L. Peters, Jr., "Axial RCS of Finite Cones by the Equivalent Current Concept with Higher Order Diffraction", *Radio Sci.*, Vol. 7, #10, pp. 943-948, October 1972.
- [5] E.F. Knott and T.B.A. Senior, "Comparison of Three High-Frequency Diffraction Techniques", *Proc. IEEE*, Vol. 62, pp. 1468-1474, 1974.
- [6] P.H. Pathak, "Techniques for High Frequency Problems", Chapter A7 in Handbook of Antenna Theory and Design, eds. Y.T. Lo and S.W. Lee, to be published by ITT-Howard W. Sams and Co., Inc.
- [7] P. Ya. Ufimstev, "Method of Edge Waves in the Physical Theory of Diffraction", (from the Russian "Method Krayevykh voin v fizicheskoy teorii difraktsii", Izd-Vo Vo. Radio, pp. 1-243, 1962), translation prepared by the U.S. Air Force Foreign Technology Division, Wright-Patterson Air Force Base, Ohio; released for public distribution, September 7, 1971.
- [8] S.N. Karp and J.B. Keller, "Multiple Diffraction by an Aperture in a Hard Screen", *Optica Acta*, Vol. 8, pp. 61-72, January 1961.
- [9] C.C. Huang, P.H. Pathak, C.Y. Lai and D.L. Moffatt, "Analysis of Electromagnetic Backscatter from an Inlet Cavity Configuration", Final Report 712661-4, October 1982, The Ohio State University ElectroScience Laboratory, Department of Electrical Engineering; prepared under Contract No. F19628-80-C-0056 for the Department of the Air Force, Electronic Systems Command, Hanscom Air Force Base.

- [10] P.H. Pathak, A. Altintas, C.W. Chuang and S. Barkeshli, "Near Field Scattering by Rectangular and Circular Inlet Configurations with an Impedance Surface Termination", Final Report 715267-1; prepared by The Ohio State University ElectroScience Laboratory for the Naval Weapons Center, China Lake, California on Grant No. N60530-83-M-40RD, July 1984.
- [11] R. Mittra and S.W. Lee, Analytical Techniques in the Theory of Guided Waves, The Macmillan Company, New York, 1971.
- [12] J. Van Bladel, Electromagnetic Fields, McGraw-Hill Electrical and Electronic Engineering Series, New York, 1964.
- [13] R.E. Collin, Foundations for Microwave Engineering, McGraw-Hill, New York, 1966.
- [14] J. Pace and R. Mittra, "Generalized Scattering Matrix Analysis of Waveguide Discontinuity Problems", Quasi-Optics, Vol. XIV, pp. 177-197, Polytechnic Institute of Brooklyn Press, New York, 1964.
- [15] S. Silver, Microwave Antenna Theory and Design, Boston Technical Publishers, Inc., 1964.
- [16] R. Mittra et. al., "Backscattering from Jet-Intakes (open-ended circular waveguides analyzed by the Wiener-Hopf procedure)", University of Illinois Technical Report.
- [17] L.A. Weinstein, The Theory of Diffraction and the Factorization Method, Golden Press, 1969.
- [18] A.D. Yaghjian, "Approximate Formulas for the Far Fields and Gain of Open-Ended Rectangular Waveguide", Report NBSIR83-1689, National Bureau of Standards, 1983.
- [19] P.H. Pathak and A. Altintas, "An Efficient Approach for Analyzing the EM Coupling into Large Open-Ended Waveguide Cavities", IEEE/APS Symposium and National Radio Science Meeting at the University of British Columbia, Vancouver, Canada, June 1985.
- [20] A. Altintas, "Electromagnetic Scattering from a Class of Open-Ended Waveguide Discontinuities," Ph.D. dissertation, The Ohio State University, Department of Electrical Engineering, Columbus, Ohio, Winter 1986.
- [21] W.D. Burnside, "Measured Data Report," Report 717675-1, generated under Contract N60530-85-C-0249, for Naval Weapons Center, China Lake, CA 93555, November 1985.